Synthesis and Characterization of Iron Oxides onto Cellulose Supports for Adsorption of Roxarsone

A Thesis Submitted to the College of
Graduate and Postdoctoral Studies
In Partial Fulfillment of the Requirements
For the Degree of Master of Science
In the Department of Chemistry
University of Saskatchewan
Saskatoon

By
Dexu Kong

PERMISSION TO USE

In presenting this thesis in partial fulfillment of the requirements for a Postgraduate degree from the University of Saskatchewan, I agree that the Libraries of this University may make it freely available for inspection. I further agree that permission for copying of this thesis in any manner, in whole or in part, for scholarly purposes may be granted by the professor or professors who supervised my thesis work or, in their absence, by the head of the Department or the Dean of the College in which my thesis work was done. It is understood that any copying, publication, or use of this thesis or parts thereof for financial gain shall not be allowed without my written permission. It is also understood that due recognition shall be given to me and to the University of Saskatchewan in any scholarly use which may be made of any material in my thesis. Requests for permission to copy or to make other use of material in this thesis in whole or part should be addressed to:

Head of the Department of Chemistry
University of Saskatchewan
Saskatoon, SK (S7N 5C9)
Canada

ABSTRACT:

This thesis reports on a systematic experimental study for the preparation of cellulose supported iron oxide (goethite and hematite) composite adsorbent materials, and the use of such materials for the adsorption of arsenic species from arsenic containing water. The research is divided into two sections: 1) Synthesis and characterization of the goethite and goethite-cellulose composites for the sorption of roxarsone (4-hydroxy-3-nitrobenzenearsonic acid) and 2) Synthesis and characterization of the hematite and hematite-cellulose composites for the sorption of roxarsone. Adsorption properties of the cellulose, goethite, hematite, goethite-cellulose, and hematite-cellulose adsorbents were studied with roxarsone as a model organoarsenical adsorbate.

Iron nanoparticles (NPs) and their cellulose composites were prepared with good yield, goethite and hematite were 98% and 97%, respectively. The characterization of various adsorbent materials used several techniques: Thermal gravimetric analysis (TGA), Fourier transform infrared (FTIR) spectroscopy, Raman spectroscopy, nitrogen gas adsorption/desorption (BET), ^{13}C solid state NMR (ssNMR) spectroscopy, Transmission electron microscopy (TEM) and powder X-ray diffraction (pXRD). To understand the mode of interaction between the adsorbent and the adsorbate, Roxarsone (ROX) was used to study the molecular aspects of the adsorption process. The comparison between goethite-cellulose composites and hematite-cellulose composites was made by examining the surface area and available active adsorption sites on the iron oxide and cellulose materials surfaces. The nitrogen adsorption/desorption experiments showed hematite NPs have a relatively high surface area while TEM showed better dispersion of 10 nm hematite NPs onto the surface of cellulose at low iron coating. The maximum monolayer uptake (Q_m) of the hematite was 0.155 mmol/g which was two-fold greater than goethite. The Q_m value for the 25% Fe coated hematite-cellulose was 0.10 mmol/g and was 1.5-fold greater than the Q_m value for the 30% Fe coated goethite-cellulose composite. The kinetic uptake results for the 25% Fe coated hematite-cellulose was 0.186 min^{-1}, and exceeded the uptake rate for the 35% Fe coated goethite-cellulose. The better dispersion of hematite NPs resulted in more available active sites on the cellulose surface which increased the overall uptake of the roxarsone.

Both goethite and hematite NPs provide adsorption sites that can bind with arsenic containing species. It is a cost effective and efficient way to disperse iron NPs onto a cellulose surface because such supported NPs are involved in the adsorption of arsenic species. On the other hand, the composite materials have an advantage over the pure mineral phase since composites can reduce NP leaching whilst enhancing the uptake of arsenic species at a lower levels of iron oxide doping.

ACKNOWLEDGEMENTS

I thank Professor Dr. Lee D. Wilson for his generous advice, inspiring guidance, and encouragement throughout my research. I also would like to thank him for reading the thesis manuscript and providing me with significant and constructive suggestions.

I want to thank the funding provided by Saskatchewan Research Council (SRC) and University of Saskatchewan Department of Chemistry. I also would like to thank Thomas Bonli from the Department of Geological Sciences for helping me with the pXRD analysis, Jianfeng Zhu from (Saskatchewan Structure Science Centre) SSSC for helping me with the ssNMR measurements, and the environmental analytical lab at SRC for assisting me with water chemistry analyses.

To the committee members, who acted as advisors and spared time from their busy schedules to guide my research, I offer my thanks: Dr. David Palmer (Chair 2016), Dr. Marek Majewski (Committee Advisor), Dr. Matthew Paige, Dr. Robert Scott, and Dr. Dale Ward.

I would like to thank my group members Dr. Abdalla Karoyo, Leila Dehabadi, Chen Xue, Asghar Dolatkhah, Inimfon Udoetok, Savi Bhalkaran and Mohammad Hassan Mahaninia. I wish them the best of luck in their research projects, and I also thank Wendy Wang for assisting in my research projects, too.

I also thank my family for supporting me through my graduate study work.

TABLE OF CONTENTS

PERMISSION TO USE ..... **I**

ABSTRACT: ..... **II**

ACKNOWLEDGEMENTS ..... **IV**

LIST OF TABLES ..... **X**

LIST OF FIGURES ..... **XII**

LIST OF SCHEMES ..... **XV**

LIST OF ABBREVIATIONS ..... **XVI**

CHAPTER 1 : INTRODUCTION **1**

1.1 ROXARSONE (ROX) 1

1.1.1 Sources of arsenic pollution 1

1.1.2 Physical and chemical properties of the roxarsone and inorganic arsenic species 2

1.1.3 Toxicity of arsenic species in the environment 4

1.1.4 Remediation of roxarsone 5

1.2 IRON CHEMISTRY 7

1.2.1 Introduction 7

1.2.2 Iron oxide 7

1.2.2.1 Iron oxide crystal structure 10

1.2.2.2 Iron and its oxides' electronic properties 12

1.2.2.2.1 Electronic properties – free iron 12

1.2.2.2.2 Iron oxide electronic properties – crystal field theory 13

1.2.2.2.3 Electronic properties – molecular orbital theory 15

1.3 CELLULOSE 16

1.3.1 Iron oxide-cellulose composite materials as adsorbents for water treatment 17

1.4 PHYSICAL ADSORPTION 18

1.4.1 Introduction 18

1.4.2 Solution vs. Gas based adsorption 19

1.4.3 Types of isotherms 20

1.4.3.1 Hysteresis in solid-gas adsorption/desorption curves 23

1.4.4 Models of sorption isotherms 24
1.4.4.1 Langmuir isotherm model 24
1.4.4.2 Freundlich isotherm model 25
1.4.4.3 The BET (Brunauer-Emmett-Teller) adsorption isotherm 26
1.4.5 Models of sorption kinetics 27
1.4.5.1 PFO (Pseudo-first-order) kinetics 27
1.4.5.2 PSO (Pseudo-second-order) kinetics 28
1.5 Application of Physical Adsorption: Goethite, Ferrihydrite, and Hematite 28
1.6 Application of Physical Adsorption: Cellulose and Cellulose Based Materials 31
1.7 Purpose of the Research 31
1.8 Objectives 32
CHAPTER 2 : MATERIALS AND METHODS 33
2.1 Introduction 33
2.2 Materials 33
2.3 Synthesis 33
2.3.1 Preparation of the goethite and goethite-cellulose composite materials 33
2.3.2 Preparation of the hematite and hematite-cellulose composite materials 35
2.3.3 Preparation of ferrihydrite NPs materials 36
2.4 Instrumental Analysis 36
2.4.1 TGA 36
2.4.2 FT-IR spectroscopy 36
2.4.3 Raman spectroscopy 36
2.4.4 TEM 37
2.4.5 pXRD 37
2.4.6 N_2 adsorption–desorption analysis (BET) 37
2.4.7 Solid state ^{13}C NMR spectroscopy 38
2.4.8 Iron coating efficiency 38
2.5 Sorption Measurements 39
2.5.1 Roxarsone adsorption isotherms 39

2.5.1.1 Roxarsone adsorption isotherms of the goethite and goethite-cellulose composites 39
2.5.1.2 Roxarsone adsorption isotherms of the hematite and hematite-cellulose composites..... 39
2.5.2 Roxarsone adsorption kinetics 40
2.5.2.1 Roxarsone adsorption kinetics of the goethite & goethite-cellulose composites . 40
2.5.2.2 Roxarsone adsorption kinetics of the hematite & hematite-cellulose composites 41
2.5.3 Adsorption thermodynamic study..... 42
2.5.4 Regeneration study..... 42
2.5.5 The hydration effect in the ROX adsorption process..... 43
2.6 Error Analysis of Sorption Measurement 43
2.7 Iron Leaching Tests..... 44
CHAPTER 3 : RESULTS AND DISCUSSION: SYNTHESIS AND CHARACTERIZATION OF GOETHITE, HEMATITE, GOETHITE-CELLULOSE, AND HEMATITE-CELLULOSE 45
3.1 TGA Results 45
3.1.1 TGA for the goethite and goethite-cellulose composites..... 45
3.1.2 TGA for the hematite and hematite-cellulose composites..... 47
3.2 FTIR Spectroscopy..... 49
3.2.1 FTIR for the goethite and goethite-cellulose composites 49
3.2.2 FTIR for the hematite and hematite-cellulose composites 51
3.3 Raman Spectroscopy 52
3.3.1 Raman spectroscopy of the cellulose, goethite, and goethite-cellulose composites.... 52
3.3.2 Mode of adsorption between the ROX, goethite and goethite-cellulose composites .. 54
3.3.3 Mode of adsorption between the ROX, hematite and hematite-cellulose composites 56
3.3.4 Hydration properties of adsorbent materials..... 59
3.4 TEM 60
3.4.1 TEM of the goethite and the 10% Fe coated goethite-cellulose composite..... 60
3.4.2 TEM of the hematite and different Fe coated hematite-cellulose composites..... 62
3.4.3 TEM of the ferrihydrite NPs..... 64
3.5 pXRD..... 66

3.5.1 pXRD for the cellulose, the goethite and different Fe coated goethite-cellulose composites 66
3.5.2 pXRD for the ferrihydrite, the hematite and different Fe coated hematite-cellulose composites 68
3.6 BET 70
3.6.1 Goethite and different Fe coated goethite-cellulose composites 70
3.6.2 Ferrihydrite 72
3.6.3 Hematite and different Fe coated hematite-cellulose composites 73
3.7 SOLID STATE ^{13}C NMR SPECTROSCOPY 76
3.7.1 Goethite and different Fe coated goethite-cellulose composites 76
3.7.2 Hematite and different Fe coated hematite-cellulose composites 76
3.8 IRON COATING EFFICIENCY 77
3.8.1 Goethite and different Fe coated goethite-cellulose composites 77
3.8.2 Hematite and different Fe coated hematite-cellulose composites 78
CHAPTER 4 : RESULTS AND DISCUSSION: CELLULOSE, GOETHITE, AND GOETHITE-CELLULOSE MATERIALS' SORPTION OF ROXARSONE 79
4.1 ROXARSONE ADSORPTION ISOTHERMS 79
4.1.1 pH effects on the sorption of ROX 79
4.1.2 Different Fe coated composites effect on the sorption of ROX 82
4.1.2.1 Various Fe content goethite-cellulose composites 82
4.1.2.2 Various Fe coated hematite-cellulose composites 82
4.1.3 Adsorption isotherm models for the goethite and goethite-cellulose composites 83
4.1.4 Adsorption isotherm models for the hematite and HeCell composites 86
4.2 ROXARSONE ADSORPTION KINETICS BY THE "FILTER BARRIER" METHOD 87
4.2.1 Adsorption kinetics models for the goethite and goethite-cellulose composites 87
4.2.2 Adsorption kinetics models for the hematite and hematite-cellulose composites 90
4.3 THERMODYNAMIC STUDY 92
4.3.1 Adsorption parameters of the 30% Fe coated GC composite 92
4.3.2 Adsorption parameters of the 25% Fe coated HeCell composite 92
4.3.3 The uptake of ROX by the 10% Fe coated HeCell at various Temperature 93
4.4 REGENERATION OF THE 10% FE COATED HECELL ADSORBENT 96

4.4.1 10% Fe coated HeCell regeneration with the 0.6 M NaOH solution..... 96
4.5 IRON LEACHING TEST 97
4.6 ADSORPTION MECHANISM 99
CHAPTER 5 : CONCLUSION AND FUTURE WORK 100
5.1 CONCLUSION 100
5.2 FUTURE WORK 101
REFERENCES 103

LIST OF TABLES

Table 1.1 Acid–base equilibrium constants for arsenic acid (H_3AsO_4) and arsenous acid (H_3AsO_3) in aqueous solution. 3
Table 1.2 General properties of the goethite, ferrihydrite, and hematite [26] 10
Table 1.3 Crystallographic data for iron oxides 11
Table 1.4 Technological application of different forms of cellulose 17
Table 1.5 Adsorption application of goethite, ferrihydrite and hematite materials towards anion species 29
Table 1.6 The cation adsorption studies of iron oxides. 30
Table 3.1 Total specific surface area of the goethite NPs and the 10% Fe coated GC 72
Table 3.2 Total specific surface area of ferrihydrite from BET analysis 73
Table 3.3 The BET specific surface area for the hematite and different Fe coated HeCell composites 75
Table 3.4 Fe coating efficiency of GC composite adsorbent materials with variable Fe content 78
Table 3.5 Fe coating efficiency of HeCell composite adsorbent materials with variable Fe content 78
Table 4.1 Roxarsone adsorption values by GC composite adsorbent materials with variable Fe content 82
Table 4.2 Roxarsone adsorption values by HeCell materials with variable Fe content 83
Table 4.3 Isotherm adsorption parameters for the roxarsone onto the cellulose, the goethite, and GC composite materials at 295 K 84
Table 4.4 Isotherm adsorption parameters for the roxarsone onto the hematite and the HeCell composite materials at 295 K. 87
Table 4.5 Adsorption kinetics experiment parameters from the PFO and PSO models for uptake of roxarsone onto the cellulose, the goethite and the 30% Fe coated GC adsorbents at 295 K. 89
Table 4.6 Adsorption kinetic parameters from the PFO and PSO models for the uptake of roxarsone onto hematite and HeCell adsorbents at 295 K 91
Table 4.7 Thermodynamic parameters at 295 K for the adsorption of the roxarsone onto the goethite and the 30% Fe coated GC adsorbent materials 92
Table 4.8 Thermodynamic parameters at 295 K for the adsorption of the roxarsone onto the hematite and HeCell adsorbent materials 93

Table 4.9 Adsorption kinetics experiment parameters from the PSO model for the uptake of ROX onto adsorbents at different temperature 94
Table 4.10 Thermodynamic parameters for the uptake of ROX by the 10% Fe coated HeCell .. 95
Table 4.11 ROX adsorption efficiency of the 10% Fe loaded HeCell after each washing cycle . 97
Table 4.12 The iron leaching tests 98

LIST OF FIGURES

Figure 1.1 Molecular structure of roxarsone 3
Figure 1.2 Sources of iron oxides in the global environment 8
Figure 1.3 The multidisciplinary nature of iron oxide research 8
Figure 1.4 Crystallographic arrangement of hcp 11
Figure 1.5 *d*-orbital splitting in common iron complexes 13
Figure 1.6 Ligand field spectrochemical series 14
Figure 1.7 *d*-orbital filling patterns for a d^4 electron configuration 14
Figure 1.8 MO diagram for the octahedral complex of $[Fe(H_2O)_6]^{3+}$ 15
Figure 1.9 Molecular structure of cellulose formed from β-1, 4 linked D-glucose units, with hydrogen bonding between parallel chains 16
Figure 1.10 Comparison of absorption and adsorption processes 19
Figure 1.11 Gas phase and solution phase adsorption 20
Figure 1.12 Various types of sorption isotherms for gas adsorption [24] 21
Figure 1.13 General types of hysteresis loops observed for nitrogen adsorption and desorption as defined by IUPAC [52] 23
Figure 1.14 Langmuir model of physical adsorption of a gas onto a solid adsorbent. 25
Figure 1.15 Freundlich isotherm model of physical adsorption of gas where surface heterogeneity sites are part of the adsorbent surface. 25
Figure 2.1 An illustration of the "filter barrier" setup for kinetic uptake studies 41
Figure 2.2 Block diagram of adsorption-desorption-stripping cycle 43
Figure 2.3 Setup for iron leaching tests 44
Figure 3.1 TGA results: (a) goethite, (b) 30% Fe coated GC, and (c) cellulose 46
Figure 3.2 TGA results: (a) hematite, (b) cellulose, and (c) 10% Fe coated hematite-cellulose .. 49
Figure 3.3 FTIR spectral results: (a) goethite, cellulose and GC materials, and (b) FTIR spectra of the GC materials with different Fe content 12.1%, 20.3% and 30.9%. 50
Figure 3.4 FTIR spectra of cellulose, hematite and HeCell materials with different Fe content 5%, 10% and 25% 51
Figure 3.5 Raman spectra of cellulose, synthetic goethite, and the 10% Fe coated GC 53
Figure 3.6 Raman spectra of the adsorbent materials before and after the roxarsone uptake, (a) Goethite, and (b) Cellulose and GC composites 54

Figure 3.7 Raman spectra of hematite and composites with different Fe loading levels 57
Figure 3.8 Raman spectra of the hematite and 10% Fe coated HeCell before and after uptake of roxarsone 58
Figure 3.9 Raman spectra of ROX adsorption by hematite in 5% (Vol.) D_2O/H_2O solvent 60
Figure 3.10 TEM of (a) and (b) goethite, (c), (d), (e), (f) goethite-cellulose under 500, 200, 100, 50 nm scale, (g), (h), (i), and (j) cellulose were obtained at 500, 200, 100, 50 nm scales. 62
Figure 3.11 TEM of (a) and (b) hematite, (c) and (f) hematite-cellulose in 200 nm scale, (d), (e), (g), and (h) hematite-cellulose materials at 100 nm scale 64
Figure 3.12 TEM of ferrihydrite NPs, (a) and (b) were synthesized in this study, (c) and (d) were from Schwertmann's work [119] 65
Figure 3.13 pXRD results for cellulose, goethite and goethite-cellulose composite materials 67
Figure 3.14 pXRD of ferrihydrite, hematite and different Fe coated HeCell composites 69
Figure 3.15 pXRD of cellulose, 10% Fe coated HeCell and 10% Fe coated GC 69
Figure 3.16 Goethite sorption/desorption profile with nitrogen at 77 K 71
Figure 3.17 10% Fe coated GC composite sorption/desorption profile at 77 K 71
Figure 3.18 Ferrihydrite sorption/desorption profile with nitrogen at 77 K 73
Figure 3.19 Hematite nitrogen sorption/desorption profile at 77 K 74
Figure 3.20 10% Fe coated HeCell nitrogen sorption/desorption profile at 77 K 75
Figure 3.21 ^{13}C CP-MAS solids NMR (ssNMR) spectra of Goethite and different Fe coated GC composites 76
Figure 3.22 ^{13}C CP-MAS solids NMR spectra of the hematite and HeCell composites 77
Figure 4.1 (a) Schematic of dominant charge states for ROX (roxarsone) and goethite at variable pH conditions. (b) The pH effect of the roxarsone equilibrium uptake by a 10% Fe coated GC composite with a roxarsone solution (0.040 mM) using an adsorbent dosage at 0.2 g/L. 80
Figure 4.2 Adsorption isotherms and "best fit" results for roxarsone with various adsorbent materials (Goethite, GC, and Cellulose) at 295 K (a) Langmuir isotherm and (b) Freundlich isotherm model 85
Figure 4.3 Adsorption isotherm of roxarsone with various adsorbent materials at 295 K. (a) Langmuir model fit of the hematite and HeCell composites, and (b) Freundlich model fitting of the hematite and HeCell composites. 86

Figure 4.4 Kinetic uptake experiments for the cellulose, the goethite, and the 30% Fe loaded GC, as described by two kinetic models: (a) PFO, and (b) PSO models. 88
Figure 4.5 Kinetic uptake isotherms for the hematite and hematite-cellulose composite materials, as described by two kinetic models: (a) PFO, and (b) PSO models. 90
Figure 4.6 PSO fitted ROX uptake by the 10% Fe coated HeCell composite material..... 93
Figure 4.7 Eyring plots for ROX uptake at variable temperature at pH 7 95
Figure 4.8 The activation energy (E_a) of the adsorption process of roxarsone onto the 10% Fe coated HeCell composites..... 95
Figure 4.9 Regeneration graph of the 10% Fe loaded HeCell composite material..... 96
Figure 4.10 Electrostatic interactions between goethite NPs and roxarsone at pH 4 and pH 7.... 99

LIST OF SCHEMES

Scheme 1.1 Speciation of roxarsone at variable pH in water 4
Scheme 2.1 Synthetic scheme for the formation of goethite-cellulose composite materials..... 34
Scheme 2.2 A proposed pathway for the formation of hematite-cellulose composite materials.. 35

LIST OF ABBREVIATIONS

ASTM (American Society for Testing and Materials)

BET (Brunauer-Emmett-Teller)

ccp (cubic close-packed)

Eqn. (Equation)

FWHM (Full width at half maximum)

Fh (Ferrihydrite)

Fig. (Figure)

FT-IR (Fourier Transform Infrared)

GAC (Granular Activated Carbon)

Goe (Goethite)

GC (Goethite-cellulose)

hcp (hexagonal close-packed)

HeCell (Hematite-cellulose)

H-bonding (Hydrogen bonding)

HFO (Hydrous Ferric Oxide)

IR (Infrared Spectroscopy)

IUPAC (International Union of Pure and Applied Chemistry)

Log K_{ow} (log octanol/water partition coefficient)

mM (Millimolar)

MO (Molecular orbital)

MMER (Metal Mining Effluent Regulations)

NMR (Nuclear Magnetic Resonance)

ppm (parts per million, mg/L)

PNP (p-nitrophenol)

pXRD (powder X-ray Diffraction)

pK_a (Acid dissociation constant)

PZC (Point-of-zero-charge)

PFO (Pseudo-first-order)

PSO (Pseudo-second –order)

ROX (Roxarsone)

RPM (Revolutions per minute)

SEM (Scanning Electron Microscopy)

SSA (Specific surface area)

SSSC (Saskatchewan Structure Science Centre)

ssNMR (Solid State NMR)

TGA (Thermogravimetry Analysis)

TEM (Transmission electron microscopy)

UV-vis (Ultraviolet-visible)

CHAPTER 1 : INTRODUCTION

Arsenic species possess variable toxicity, especially in cases where long-term exposure to arsenic from drinking water and food can cause cancer [1]. Various wastewater treatment technologies have been tested for arsenic removal: (i) oxidation/precipitation processes offer simple and rapid removal at low cost but have limited removal efficiency; (ii) coagulation and flocculation are relatively facile and efficient processes but often result in sludge by-products with arsenic; (iii) membrane-based techniques are relatively high cost such as nano filtration and reverse osmosis (RO)with good removal efficiency but are prone to membrane fouling. RO produces large quantities of wastewater [2], where ca. 3 to 4 volumes of wastewater are produced relative to permeate water for desalination processes [3]. By contrast, adsorption technology is a very cost effective method and is relatively simple to implement. This Master of Science thesis describes research on the preparation cellulose supported iron oxide (goethite and hematite) composite adsorbent materials and the use of such materials for the adsorption of arsenic species from arsenic (V) species in water. Roxarsone was used as a model organic arsenic compound to evaluate the adsorption efficiency of the binary composite materials. Two objectives for this research are as follows: 1) to develop improved iron oxide-cellulose composite materials with enhanced adsorption properties toward arsenic species; 2) to develop a greater understanding of the "structure-function relationship", in terms of the adsorption properties for such systems.

1.1 Roxarsone (ROX)

1.1.1 Sources of arsenic pollution

Prior to 2012, many livestock producers used roxarsone (ROX; 4-hydroxy-3-nitrobenzenearsonic acid) as a feed additive for poultry production to control coccidia intestinal parasites. The safety of organoarsenicals such as ROX was raised after minor levels of chemical change were reported after consumption by poultry, the inorganic arsenic species were found

accumulated in soils [4]. However, roxarsone residues in poultry litter and waste may undergo chemical decomposition, especially when applied as a fertilizer and conditioner to soil matter. [5] The decomposition by-products of ROX include various organic and inorganic forms of arsenic. The inadvertent dispersal via crop and animal production may pose risks to ecosystems and human health, according to Brown et al. [6], where such organo-arsenicals may undergo microbial degradation. ROX undergoes rapid biotransformation to As (V) in the soil horizon with weak adsorption to soil that undergoes further degradation to inorganic arsenic species arsenite (H_3AsO_3) and arsenate (H_3AsO_4). Since arsenite and arsenate have relatively high mobility in aquatic systems and soil, an understanding of the environmental fate and transport of ROX in soil and aquatic environments is incomplete at present. Finally, arsenic species can occur either naturally or by anthropogenic sources in the environment. Roxarsone is one example of an arsenic pollutant from anthropogenic point source. Natural causes of arsenic breakdown in surface water are due to soil erosion, mineral leaching, volcanic deposits, and weathering [7]. Human activities such as smelting operations, fossil-fuel combustion, and gold or uranium mining are also major point sources of arsenic pollution [8].

1.1.2 Physical and chemical properties of the roxarsone and inorganic arsenic species

Elemental arsenic with atomic number 33 is a metalloid in group 5A of the periodic table. Elemental arsenic has 5 electrons in its valence electron shell and has 8 different oxidation states (5, 4, 3, 2, 1, -1, -2, -3) [9]. The redox potential and pH conditions affect the distribution of arsenic species in natural water, where the dominant inorganic forms of arsenic are the oxyanion forms of arsenite (As^{3+}) and arsenate (As^{5+}), according to Table 1.1 [9]. Arsenic contamination of surface water normally occurs at pH values between 6 to 8 that concur with the pK_a around 8 which correspond to the mono- and di-anion species of arsenate and non-ionized arsenite. This results in a reduced removal of arsenite species when compared against the removal of arsenate species at pH above 8.Table 1.1 shows the chemical forms of arsenic species at different pKa.

Table 1.1 Acid–base equilibrium constants for arsenic acid (H_3AsO_4) and arsenous acid (H_3AsO_3) in aqueous solution.

Arsenic Species	Chemical Equilibria	Chemical Equilibria	Chemical Equilibria
As (V)	$H_3AsO_4 \rightleftharpoons H_2AsO_4^- + H^+$ $pK_a = 2.22$	$H_2AsO_4^- \rightleftharpoons HAsO_4^{2-} + H^+$ $pK_a = 6.98$	$HAsO_4^{2-} \rightleftharpoons AsO_4^{3-} + H^+$ $pK_a = 11.53$
As (III)	$H_3AsO_3 \rightleftharpoons H_2AsO_3^- + H^+$ $pK_a = 9.22$	$H_2AsO_3^- \rightleftharpoons HAsO_3^{2-} + H^+$ $pK_a = 12.1$	$HAsO_3^{2-} \rightleftharpoons AsO_3^{3-} + H^+$ $pK_a = 12.7$

Various chemical methods that involve oxidation of arsenite As (III) to arsenate As (V) and then removal of the charged arsenic species can occur by adsorption because most arsenate species bare negative charge at pH 8. Hence, oxidizing arsenite As (III) to arsenate As (V) is one facile approach for the remediation of arsenic contaminated water.

Figure 1.1 illustrates the molecular structure of Roxarsone (4-hydroxy-3-nitrobenzenearsonic acid). The effects of variable charge states of ROX due to ionization equilibria are shown in Scheme 1.1 where roxarsone carries no charge when pH<3 and negative charges when pH increases above the respective pK_a values.

Roxarsone

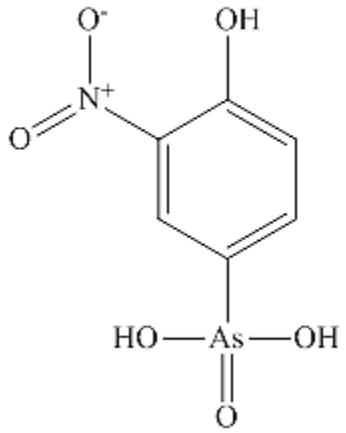

Figure 1.1 Molecular structure of roxarsone

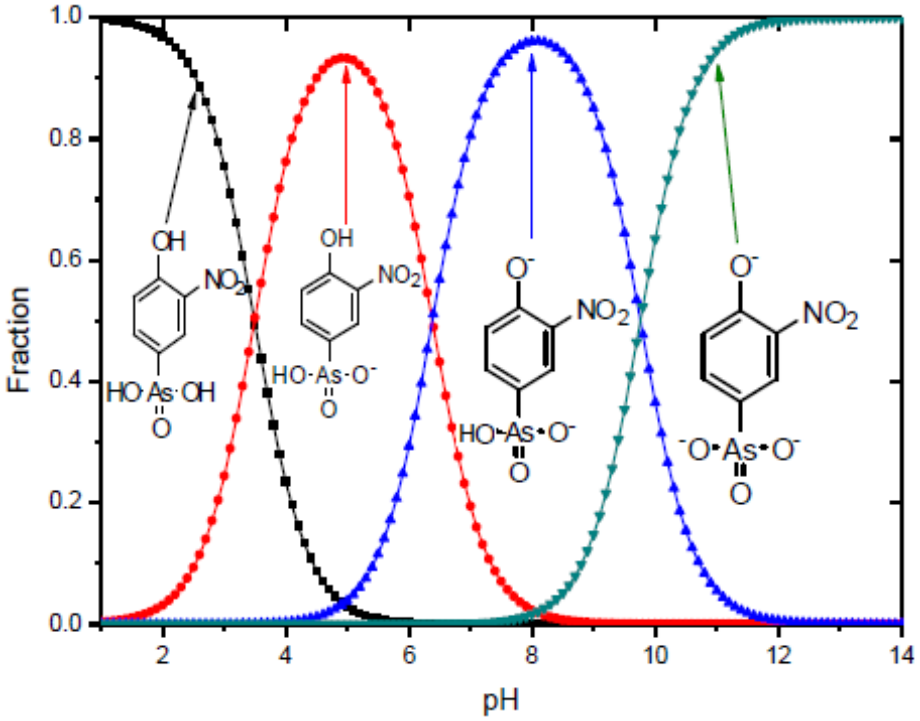

Scheme 1.1 Speciation of roxarsone at variable pH in water

1.1.3 Toxicity of arsenic species in the environment

Arsenic contamination of soils and aquatic environments is a concern due to its toxicity as evidenced by the Toroku arsenic disease [8]. High levels of arsenic are found in nature and anthropogenic sources in many countries, including Bangladesh, New Zealand, USA, Italy, and Malaysia [10]. The World Health Organization (WHO) established international health standards for arsenic in drinking water at a maximum value of 10 ppb to minimize the risks of arsenic exposure. In Canada, the metal mining effluent regulations (MMER) require that Canadian mining industries adhere to the release limits on arsenic, radium-226, and total suspended solids [11]. Uranium mill tailings from the Key Lake mill mining site in northern Saskatchewan contains elevated levels of arsenic and nickel species [12]. In 2006, a national news release reported the arsenic levels from the untreated water on the Saskatchewan Gordon First Nation reserve in Canada were nearly four times above the acceptable limit [13].

1.1.4 Remediation of roxarsone

To address potential health concerns regarding arsenic waterborne contaminants, various wastewater treatment technologies have been tested: (i) oxidation/precipitation processes offer simple and rapid removal with low cost, but have limited arsenic removal efficiency; (ii) coagulation and flocculation are relatively facile and efficient processes, but often result in arsenic containing sludge by-products; (iii) membrane-based techniques are relatively high cost that include the nanofiltration and reverse osmosis (RO) while offering good removal with limited efficiency due to membrane fouling. The RO method produces large quantities of wastewater [2] and in the case of desalination, ca. 3 to 4 volumes of water are produced as wastewater relative to permeate water [3]. By contrast, adsorption techniques are well established with good uptake that is primarily determined by the various types of adsorbent media (e.g., activated alumina, ion exchange resins, and iron coated sand). Iron oxide NPs have received much attention in adsorption technology due to the relatively large surface area and active sites that can bind with arsenic species. While adsorbent technology is relatively facile with much scope for future development, it is often limited by the nature of the adsorbent material. Inorganic adsorbents for arsenic removal include metal organic frameworks [14], iron and aluminum oxides [15], while iron oxide composites have been reported to display relatively high uptake [16]. An ionic solvent (urea-thiourea-NaOH) at low temperature was developed to dissolve cellulose fibers for synthesis of iron oxide-cellulose composites [17]. The low temperature synthetic method may pose limitations due to the harsh basicity of the solvent and its effect on the molecular structure of cellulose. Iron oxide-cellulose composites using other methods are known where variable uptake of As species (arsenite; 32.1 mg/g and arsenate; 183 mg/g) were recently reported [18]. Iron (hydr)oxide-modified multi-wall carbon nanotubes (MWCNTs) showed a maximum adsorption capacity (Q_m = 5.98 mg/g) for roxarsone [19]. Similar results were obtained by using MWCNTs to yield a maximum adsorption capacity (Q_m = 9.36 mg/g) for roxarsone [20]. Iron oxide-based composites containing granular activated carbon (GAC) were reported to display dual adsorption properties due to the removal of organoarsenicals and inorganic species [21]. The use of iron oxide nanoparticles (NPs) such as goethite was tested for the removal of roxarsone due to the comparable uptake observed for organic and inorganic species, the reported roxarsone uptake by goethite was 0.673 mmol/g at pH 7 [22]. However, such metal oxide NPs are potentially mobile in the environment and pose certain

challenges for practical water treatment. The use of supported NPs was reported to dramatically reduce the occurrence of leaching [19] whilst retaining favourable adsorption properties. Cellulose is a versatile biopolymer support with unique molecular structure due to its numerous polar hydroxyl groups which may coordinate with iron oxide-based NPs to form stable composites. Such types of binary composite materials may display tunable surface charge according to the respective pH_{pzc} value (the pH value that results in a net zero net electrical charge on the surface) of the components and their relative composition. The value of pH_{pzc} for cellulose is ca. 4 which indicates its point of zero charge is near pH 4 [23] and the value for goethite is ca. 9 [24].

Herein, this thesis reports on the preparation, characterization, and adsorption properties of cellulose composite materials containing goethite/hematite nanoparticles (NPs). A systematic adsorption study of the properties of goethite-cellulose and hematite-cellulose composite materials with roxarsone at variable conditions (pH, equilibrium, and dynamic conditions) was carried out to provide thermodynamic and kinetic adsorption parameters for the uptake process. Roxarsone is a suitable model compound that can be used to further understand the fate and transport of organoarsenicals in aquatic environments. This thesis reports several contributions to the field of cellulose biopolymers and adsorption-based phenomena: (i) the development of a composite cellulose material with immobilized goethite and hematite NPs for the adsorption of roxarsone, (ii) the development of an improved understanding of uptake properties of roxarsone using goethite-cellulose and hematite-cellulose composites, and (iii) a first report of a systematic study on goethite-cellulose and hematite-cellulose composite materials with roxarsone. A comparison of the adsorption properties of goethite-cellulose and hematite-cellulose materials relative to cellulose and goethite or hematite NPs provide an understanding of the role of surface modification of cellulose along with the relationship of structure and adsorption properties for these types of composites.

1.2 Iron Chemistry

1.2.1 Introduction

Iron is a group 8, *d*-block element with silver-white color; it exists in a wide range of oxidation states, -2 to +6. Iron is the fourth most abundant element in the earth's crust. Elemental iron can undergo rapid oxidization to iron oxides at ambient conditions in the environment. The most common usage of iron includes the fabrication of carbon steel and iron alloys. Carbon steels are made from 99.5% of elemental iron and 0.1-0.5% carbon by weight; and stainless steels are made from iron alloys with ~ 18% and ~ 8% nickel for corrosion resistance [25].

1.2.2 Iron oxide

Iron oxides occur widely in the environment and are readily synthesized in the laboratory. The aerobic weathering of rocks on the earth's surface is the main source of the Fe^{3+} oxides. Wind/water erosion process will redistribute iron oxides into soil and lakes, rivers, and oceans. Human activities such as mining and industrial application of iron oxides also increase the release of iron oxides in the global system. Figure 1.2 shows an outline of the occurrence of iron oxides in the global environment system [26].

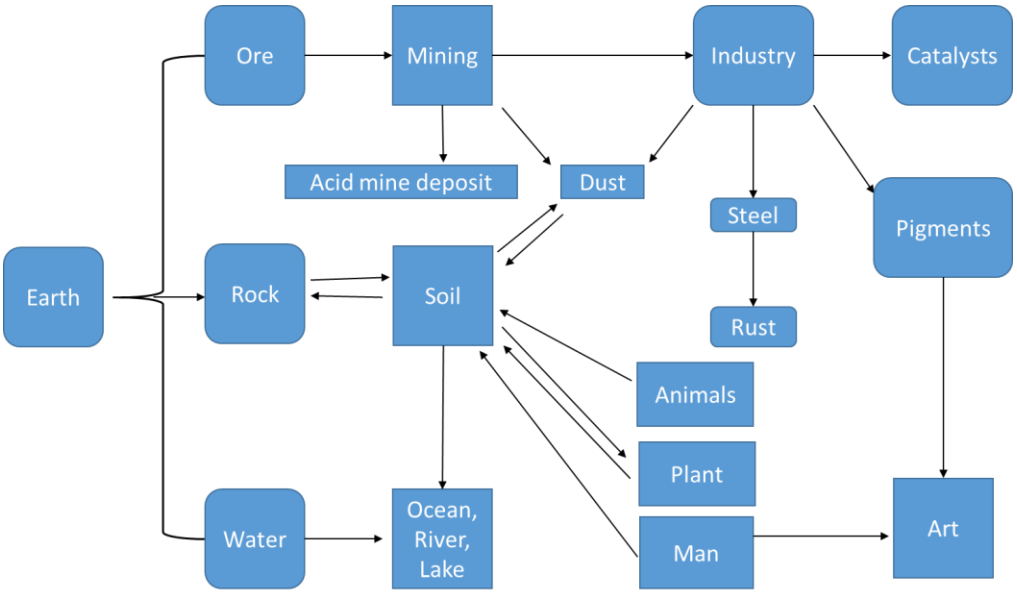

Figure 1.2 Sources of iron oxides in the global environment

The research about iron oxides are truly multidisciplinary, where Figure 1.3 shows the application of iron oxides in all different research areas [26].

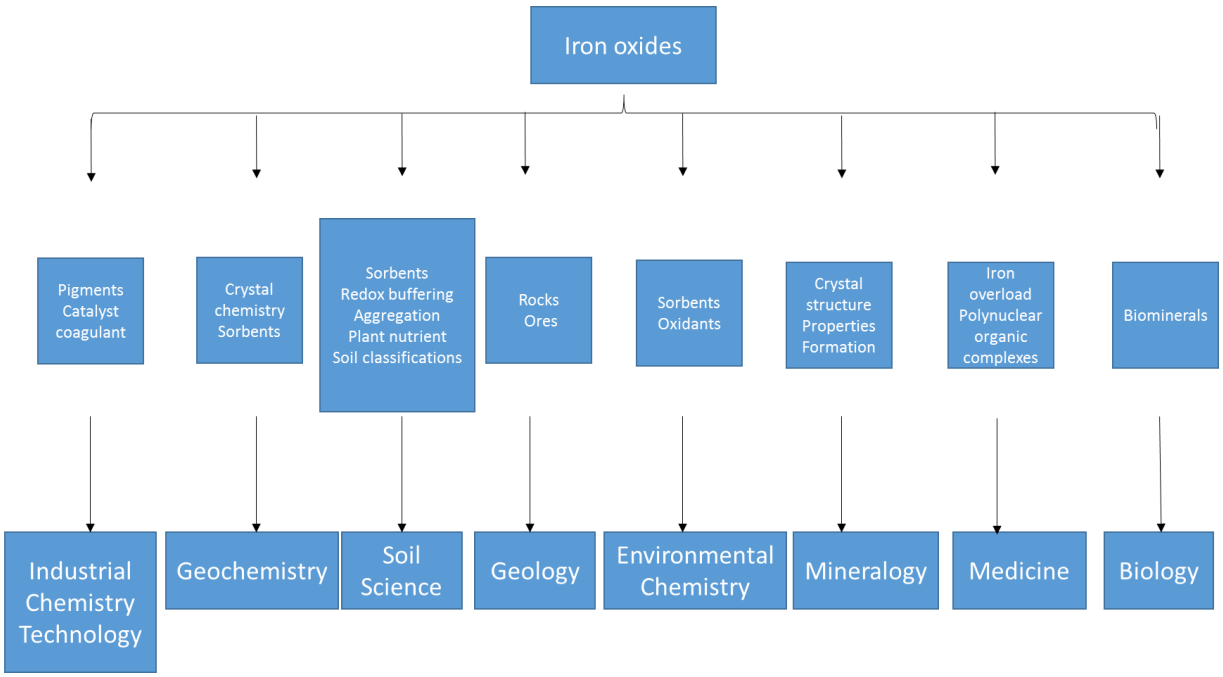

Figure 1.3 The multidisciplinary nature of iron oxide research

There are many types of iron oxides, but the scope of this research will focus on three major types: goethite, ferrihydrite, and hematite. Most iron oxides are crystalline besides ferrihydrite which is poorly crystalline and certain iron oxides are isomorphous. For example, goethite (α-FeOOH) is isomorphous and it is found in rocks and throughout various compartments of the global ecosystem. It has a diaspore structure which is based on hexagonal close packing of anions (hcp). It is one of the most thermodynamically stable forms of iron oxides since it consists of an hcp array of anions O^{2-} and OH^- stacked along the [010] direction, where Fe^{3+} ions occupy half of the octahedral interstices within a layer. Each Fe ion is surrounded by three O^{2-} and three OH^- to give $FeO_3(OH)_3$ octahedra, and the structure is usually described in terms of these octahedra [26].

Ferrihydrite is poorly ordered and the degree of ordering is variable. The two extremes of such crystal ordering are referred to as 2-line and 6-line ferrihydrites. An exact formula for ferrihydrite has not yet been determined because a precise separation of structural OH and H_2O from adsorbed water results in structural complexity. Towe and Bradley suggested the bulk formula $Fe_5HO_8 \cdot 4H_2O$ which is certainly to be preferred over $Fe(OH)_3$, because of the bound water molecules. Infrared measurements using D_2O exchange have suggested that ferrihydrite contains OH^- and O^{2-} with about half of the protons present such as OH^- and the remainder as water (150 g/kg) [27]. The unit cell parameters given by Chukhrov et. al. [Fe 1.42 O1.26 (OH)1.74] appear closer to the real composition of 6-line ferrihydrite [28]. In 1992 Stanjek & Weidler suggested the composing factors $0.15 < OH/Fe < 0.86$ by performing a water loss test by heating the ferrihydrite and assuming that no transformation to hematite occurred [29].

Hematite is similar to goethite and is extremely stable that is often the end stage of transformations to other iron oxides [26]. It has a molecular formula (α-Fe_2O_3) and its unit cell is hexagonal with a = 0.5034 nm and c =1.375 nm [30]. There are six formula units per cell. For hexagonal symmetry, the Miller indices are (hkil); i may be replaced by a dot or omitted. The structure of hematite can be described as consisting of hcp arrays of oxygen ions stacked along the [001] direction, where the planes of anions are parallel to the (001) plane. Two thirds of the sites are filled with Fe^{3+} ions which are arranged regularly with two filled sites being followed by one vacant site in the (001) plane thereby forming six-fold rings. The arrangement of cations produces pairs of $Fe(O)_6$ octahedra. Each octahedron shares edges with three neighboring octahedra in the same plane and one face with an octahedron in an adjacent plane. Face-sharing occurs along the

c-axis. The face-sharing of octahedra is responsible for the distortion of the cation sub-lattice from ideal packing; Fe atoms in the octahedra which share faces are repelled along the direction normal to the [001], causing the cations to shift closer to the unshared faces. To provide charge balance, O^{2-} may be partly replaced by the OH^{-} accompanied by Fe^{3+} vacancies. General properties of the iron oxides such as the goethite, ferrihydrite and hematite are described in Table 1.2. Generally speaking the iron oxide NPs with more amorphous crystallinity have larger surface area, the larger surface area would favor their adsorption capacity. Briefly looking at the crystallinity of goethite, hematite and ferrihydrite, a very general statement about these iron oxide NPs adsorption capacity could be predicted as follows: ferrihydrite > hematite > goethite.

Table 1.2 General properties of the goethite, ferrihydrite, and hematite [26]

	Goethite	Ferrihydrite	Hematite
Density (g/cm^3)	4.26	3.96	5.26
Octahedral occupancy	½	<2/3	2/3
Color	Yellow-brown	Red-brown	Red
Hardness	5 – 5.5	N/A	6.5
Standard free energy of formation ΔG^0_f (kJ/mol)	-488.6	-699	-742.7

1.2.2.1 Iron oxide crystal structure

The crystal structures of iron oxides such as hematite and goethite are determined by single crystal X-ray diffraction. Table 1.3 Crystallographic data for iron oxides [26]. The crystal structures of iron oxides are generally represented by close packed geometries of anion layers or as linkages of octahedron and tetrahedron units.

Table 1.3 Crystallographic data for iron oxides

Compound	Crystallographic system	Stacking of close packed anions	Unit cell dimensions (nm)			Z (anions number per unit cell)
			x	y	z	
Goethite	Orthorhombic	ABAB [001]	0.9956	0.3021	0.4608	4
Ferrihydrite	Hexagonal	ABAB [001]	0.2955	N/A	0.937	4
Hematite	Hexagonal (rhombohedral)	ABAB [001]	0.50356	N/A	1.37489	6

In the close packing of the anion layer, each Fe cation and oxygen anion are considered as spheres. The large sized anions usually make up the framework of the crystal lattice and the smaller sized cations normally fill the holes and spaces among the frameworks of anions. Geometrically, the cubic close-packed (ccp), hexagonal close-packed (hcp) are examples of structures that can minimize similar charge interactions from the ion within the lattice. The Fe cation and anions from goethite, hematite and Fe $(OH)_2$ crystal structure represent A and B on two different planes, and these planes will stack in ABAB order along the Miller index [001] plane to form the hexagonal closed-packed structure in Figure 1.4.

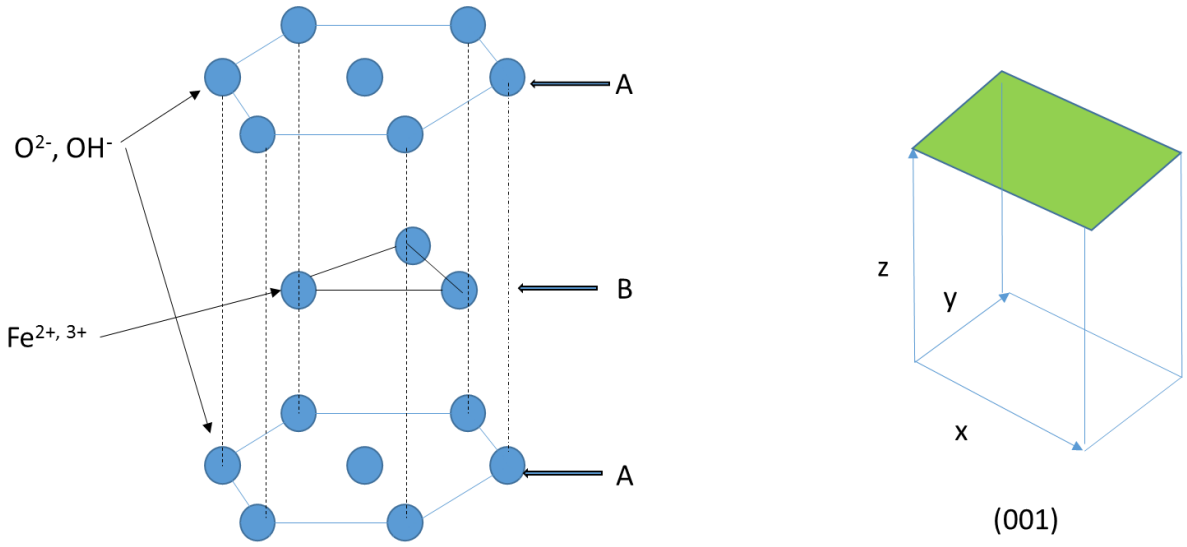

Figure 1.4 Crystallographic arrangement of hcp

Another way to explain how the hcp structure is formed for the hematite and ferrihydrite is to link the octahedron shape units of Fe $(O)_6$ or $FeO_3(OH)_3$ and tetrahedron units of $Fe(O)_4$ by corners, edges or faces. The crystal structure of iron oxide plays an important role in adsorption of arsenic species, where the arrangement of ions (oxygen, iron and OH^-) can alternate the porosity of iron oxide NPs from microporous to mesoporous. The pore size of iron oxide NPs result in different surface area which will affect their adsorption capacity. On the other hand, the arrangement of OH^- function groups of goethite NPs can also impact the adsorption capacity. For instance, more OH^- presented on the outside shell of goethite NPs will favor arsenic species uptake.

1.2.2.2 Iron and its oxides' electronic properties

1.2.2.2.1 Electronic properties – free iron

To understand the physical and chemical behavior of iron, it is pertinent to give some fundamental information about relevant properties of electrons and nuclei. Iron is a group 8, *d*-block element with atomic number 26 and electron configuration $1s^2$, $2s^2$, $2p^6$, $3s^2$, $3p^6$, $3d^6$, $4s^2$. Electrons are described by four kinds of quantum numbers from the wave function, n (principal quantum number), l (angular momentum), m_l (magnetic quantum number) and m_s (spin projection quantum number) that represent the radial distance from the nucleus (shell), shape (subshell), energy shift (orientation of the subshell shape), and spin of the electron, respectively. The principal quantum number, n, takes on integer values (1, 2, 3, etc.) with energy increasing by increasing n. The shape quantum number, l, adopts values of 0, 1, 2, 3, etc. (or by letters *s*, *p*, *d*, *f*, etc.), and adopts $2l+1$ orientations. The magnetic quantum number has values that range from +l to –l. Spin projection quantum number, m_s, where an electron has only two values -1/2 for "spin down" and +1/2 for "spin up". For example, *d* electrons will have a quantum number of 2 which will give $2 \times 2+1 = 5$ orientations of the subshell's shape (*d*-orbitals d_{xy}, d_{xz}, d_{yz}, d_{x2-y2}, and d_{z2}). The magnetic and a number of spectroscopic properties of Fe-containing species are governed by the electrons in the 3*d* orbitals of Fe. The following sections will give a brief introduction to the principles that are responsible for the behavior of these electrons.

1.2.2.2.2 Iron oxide electronic properties – crystal field theory

The basis of crystal field theory is when Fe is forming ionic compounds, its electrons will have a repulsive interaction with other electrons of the surrounding atoms (ligand) [31]. As a ligand approaches the Fe species, the electrons from the ligand repel the electrons in the *d*-orbitals of iron. Those *d*-electrons closer to the ligands will have a higher energy than those farther away, the result of the repulsion between the *d*-orbitals and electrons from ligands causes splitting in energy. Common iron oxide complexes are octahedral where six ligands form an octahedron around the Fe ion, and tetrahedral complexes where four ligands form a tetrahedron around the metal ion. Figure 1.5 shows energy levels of the *d*-orbitals in commonly occurring iron complexes.

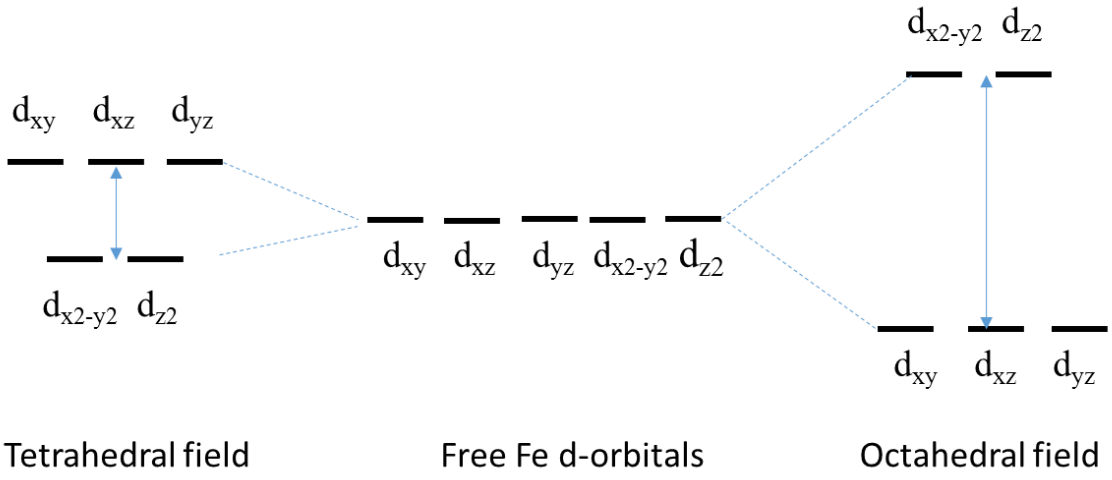

Figure 1.5 *d*-orbital splitting in common iron complexes

The above *d*-orbital splitting is caused by ligands and "low spin" and "high spin" of ligand field theory are based on the experimental results of adsorption spectra of a cobalt complex reported in 1938 [32]. Some ligands like Br^- and I^- will result in low spin and CN^- could result in high spin. Figure 1.6 indicates the spectrochemical series of ligands.

$I^- < Br^- < Cl^- < F^- < OH^- < C_2O_4^{2-} < H_2O < NH_3 <$ en < bipy < phen < CN^- ~ CO

Spectrochemical Series

Figure 1.6 Ligand field spectrochemical series

The ways of *d*-electron filling into the octahedral *d*-orbitals in the high-spin (HS) state and the low-spin (LS) state are shown in Figure 1.7.

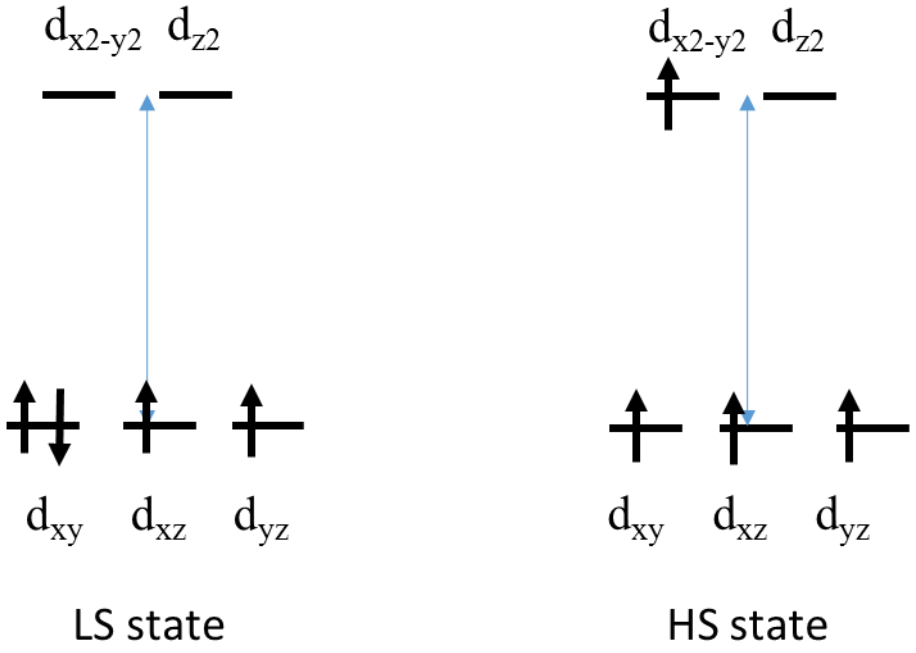

Figure 1.7 *d*-orbital filling patterns for a d^4 electron configuration

Figure 1.9 above illustrates how Fe *d*-orbitals will split and electrons will fill in these *d*-orbitals when interacting with different ligands. The following paragraph will introduce molecular orbital theory to describe electron interaction between atoms under the influence of the nuclei in the whole molecule.

1.2.2.2.3 Electronic properties – molecular orbital theory

The molecular orbital (MO) theory describes the distribution of electrons in molecules and incorporates the wave character of electrons in developing MO diagrams. With basic information on electronic properties of free iron and crystal field theory described above, MO diagrams of complexes can be constructed to predict the physical and chemical properties of a molecule such as shape, bond energy, bond length and bond angle.

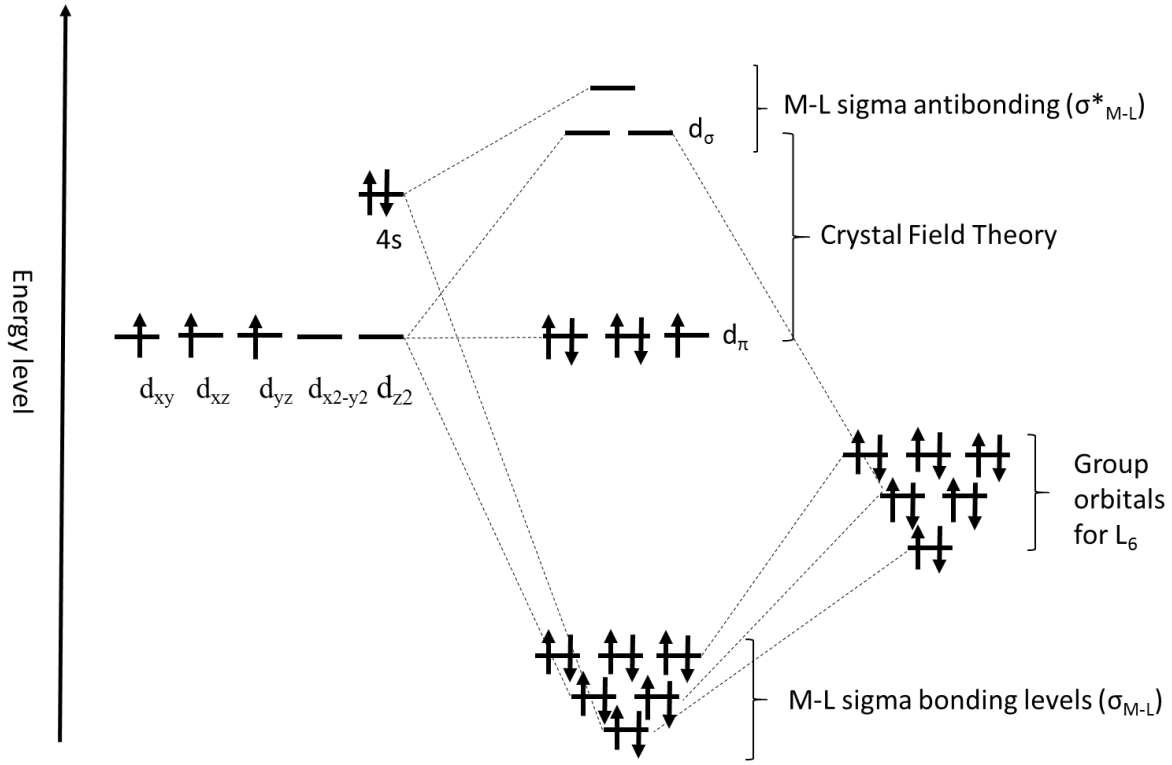

Figure 1.8 MO diagram for the octahedral complex of $[Fe(H_2O)_6]^{3+}$

Iron oxides such as goethite, hematite, and ferrihydrite prepared from Fe^{3+} ions normally form the octahedral complex (Figure 1.8) with water molecules.

1.3 Cellulose

Cellulose is the most abundant natural biopolymer. Each cellulose molecule is an unbranched polymer containing from 1,000 to 1 million D-glucose units. It is formed by β-1, 4 linkages between D-glucose monomer units [33]. Figure 1.9 shows the structure of cellulose formed from β-1, 4 linked D-glucose units, with hydrogen bonding between parallel chains. The various kinds of inter- and intra-molecular hydrogen bonds that are formed by hydroxyl groups at the C2-, C3-, and C6-positions of cellulose. Cellulose is permeable, meaning that it allows water and other substances to pass through it freely. Unlike starch and glycogen, cellulose cannot be hydrolyzed easily, because of the formation of inter- and intra- molecular hydrogen bonds in the cellulose fibril structure [34].

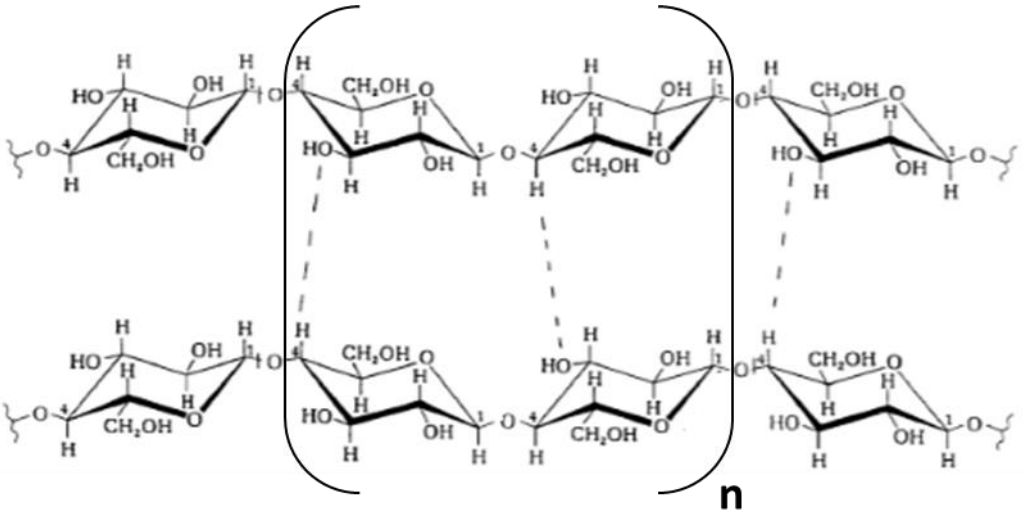

Figure 1.9 Molecular structure of cellulose formed from β-1, 4 linked D-glucose units, with hydrogen bonding between parallel chains

Cellulose is a colorless, odorless, and a nontoxic solid polymer. Because of its great mechanical strength, biocompatibility, relative thermostability, and high sorption capacity, cellulose materials has been investigated and researched for various applications. Table 1.4 lists some selected examples of cellulose-based materials and their technological applications.

Table 1.4 Technological application of different forms of cellulose

Material forms	Applications	References
Film/membrane	Separation, water treatment, adsorption, biomembrane, package, *etc*.	[35], [36], [37]
Nanocomposite	Adhesion, drug delivery, membrane, *etc*.	[38], [39], [40]
Polymer	Biomaterial, water treatment, thickener, stabilizer, *etc*.	[41], [42]
Fiber	Reinforcement material, *etc*.	[43]

1.3.1 Iron oxide-cellulose composite materials as adsorbents for water treatment

Cellulose is an environmentally friendly biomaterial with many applications. Due to the presence of available hydroxyl groups, cellulose is considered to be an excellent material for surface modification [44]. At the same time, a combination between bioadsorbents and iron oxide NPs can pose an efficient biocomposite material which could possibly show high adsorption capacity and easy recovery from treated effluents by magnetic separation. Meanwhile, pure iron oxide NPs tend to undergo aggregation because of interparticle electrostatic forces that reduce the intrinsic magnetic properties, resulting in a weak magnetic response and a decreased surface area [45]. To avoid aggregation, natural polymers such as cellulose have attracted much attention due to their environmentally friendly character. The use of composite materials comprised of functionalized cellulose as a support for iron oxide NPs can overcome the aggregation issues of iron oxide NPs. In turn, this will contribute to improved adsorption capacity of toxic contaminants [46]. Here, cellulose is used as supporting material for goethite NPs to make goethite-cellulose composite materials. Iron oxide NPs can be used as adsorbent materials for charged particles such as arsenate and arsenite species. Among the various types of iron oxides, goethite has abundant hydroxide groups which can be used as binding sites for metal ions. Similar types of cellulose and iron oxide composite materials were developed by Yu and her coworkers [17]. The latter study outlined the feasibility of developing iron oxide-cellulose composite materials for arsenic removal.

Duro and others investigated and compared arsenic adsorption onto natural goethite, hematite and magnetite NPs [47]. Herein, goethite showed potential adsorption ability towards arsenic which indicate that the hydroxide groups available for binding arsenic are important in the sorption properties. In this study, the goethite NPs were synthesized by precipitation of $FeCl_3$ in NaOH and then impregnated onto cellulose fiber powders to produce goethite-cellulose (GC) composites.

1.4 Physical Adsorption

1.4.1 Introduction

Adsorption and absorption are two processes that contribute to the overall sorption process. Absorption is the partitioning of adsorbates into the interior of the adsorbent where the sorbate may change the physical properties of the adsorbent; where the adsorption is the attraction of the adsorbates from the bulk phase onto the external surface of an adsorbent, and this process is normally reversible.

Adsorption in solution experimental results that adsorption is a spontaneous process. The spontaneous process indicates an overall lowering of the Gibbs energy of a system (Gibbs energy, ΔG). In other words, generally speaking the adsorption process is spontaneous because it gives off energy in the form of heat ($\Delta H < 0$) and indicates an exothermic process. According to the second law of thermodynamics, a spontaneous process indicates ($S > 0$) a more disordered system after adsorption process. However the change in entropy of adsorption (ΔS) for the system can be negative or positive (decrease or increase) with the level of adsorption depending on the role of solvent.

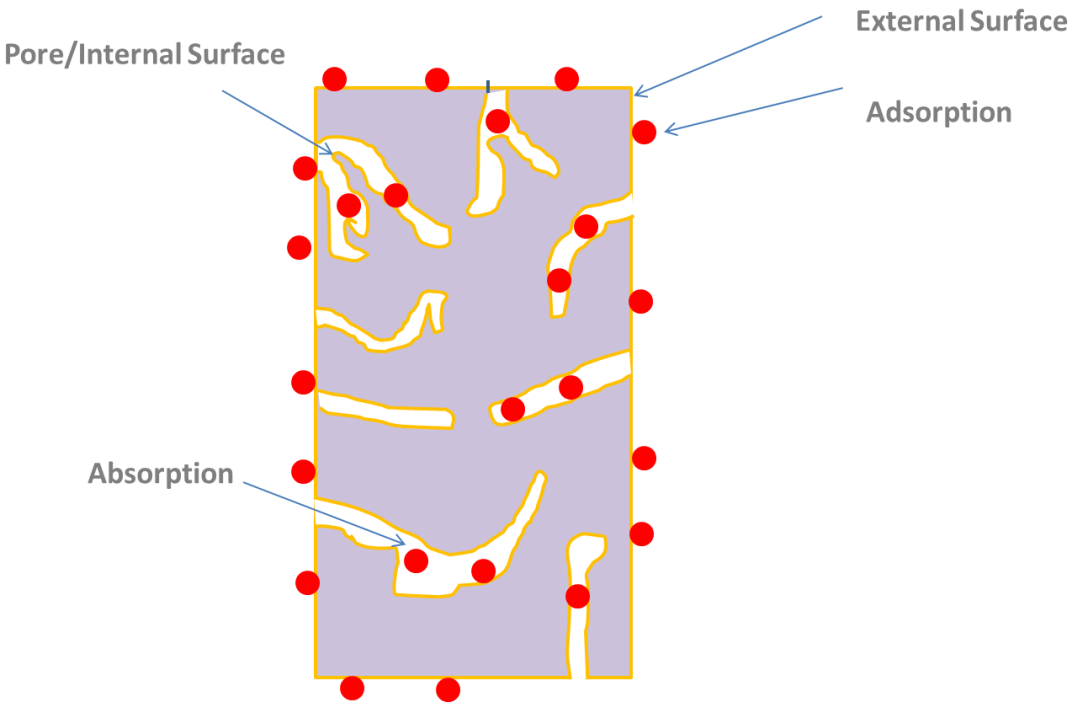

Figure 1.10 Comparison of absorption and adsorption processes

In general, sorption can be classified as chemisorption and physisorption. Chemisorption involves a chemical bond formation between the adsorbent surface and the adsorbate, the enthalpy of desorption for a typical chemisorption process is approximately 100 kJ/mol or greater. Chemisorption involves a strong intermolecular force that results in an irreversible sorption process [48]. Physisorption processes often at the surface by multiple intermolecular forces such as van der Waals, hydrogen bonding, and dipole-dipole interactions. In physisorption process, the enthalpy of desorption ranges up to 80 kJ/mol and results in a reversible sorption process [48].

1.4.2 Solution vs. Gas based adsorption

Gas based adsorption involves non-covalent attachment of gas molecules with an adsorbent [48]. A solution based adsorption process is the displacement of solvent molecules on the adsorbent surface by an adsorbate species from solution [49]. Figure 1.11 illustrates these two adsorption processes.

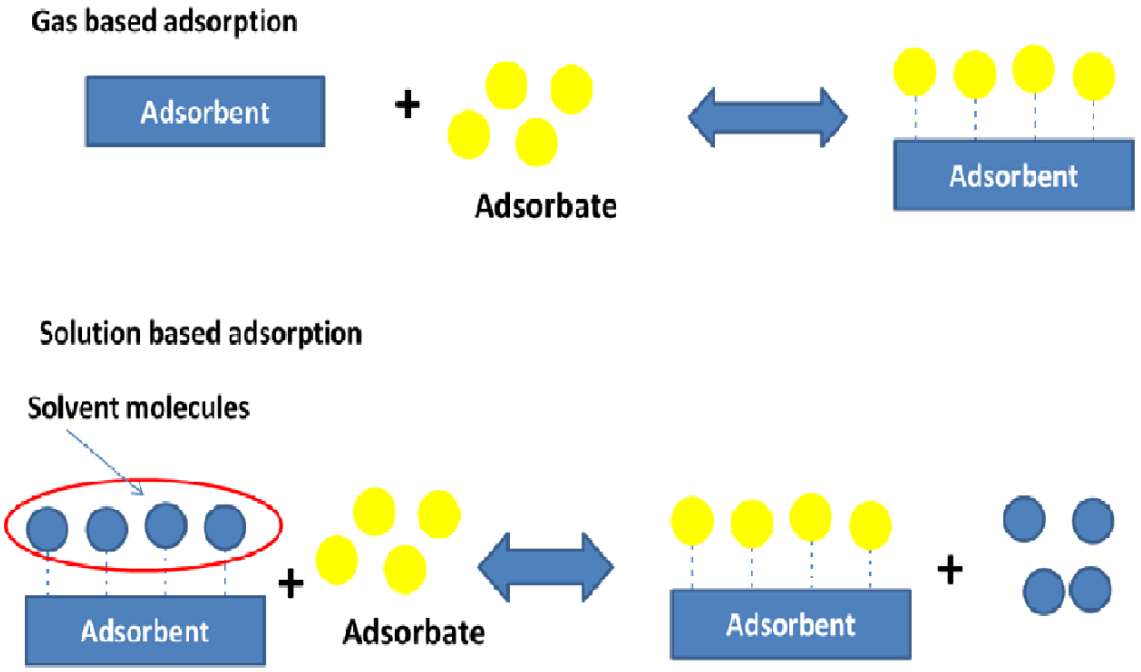

Figure 1.11 Gas phase and solution phase adsorption

1.4.3 Types of isotherms

According to the International Union of Pure and Applied Chemistry (IUPAC), there are six general types of adsorption isotherms which are shown in Figure 1.12 [50]. The shapes of adsorption isotherms are greatly affected by the pore size (pore diameter) and surface area of the adsorbent. Adsorbents with different pore diameters are classified as Macropores (>50 nm), Mesopores (2-50 nm), and Micropore (<2 nm).

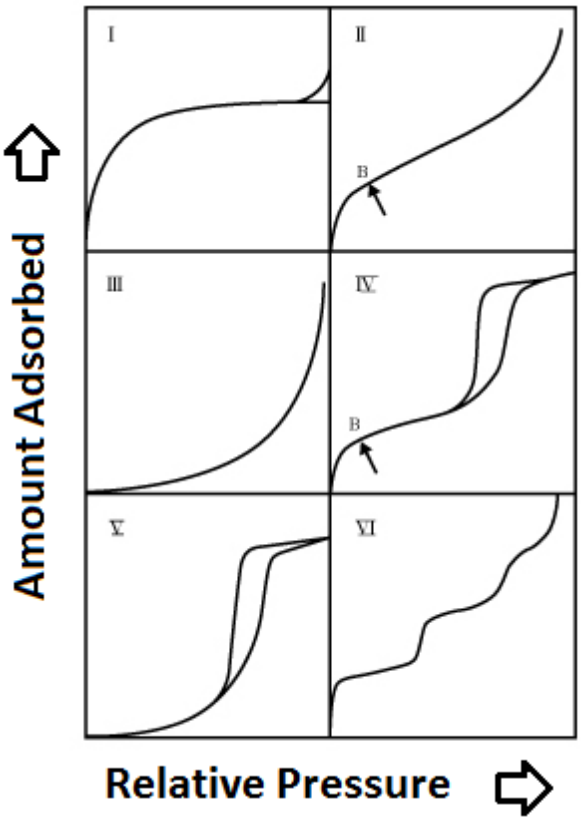

Figure 1.12 Various types of sorption isotherms for gas adsorption [24]

Type I

This adsorption isotherm has a plateau which indicates a specific sorption capacity of the sorbents. Adsorbents with microporous pores like granular activated carbon (GAC) and zeolite have a very small cross-sectional area which cannot allow more than one adsorbate species to fit within a pore.

Type II

Two possible adsorption processes can be described by this adsorption isotherm, one is a non-porous material where the sorption sites are on the external surface. The other case is adsorbents with large macropores where the surface area of the pore is so large that multilayer adsorption can occur without restrictions. The point B is an indication that the monolayer coverage is complete.

Type III

Strong adsorbate and adsorbate interaction can exceed the interaction between the adsorbate and adsorbent which will result in this type adsorption isotherm.

Type IV

This type of adsorption isotherm exhibits a hysteresis loop, where this is typical for mesoporous adsorbents. At low pressure, an adsorbent monolayer is formed on the adsorbent pore surface firstly. The subsequent multilayer formation of adsorbents will be formed as the adsorbate pressure increases.

Type V

Type V adsorption isotherm contains hysteresis loops which indicate the agglomerated particles desorb at once as a collective group. It also reveals finite sorption sites which cause a plateau to be seen because of the weak interactions between adsorbate fluid and the adsorbent surface sites.

Type VI

This type of curve shows a multilayer adsorption process and a stepwise adsorption from the external surface to internal surface and pores. Adsorbates fill the adsorption sites following the energy requirement for each type adsorption site.

1.4.3.1 Hysteresis in solid-gas adsorption/desorption curves

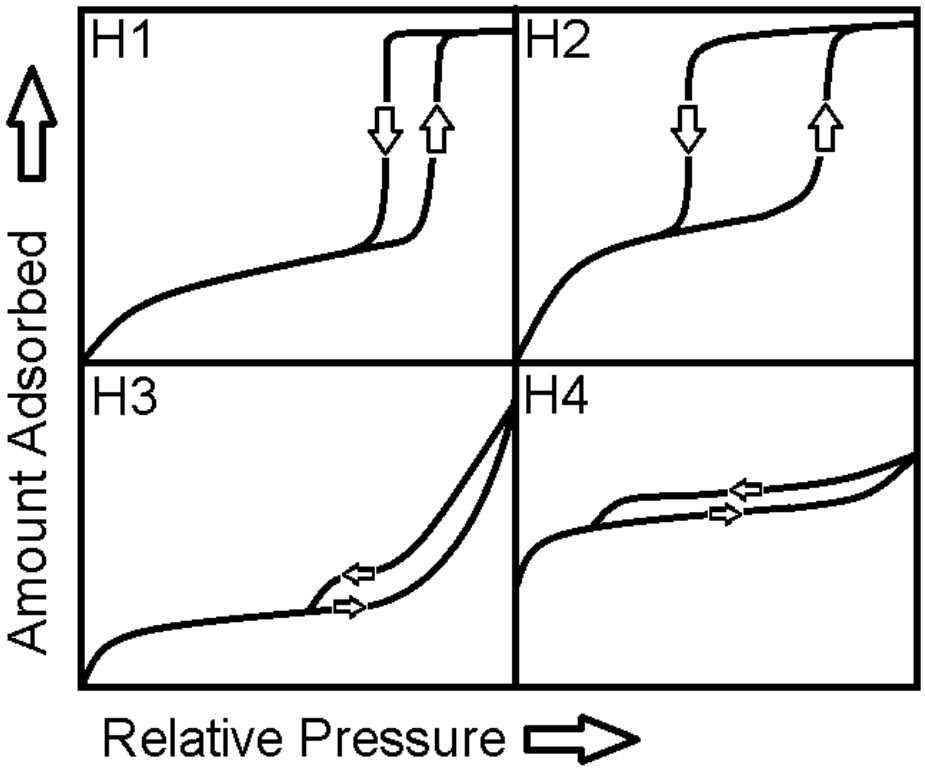

Figure 1.13 General types of hysteresis loops observed for nitrogen adsorption and desorption as defined by IUPAC [52]

Four types of hysteresis are shown in Figure 1.13. These different profiles of adsorption curves relate to different pore shapes of adsorbents [50]. When the relative pressure of nitrogen gas increases to unity, condensation occurs inside the pores. The adsorption isotherm obtained can reveal the shape of the pore before condensation.

Type H1

Gas molecules such as N_2 can adsorb into the sides of the pores to form a monolayer firstly that continue to form a multilayer until the pore is filled. Adsorbents with cylindrical pores can result in this kind isotherm [50].

Type H2

The H2 adsorption isotherm shows the adsorption process as very similar to H1, but there is a region inside the pore that is difficult to fill [50]. The desorption isotherm profile is usually understood as a sign of interconnection of the pores. For instance, a pore connected to the external vapor phase via a smaller pore, in many cases the smaller pore acts as a neck which is often referred as an "ink-bottle" pore.

Type H3

The broad type H3 adsorption isotherm shows the monolayer coverage, the interaction between adsorbates on the first layer and the n^{th} layer is relatively weak. The presence of thin slit-like capillary pores can result in this type of desorption curve [50].

Type H4

The adsorption isotherm provides an indication of microporosity of the adsorbent and strong adsorbent-adsorbate interactions [50]. The desorption profile also indicates the presence of slit-shaped pores within the adsorbent phase.

1.4.4 Models of sorption isotherms

1.4.4.1 Langmuir isotherm model

The Langmuir model assumes monolayer adsorption with a finite number of binding sites that are homogeneously distributed over the adsorbent surface, where no interaction occurs between adsorbed species, [51] described by Equation 1.1:

$$Q_e = \frac{Q_m K_L C_e}{(1+K_L C_e)} \qquad (1.1)$$

Q_m is the maximum amount of the adsorbate bound onto the monolayer of the adsorbent, Q_e is the amount of the adsorbate bound at equilibrium, C_e is the unbound adsorbate concentration in solution at equilibrium, and K_L is the Langmuir adsorption constant.

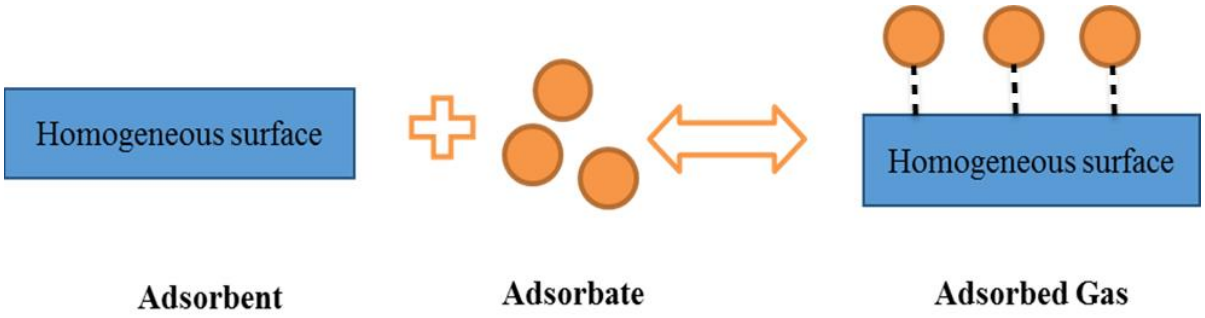

Figure 1.14 Langmuir model of physical adsorption of a gas onto a solid adsorbent.

1.4.4.2 Freundlich isotherm model

The Freundlich model resembles the Langmuir model, except it assumes that the sorbent has a heterogeneous surface with nonequivalent binding sites with variable binding affinity [52], as described by Equation 1.2:

$$Q_e = K_f C_e^{\frac{1}{n}} \qquad (1.2)$$

Q_e is the amount of the adsorbate bound onto the adsorbent at equilibrium, while K_f and n are the Freundlich adsorption constants for a given adsorbent-adsorbate system at specific conditions.

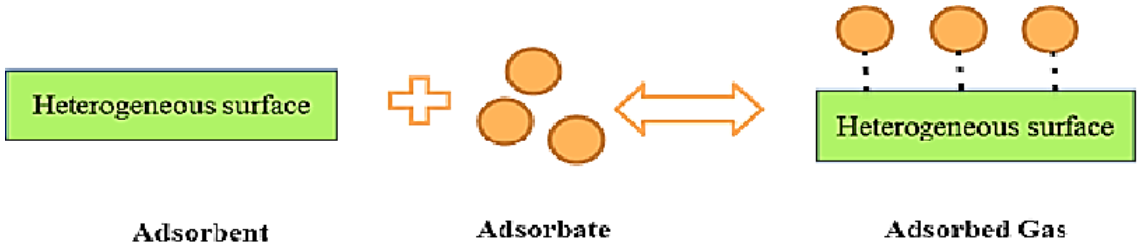

Figure 1.15 Freundlich isotherm model of physical adsorption of gas where surface heterogeneity sites are part of the adsorbent surface.

1.4.4.3 The BET (Brunauer-Emmett-Teller) adsorption isotherm

The BET model is a theoretical equation and an extended form of the Langmuir isotherm by accounting for multilayer surface coverage [53]. Several assumptions are made in this model: 1) the adsorbent surface is assumed to be uniform and homogeneous, so that the Langmuir theory can be applied to each layer; 2) there are no lateral molecular interactions between each adsorption layer; and 3) infinite multiple layers adsorption of gas molecules on a solid is achievable. The resulting BET equation is expressed in Equation 1.3:

$$\frac{1}{v\left[\left(\frac{P_o}{P}\right)-1\right]} = \frac{c-1}{v_m c}\left(\frac{P}{P_o}\right) + \frac{1}{v_m c} \qquad (1.3)$$

P and P_o are the equilibrium and the saturation pressure of adsorbates at the temperature of adsorption, v is the volume of adsorbed gas, and v_m is the volume of monolayer adsorbed gas. c is the BET constant, which is expressed by Equation 1.4:

$$c = \exp\left(\frac{E_1 - E_L}{RT}\right) \qquad (1.4)$$

E_1 is the heat of adsorption for the first layer, and E_L is the heat of liquefaction of the layers on top of the first layer. From Equation 1.3, a graph with the y-axis for the $1 / v[(P_o / P) - 1]$ and x-axis for the relative pressure P / P_o can be plotted according to the experimental results. This type of isotherm is called a BET plot.

$$v_m = \frac{1}{S+I} \qquad (1.5)$$

S is the value of the slope and I is the value of y – intercept

$$c = 1 + \frac{S}{I} \qquad (1.6)$$

According to experimental observation, the linear relationship of Equation 1.3 is maintained only in the range of $0.05 < P / P_o < 0.35$ [53]. The values of the volume of monolayer adsorbed gas v_m and the BET constant *c* are calculated from Equation 1.5 and Equation 1.6. The total surface area S_{total} and the specific surface area S_{BET} are calculated by Equation 1.7 and Equation 1.8.

$$S_{total} \frac{(v_m N s)}{V} \qquad (1.7)$$

$$S_{BET} \frac{S_{total}}{m} \qquad (1.8)$$

Where *N* is Avogadro's number, *V* is the molar volume of the adsorbate gas, and *m* is the mass of the solid sample or adsorbent, and v_m is in units of volume which are also the units of the monolayer volume of the adsorbate gas, *s* is the adsorption cross-section of the adsorbed species. The disadvantages of this adsorption model are as follows: 1) surface is assumed to be homogenous which is not always true; 2) molecular interactions between each layer of adsorbed molecules are neglected; 3) it is not always valid to assume that the heat of adsorption from the second layer will be equal to subsequent layers.

1.4.5 Models of sorption kinetics

1.4.5.1 PFO (Pseudo-first-order) kinetics

The PFO kinetic model originally proposed by Lagergren and Svenska [54] has been widely used to describe kinetic adsorption processes. The PFO model assumes a large number of available adsorption sites, as described by Equation 1.9.

$$q_t = q_e(1 - e^{-k_1 t}) \qquad (1.9)$$

q_e and q_t are the amounts of adsorbate adsorbed (mg/g) at steady state and variable time (t; min) by the adsorbent.

1.4.5.2 PSO (Pseudo-second-order) kinetics

The experimental uptake (q_e) the amounts of roxarsone adsorbed (mg/g) at steady state can be calculated from the PSO model, according to Equation 1.10.

$$q_t = \frac{k_2 {q_e}^2 \mathrm{t}}{(1+k_2 q_e t)} \qquad (1.10)$$

The PSO rate constant (k_2) is determined from a non-linear fit while q_t are the amounts of roxarsone adsorbed (mg/g) at variable time (t; min) by the adsorbent.

1.5 Application of Physical Adsorption: Goethite, Ferrihydrite, and Hematite

Iron oxides represent mineral phases that consist of iron and oxygen. There are sixteen known iron oxides and hydrous ferric oxides (HFO) [26]. Hydrous ferric oxide is a class of minerals that contain iron (Fe), hydroxyl groups (-OH), and weakly bound water. They are normally poorly crystalline, highly porous and have large surface areas. Goethite and ferrihydrite are both considered as hydrous ferric oxide with chemical formulae; FeOOH and Fe_2O_3•$0.5H_2O$. Accordingly, HFO is a 2-line ferrihydrite that has been reported as a classic sorbent for diverse adsorption studies. Dzombak and Morel (1990) reported on the use of ferrihydrite as an adsorbent; however, ferrihydrite is unstable and transforms into hematite [55]. Hence, goethite and hematite have attracted much attention by their utility as adsorbents and their abundance in nature. Goethite has been used as a model adsorbent because of its well-defined crystal structure since it can be synthesized readily in the laboratory.

Goethite, ferrihydrite, and hematite have been widely used to adsorb simple inorganic anions, oxyanions and organic ions. Table 1.5 lists the technological applications that use goethite, ferrihydrite and hematite materials for anion species removal:

Table 1.5 Adsorption application of goethite, ferrihydrite and hematite materials towards anion species

Oxide	Anion	Reference
Goethite	Arsenate/Arsenite (Inorganic)	[56], [57], [58]
	Borate (Inorganic)	[59], [60]
	Carbonate (Inorganic)	[61]
	Chloride (Inorganic)	[62]
	Fluoride (Inorganic)	[62], [63]
	Iodate (Inorganic)	[64]
	Molybdate (Inorganic)	[59]
	Phosphate (Inorganic)	[65], [66], [67]
	Selenate/Selenite (Inorganic)	[68], [69]
	Silicate (Inorganic)	[70]
	Sulphate (Inorganic)	[71], [72]
	Carboxylic acids (Organic)	[73]
	Citrate (Organic)	[67], [74], [75]
	EDTA (Organic)	[76]
	Humic acids (Organic)	[77], [78]
	Lactate (Organic)	[74], [75]
	Phenols (Organic)	[79]
	2,4 – D (Organic)	[80], [81]
Ferrihydrite	Arsenite/Arsenate (Inorganic)	[82], [83]
	Carbonate (Inorganic)	[84]
	Fluoride (Inorganic)	[85]
	Phosphate (Inorganic)	[86], [87]
	Silicate (Inorganic)	[88], [89]

	Sulphate (Inorganic)	[90]
	Chromate (Inorganic)	[91]
	Phenols (Organic)	[79, 80]
	Quinmerac (Organic)	[29]
	2,4-D (Organic)	[80]
Hematite	Sulphate (Inorganic)	[92]
	Arsenate (Inorganic)	[93]
	Methylene blue (Organic)	[94]
	Congo red (Organic)	[95]

Using goethite, ferrihydrite, hematite to adsorb cations involves interaction with deprotonated surface hydroxyl groups to form mono- and bi-nuclear, inner-sphere complexes. Cation adsorption is initially fast onto hydrous ferric oxide, but adsorption of trace metals can continue for days before attaining equilibrium. Since the cation adsorption is not a focus of this research work, the Table 1.6 briefly lists the cation adsorption studies onto iron oxide materials.

Table 1.6 The cation adsorption studies of iron oxides.

Oxide	Cation	Reference
Goethite	Al^{3+}	[78], [96]
	Cu^{2+}	[97] , [98]
	Co^{2+}	[98], [99]
	Hg^{2+}	[100], [101]
	Mg^{2+}	[102]
	U^{6+}	[103]
Ferrihydrite	Ca^{2+}	[104]
	Co^{2+}	[105]
	U^{6+}	[106]
	Zn^{2+}	[107], [108]
Hematite	Pb^{2+}, Ni^{2+}	[109], [92]
	Cd^{2+}	[110], [92]
	$As^{2+, 3+, 5+}$	[111], [92]

1.6 Application of Physical Adsorption: Cellulose and Cellulose Based Materials

Because of the interparticle dipole forces, iron oxide NPs tend to aggregate into large particles [112] which lead to the loss of size effect and the decrease of specific surface area. In order to avoid the agglomeration, many materials such as carbon nanotubes [113], reduced graphene oxide [114], silica microspheres [115], and bacterial cellulose [116] have been used as template to disperse magnetic NPs. Because cellulose is one of the most abundant and renewable biopolymers on earth, cellulose has been considered a good candidate for the immobilization of these NPs [21]. Therefore, composites of cellulose and iron nanomaterials are very promising in many applications.

Researchers have modified cellulose fibers chemically to remove cation organic dyes in wastewater [23]. Hokkanen's group used magnetic NP activated microfibrillated cellulose to remove inorganic arsenic (V) species [18]. Yu and Tong's group also discovered a simplified method for producing the magnetic iron oxide coated cellulose in "a one-step process" to remove inorganic arsenic species [17]. In this research, iron oxide coated cellulose was used for removal of anionic organoarsenical species such as ROX.

1.7 Purpose of the Research

Arsenic species are very toxic. Long-term exposure to arsenic from drinking water and food can be cancerous [10]. Hence, effort should be made to keep arsenic levels in drinking water as low as possible. Although there are various arsenic removal technologies available, the adsorption method is often preferred due to its cost effectiveness and simple operational requirements [117]. This thesis presents the progress made in the research on the preparation of cellulose supported iron oxides NPs (goethite and hematite) composite adsorbent materials and the use of such materials for the adsorption of arsenic species in aqueous solution at variable conditions.

1.8 Objectives

The overall objective for this research is to develop an environmental friendly iron oxide coated cellulose composites to remove organoarsenical species in an aqueous environment.

1) to prepare and characterize iron oxides onto cellulose supports and mineral phases in the absence of supports;
2) to evaluate the adsorption properties of iron oxides and their supported forms with selected adsorbates (PNP, Roxarsone, and nitrogen gas);
3) to develop improved iron oxide–cellulose composite materials with enhanced adsorption properties;
4) to study the structure-function properties of goethite-cellulose and hematite-cellulose composite materials' that relate to the adsorption process.

CHAPTER 2 : MATERIALS AND METHODS

2.1 Introduction

In this section, instruments used in the study and this report will be described. Materials and the synthesis protocol for both of the goethite/hematite and their cellulose composite are also provided in this chapter.

2.2 Materials

Ferric chloride hexahydrate ($FeCl_3$• $6H_2O$), sodium hydroxide (NaOH), Ferric nitrate nanohydrate ($Fe(NO_3)_3$•$9H_2O$), potassium hydroxide (KOH), *p*-nitrophenol and cellulose (medium fiber derived from cotton linters) were obtained from Sigma-Aldrich Canada Ltd. (Oakville, ON). Roxarsone used was from Haohua Industry Co. Ltd. (Jinan, China). Roxarsone was purified via recrystallization by dissolving 5 g of roxarsone in 125 mL of millipore water at 65 °C with stirring, this solution was then hot filtered through Whatman No.2 filter paper at the ambient condition. The filtrate solution was allowed to cool slowly before being placed in a refrigerator for 24 h. The recrystallized product was light yellow-orange in color and was recrystallized further until a homogeneous light yellow product remained. The final pure light yellow color roxarsone product was isolated through filtration and dried at 50 °C in a vacuum oven.

2.3 Synthesis

2.3.1 Preparation of the goethite and goethite-cellulose composite materials

The synthesis of the goethite was modified from a previous report [21]. The slow addition of 20 mL of 0.4 M ($FeCl_3$• $6H_2O$) was made into a basic solution of Millipore water (170 mL) containing 10 mL of 4.0 M NaOH. A dark red-orange colored precipitate formed immediately and

the slurry was further stirred for 24 h until a green-yellow goethite precipitate was formed. The product was filtered through Whatman No. 42 filter paper and washed with Millipore water. The product was repeatedly washed with water until the conductivity of the filtrate was ca. 30 µS/cm and finally dried in an oven at 70 °C for two days with a final yield of 98%, in agreement with another reported study [118].

The synthesis of goethite-cellulose composites was carried out in a 250 mL plastic beaker using commercial bulk cellulose (2 g, 5 g or 10 g) with 6 g NaOH with mixing in 100 mL of Millipore water and heating to 70℃, followed by the slow addition of a hot 70℃ solution of 8.11 g $FeCl_3$• $6H_2O$ in water (100 mL). Fe^{3+}/OH^- was fixed at the 1:5 mole ratio. The slurry was mixed at ambient conditions and aerated for 1 h until a brown-yellow color solution appeared. The slurry was oven dried at 70℃ for ca. 12 h. The dried materials were washed with excess Millipore water and the filtrate was passed through Whatman no. 42 filter papers until the conductivity of the filtrate was ca. 30 µS/cm. The final product was oven-dried at 70 °C for two days. These products were referred to as 30% Fe coated GC (2 g), 20% Fe coated GC (5 g), and 10% Fe coated GC (10 g) according to their variable iron loadings in parentheses. Scheme 2.1 illustrates a proposed synthetic pathway for the formation of goethite-cellulose composite materials.

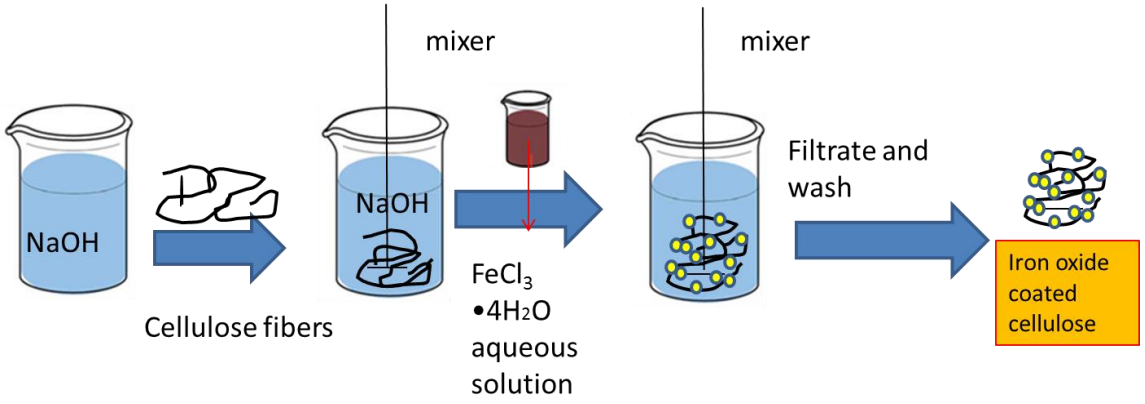

Scheme 2.1 Synthetic scheme for the formation of goethite-cellulose composite materials

2.3.2 Preparation of the hematite and hematite-cellulose composite materials

The synthesis of the hematite NPs was prepared by dissolving 40 g $Fe(NO_3)_3 \bullet 9H_2O$ in 500 mL DI water and titrate with 1 M KOH solution to pH 7, the reddish precipitate was filtered through Whatman No. 42 filter papers and washed with Millipore water. The product was repeatedly washed with water until the conductivity of the filtrate was ca. 30 µS/cm. The product was dried in an oven at 70 °C for 18 h, the drying process produced hematite by transferring from ferrihydrite [119].

Three different Fe loaded hematite-cellulose materials were synthesized. To synthesize HeCell-3 with 5% Fe loading, first dissolve 5.38 g $Fe(NO_3)_3 \bullet 9H_2O$ into 20 g Millipore water in a 100 mL beaker and then heat to 75°C and add 14 g of cellulose into a glass beaker containing ferric nitrate solution and mix. In another beaker prepare 1 M KOH solution and heat to 75 °C; titrate the KOH solution into the iron (III) nitrate and cellulose mixture until the final pH of the slurry was around 7. The precipitates were filtered with No.42 quantitative filter papers, and then dried in oven at 90 °C for 8 h; after that these precipitates were washed with excess Millipore water until the conductivity of the filtrate was ca. 30 µS/cm. The final products were dried in an oven at 70 °C for 18 h. The synthesis of 10% and 25% Fe coated hematite-cellulose are similar to the synthesis of 5% Fe coated hematite-cellulose, where the only difference relates to the addition of different amount of cellulose fibers. For the 10% and 25% Fe coated hematite-cellulose, 7 g and 2.8 g of cellulose fibers are used in the synthesis.

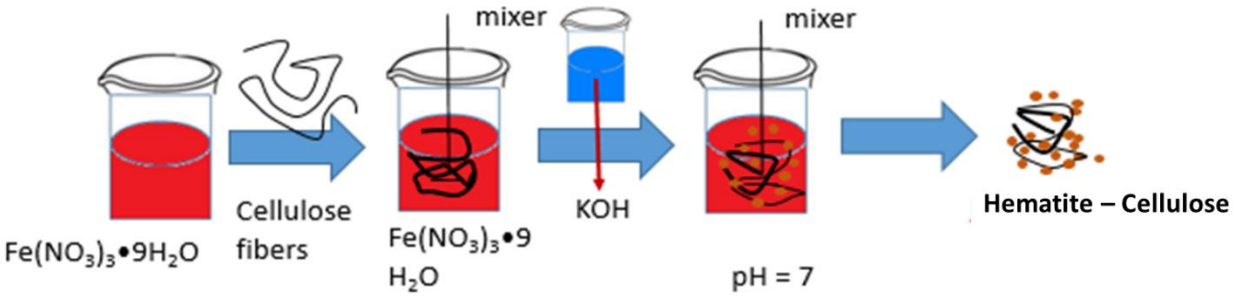

Scheme 2.2 A proposed pathway for the formation of hematite-cellulose composite materials

2.3.3 Preparation of ferrihydrite NPs materials

The synthesis of the ferrihydrite NPs was prepared by dissolving 40 g $Fe(NO_3)_3 \bullet 9H_2O$ in 500 mL DI water and titrate with 1 M KOH solution to pH 7, the reddish precipitate was filtered through Whatman No. 42 filter paper and washed with Millipore water. The product was repeatedly washed with water until the conductivity of the filtrate was ca. 30 µS/cm. The product was air dried for 72 h [119].

2.4 Instrumental Analysis

2.4.1 TGA

The thermogravimetric analysis (TGA) of materials was carried out using a TA instruments (Model Q50) thermal analyzer. Nitrogen gas was used for cooling and purging of the sample compartment, where samples were analyzed between 30 °C and 500 °C at a heating rate of 10 °C /min.

2.4.2 FT-IR spectroscopy

The Fourier Transform infrared (FTIR) spectra of the powder form samples were obtained with a BioRAD FTS-40 spectrophotometer, where samples were diluted with KBr (FTIR grade, Alfa Aesar) at 10% (w/w) and scanned (n = 256) from 4000 to 400 cm^{-1} with an instrument resolution of 4 cm^{-1}.

2.4.3 Raman spectroscopy

Raman spectra were acquired with a Renishaw Invia Raman Microscope where the spectral shifts were obtained at ambient temperature with an argon ion laser at an excitation wavelength of

786 nm. The spectra were recorded over the rang 200 cm^{-1} to 2000 cm^{-1} using an operating spectral resolution of 1.9286 cm^{-1} of Raman shift. Instrument parameters used an optimized power (1 mW) to prevent sample decomposition, 50× objective lens magnification, and 50 scans with a 10 s integration time. Raman spectra of the dry ROX, dry adsorbents before ROX sorption and wet adsorbents after ROX sorption were obtained through observations from a gold coated microscope glass.

2.4.4 TEM

The transmission electron microscopy (TEM) images of samples were obtained using a Hitachi HT-7700 microscope with a 100 kV voltage. Samples were prepared by dispersing samples in ethanol solution in a sonication bath, them depositing a drop of sample in ethanol onto a carbon-coated copper TEM grid without staining. The samples were examined under 50 (500k × magnification), 100 (250k × magnification), 200 (125k × magnification), and 500 (50k × magnification) nm scales.

2.4.5 pXRD

Powder X-ray diffraction (pXRD) was used to monitor the product phase variation at variable iron oxide compositions using a diffractometer (Model: Empyrean, manufacturer: PANalytical, The Netherlands) fitted with Cu K-alpha X-ray irradiation sources. pXRD results obtained herein for the iron oxides were compared to the simulated spectra from the X'pert Highscore Plus software (Ver. 3.0b (3.0.2), PANalytical, Almelo, The Netherlands).

2.4.6 N_2 adsorption–desorption analysis (BET)

The specific surface areas of goethite, hematite, ferrihydrite and different Fe coated goethite-cellulose, and different Fe coated hematite-cellulose composites were measured by

Micromeritics ASAP 2020 (ver. 3.04). N_2 adsorption–desorption analysis (BET) of the specific areas' accuracy was ±5%. Approximately 200 mg samples were measured with a degassing temperature at 100 °C prior to analysis.

2.4.7 Solid state ^{13}C NMR spectroscopy

^{13}C solid state NMR experiments were performed using a Bruker AVANCE III HD spectrometer operating at 125.77 MHz (^{1}H frequency at 500.13MHz), with a 4 mm DOTY CP-MAS probe. The ^{13}C CP/TOSS (Cross Polarization with Total Suppression of Spinning Sidebands) experiments were carried out at a spinning speed of 6 kHz, a ^{1}H 90° pulse of 3.5 µs, and contact time of 0.75 ms, with a ramp pulse on the ^{1}H channel. For all the samples, 5120 scans were accumulated, with a recycle delay of 2 s. All experiments were recorded using 71 kHz SPINAL-64 decoupling during acquisition. Chemical shifts are referenced to adamantane at 38.48 ppm (low field signal).

2.4.8 Iron coating efficiency

Samples were digested by dissolving approximately 0.1 g in 10 mL of nitric acid (conc.), to which was added 30 mL of hydrochloric acid (conc.) in a beaker. A graduated cylinder was used to deliver the correct acid volumes. Once the digestion was completed, the mixture was allowed cool then added it slowly to a 100 mL volumetric flask containing approximately 30 mL of Millipore water. The volumetric flask was diluted to mark with Millipore water and mixed well. The recommended linear range of response for atomic spectroscopic measurements of iron was 2.5 to 10 ppm. A 100 ppm iron standard was diluted to 3, 4, 5, 6, 7, 8, 9 ppm to produce a calibration curve. the acid digested solution that contained samples 10× was diluted further to ensure the results fall into the calibration curve and then back calculated the iron content in the samples from

the dilution factor. Perkin Elmer Atomic Absorption Spectrometry (AAS) iCE 3300 AA with Iron Atomax hollow cathode 1.5 lamp was used for this analysis.

2.5 Sorption Measurements

2.5.1 Roxarsone adsorption isotherms

2.5.1.1 Roxarsone adsorption isotherms of the goethite and goethite-cellulose composites

An isotherm study of roxarsone uptake was conducted in a batch mode with accurately known amounts of adsorbent (ca. 35 mg). Each adsorbent was dispensed into 15 mL "Falcon" conical plastic centrifuge tubes containing ROX solution (7 mL) at variable pH (4, 5, 6, 7, and 8) and initial concentrations (0.05 mM to 1.5 mM). The samples were covered to minimize exposure to light while mixing on a shaker table at 250 RPM at 295 K for 24 h. After attaining equilibrium, 60 µL of the supernatant solution was isolated after centrifuging and subsequent dilution with 2.94 mL of pH 7 phosphate buffer to enable analysis of absorbance over a linear calibration range in triplicate fashion. Two different adsorption models were used to analyze isotherm adsorption data.

2.5.1.2 Roxarsone adsorption isotherms of the hematite and hematite-cellulose composites

An isotherm study of roxarsone uptake was conducted in a batch mode with accurately known amounts of adsorbents (ca. 35 mg). Each adsorbent was dispensed into 15 mL "Falcon" conical plastic centrifuge tubes containing ROX solution (7 mL) at pH 7 and initial concentration

(0.05 mM to 1.50 mM) values. The samples were covered to minimize exposure to light while mixing on a shaker table at constant speed (250 RPM) at 295 K for 24 h. After attaining equilibrium, 0.5 mL of each sample was withdrawn and centrifuged. 60 µL of supernatant solution was isolated after centrifuging and subsequent dilution with 2.94 mL of pH 7 phosphate buffer to enable UV-vis spectrophotometric analysis within a linear calibration range. Triplicate measurements were made to obtain average estimates of uptake, according to the calibration curve. Two adsorption models (Langmuir and Freundlich) were used to analyze isotherm adsorption data.

2.5.2 Roxarsone adsorption kinetics

2.5.2.1 Roxarsone adsorption kinetics of the goethite & goethite-cellulose composites

Kinetic uptake was carried out by modifying a one-pot experiment [120] where ca. 0.7 g of adsorbent was added into 200 mL of roxarsone solution (1.5 mM). The conical sharp Whatman no. 42 filter paper (5.5cm diameter) was placed on the of the ROX solution as a barrier to prevent sampling the solid adsorbents. Figure 2.1 shows the setup for the adsorption kinetics experiments. The adsorption kinetics was studied over a 90 min interval where the roxarsone solution was adjusted to pH 3 and mixed before the addition of the adsorbent. 150 µL samples were taken at different time intervals and centrifuged. 60 µL of the supernatant solution was isolated after centrifuging and subsequently diluted with 2.94 mL of phosphate buffer at pH 7 prior to absorbance measurements. The uptake of roxarsone by the various adsorbents was analyzed using Equation 1.9 and Equation 1.10 from the chapter 1. The uptake kinetics for the goethite and the composite materials were carried out similarly apart from the variable sorbent dosage.

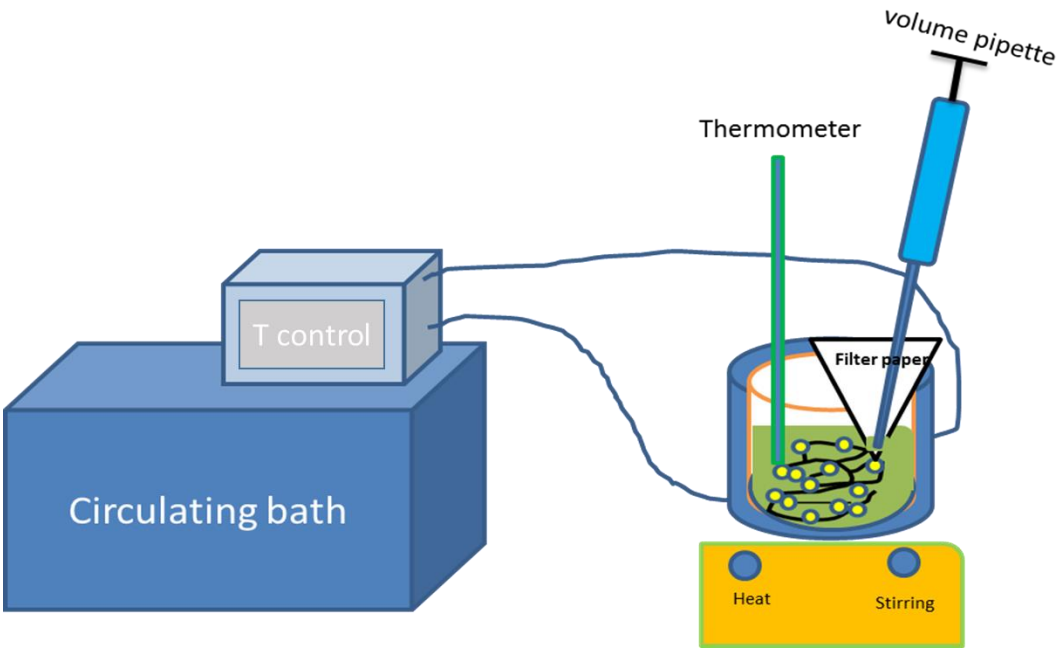

Figure 2.1 An illustration of the "filter barrier" setup for kinetic uptake studies

2.5.2.2 Roxarsone adsorption kinetics of the hematite & hematite-cellulose composites

Kinetic uptake was carried out by modifying a one-pot experiment [120] where ca. 0.4 g of adsorbent was added into 80 mL of roxarsone solution (1.5 mM). The experimental setup for the measurement of adsorption kinetics was similar as illustrated in Figure 2.1. The conical sharp Whatman no. 42 filter paper (5.5 cm diameter) was placed in the ROX solution as a barrier to prevent sampling the solid adsorbents that are dispersed in the main volume of the vessel. The adsorption kinetics was studied over a 90 min interval where the roxarsone solution was adjusted to pH 7 and mixed before the addition of the adsorbent. 150 µL samples were taken at different time intervals and centrifuged. 60 µL of the supernatant solution was isolated after centrifuging and subsequently diluted with 2.94 mL of phosphate buffer at pH 7 prior to absorbance measurements. The roxarsone solution uptake by the various adsorbent systems was analyzed using Equation 1.9 and Equation 1.10. The measurement of the adsorption kinetics for the hematite material and the hematite-cellulose material was carried out similarly, except that variable adsorbent dosage was used for hematite vs. composite materials.

2.5.3 Adsorption thermodynamic study

The adsorption thermodynamic study of roxarsone was done by studying the uptake properties with 10% Fe coated hematite-cellulose composite at different temperatures. Figure 2.1 showed the setup for the adsorption kinetic experiments, where the temperature water bath was used to conduct the experiments at 5, 15 and 25℃. 1.5 mM ROX solution was cooled to required temperature, 1 g of the adsorbent was added into this 1.5 mM ROX solution. 150 µL of sample was taken at different time intervals to evaluate the ROX concentration during the adsorption process.

2.5.4 Regeneration study

The regeneration study was carried out using the 10% Fe coated hematite-cellulose and 0.6 M NaOH caustic solution to wash off the ROX on the adsorbent surface. The volume of the regeneration fluid used in each washing cycle was recorded. Figure 2.2 shows the experimental setup for the regeneration process. The procedure was as follows: 1 g of used adsorbent was filtered out by 45 µm screen and air dried on the screen. For each regeneration cycle 20 mL of 0.6 M NaOH solution was poured onto the adsorbent placed on a No. 42 filter paper in a filtration funnel, the eluent was collected in a glass bottle. 60 µL sample was withdrawn from the eluent and further diluted with 2.94 mL pH 7 phosphate buffer to determine the ROX concentration from the UV-vis analysis.

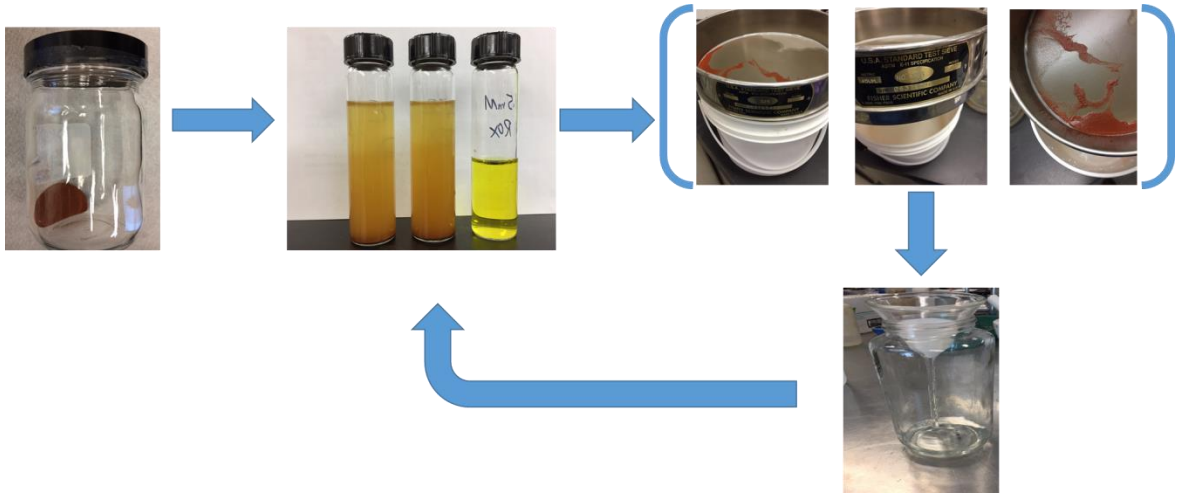

Figure 2.2 Block diagram of adsorption-desorption-stripping cycle

2.5.5 The hydration effect in the ROX adsorption process

The objective was to compare the Raman spectra difference between ROX adsorption in H_2O/D_2O solvent system and pure H_2O system to see the hydration effect in the ROX adsorption process. A pure 300 mL of 5% (by volume) D_2O/ H_2O solvent system without roxarsone was prepared as a blank solution. 60 mL of these 5% (by volume) D_2O/ H_2O solvent were used to make three 20 mL 1.5, 0.75, 0.375 mM ROX in 5% (by volume) D_2O/ H_2O solvent. 0.1 g of hematite added into three different vials contained with 20 mL 1.5, 0.75, 0.375 mM Roxarsone in 5% (by volume) D_2O/ H_2O solvent. The tests were done in triplicate. These vials were placed on a shaker and shook at 250rpm for 18 h to reach equilibrium. These hematite adsorbents were filtered out with 45 um filter paper and carefully dried with Kimwipe tissue for the Raman spectroscopy analysis.

2.6 Error Analysis of Sorption Measurement

Error analysis of the adsorption isotherms was done using the standard error of the regression (S), using the non-linear data fitting method [121], where “S” represents the average distance that the observed values fall from the regression line. The minimization of “S” ensures

that the observed values are closer to the fitted line. The best-fit model used herein involved a minimization of the sum of the standard error (SSE).

2.7 Iron Leaching Tests

To test if iron could be leached out from the composite materials, 0.1 g of the composite materials were soaked in the 100 g DI water and mixed at 300 RPM for 48 h. According to ASTM D3987 (method of shake extraction of solid waste with water), 18 h of extraction time is needed to leach out iron and 48 hours leaching time is adequate in this experiment. 2 mL samples of aqueous solution were taken at 1, 4, 22, 24, and 48 h and filtered by 0.45 μm syringe filters before conducting the iron concentration analysis. The experimental setup for the leaching tests are shown below.

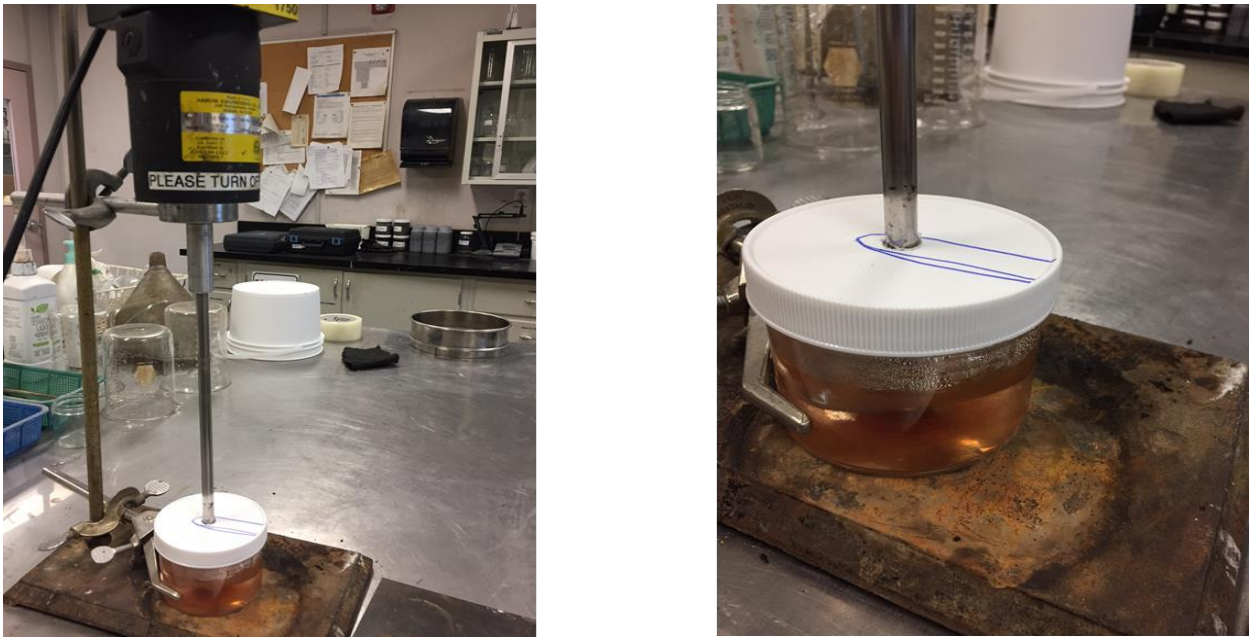

Figure 2.3 Setup for iron leaching tests

CHAPTER 3 : RESULTS AND DISCUSSION: SYNTHESIS AND CHARACTERIZATION OF GOETHITE, HEMATITE, GOETHITE-CELLULOSE, AND HEMATITE-CELLULOSE

3.1 TGA Results

3.1.1 TGA for the goethite and goethite-cellulose composites

The thermal stability of the cellulose, goethite, and composite materials were examined using TGA, as shown in Figure 3.1 a-c. The goethite's TGA graph showed a weight loss before 300 ^{o}C and about 90% of goethite weight loss at 500 ^{o}C, which confirms results obtained by Kosmulski's group [122]. The thermogram for the cellulose in Figure 3.1 c had a notable weight loss between 325 ^{o}C-375 ^{o}C. By comparison, a significant weight loss occurs between 200 to 400 ^{o}C for the 30% Fe coated GC composite (Figure 3.1 b), while the composite showed a thermal event between 150 ^{o}C to 350 ^{o}C, with reduced thermal stability relative to cellulose. The lower thermal stability of composites related to the catalytic decomposition of iron oxide on the organic framework [17].

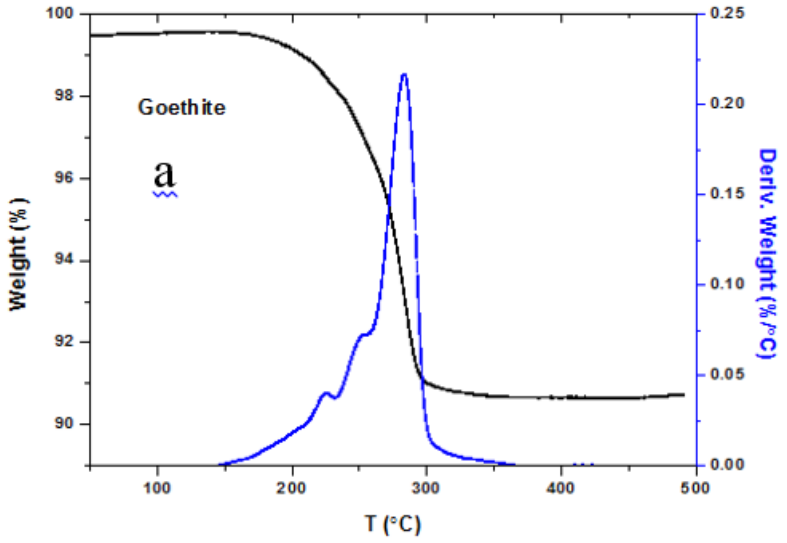

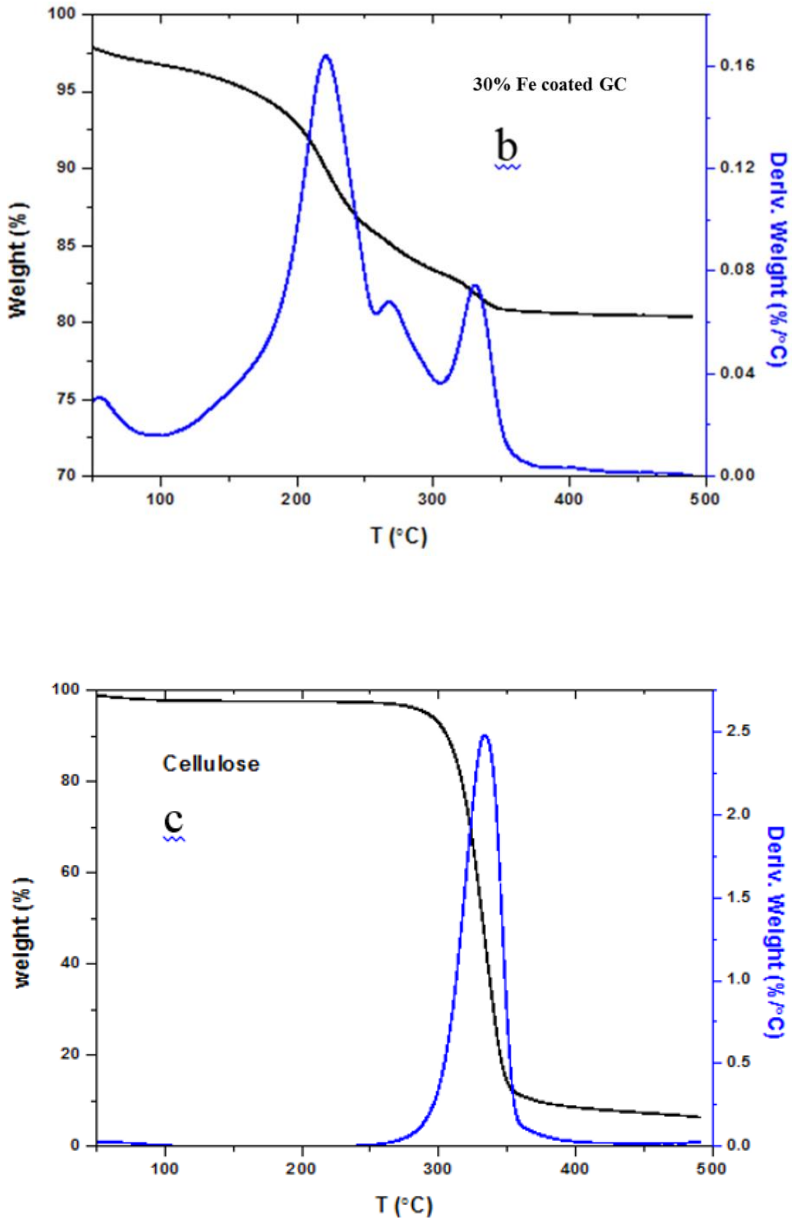

Figure 3.1 TGA results: (a) goethite, (b) 30% Fe coated GC, and (c) cellulose

Figure 3.1 (c) showed a small weight loss occurs between 40-70°C which was attributed to the removal of absorbed water in cellulose [123]. The decomposition steps of the cellulose involved the cleavage of the glycoside linkages of cellulose and produce CO_2, H_2O and a variety of hydrocarbon derivatives. The main weight loss events of cellulose occur over the range of 250°C

to 375°C. In the case of cellulose, the above results are consistent with Poletto's results for the thermal decomposition of the cellulose [124].

3.1.2 TGA for the hematite and hematite-cellulose composites

The thermal stability of the cellulose, hematite and the 10% Fe coated HeCell composite materials were examined using TGA. Figure 3,2 (a) showed hematite losses weight at 80 and 200 °C, the wide peak at 80 °C was because of the iron oxide losses adsorbed water [119]. The observed water lost in hematite TGA analysis could be due to incomplete drying process or because of these hematite nanoparticles were synthesized from further oxidation of ferrihydrite NPs which likely interacts favourably with water molecules. The second peak at 200 °C was from the decomposition of hematite molecules. Figure 3.2 (b) showed a sharp peak at 340 °C from the cellulose decomposition. For the 10% Fe coated HeCell, Figure 3,2 (c) showed three peaks, one small peak around 80 °C, second shoulder peak at 280 °C and a sharp peak at 360 °C. The small peak around 80 °C was due to the water adsorbed in the hematite, the second small shoulder peak at 280 °C was due to the decomposition of the hematite NPs, the third peak at 360 °C was from the decomposition of cellulose. By comparing Figure 3,2 (c) with Figure 3,2 (a) and (b), the decomposition temperature of the 10% Fe coated HeCell composite shifted to a higher temperature than the pure hematite and cellulose material. This proved new composite material was successfully formed and it showed distinct thermal profile features over those containing only pure hematite and cellulose materials. The composite material was also more thermally stable according to the TGA analysis.

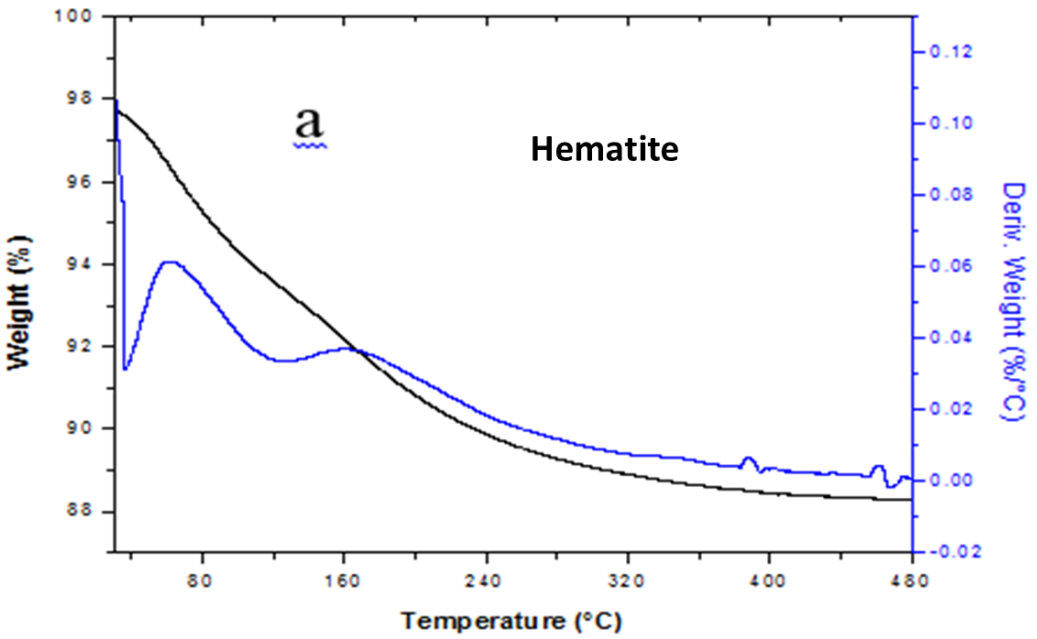
a
Hematite
Weight (%)
Deriv. Weight (%/°C)
Temperature (°C)
100
98
96
94
92
90
88
0.12
0.10
0.08
0.06
0.04
0.02
0.00
-0.02
80
160
240
320
400
480

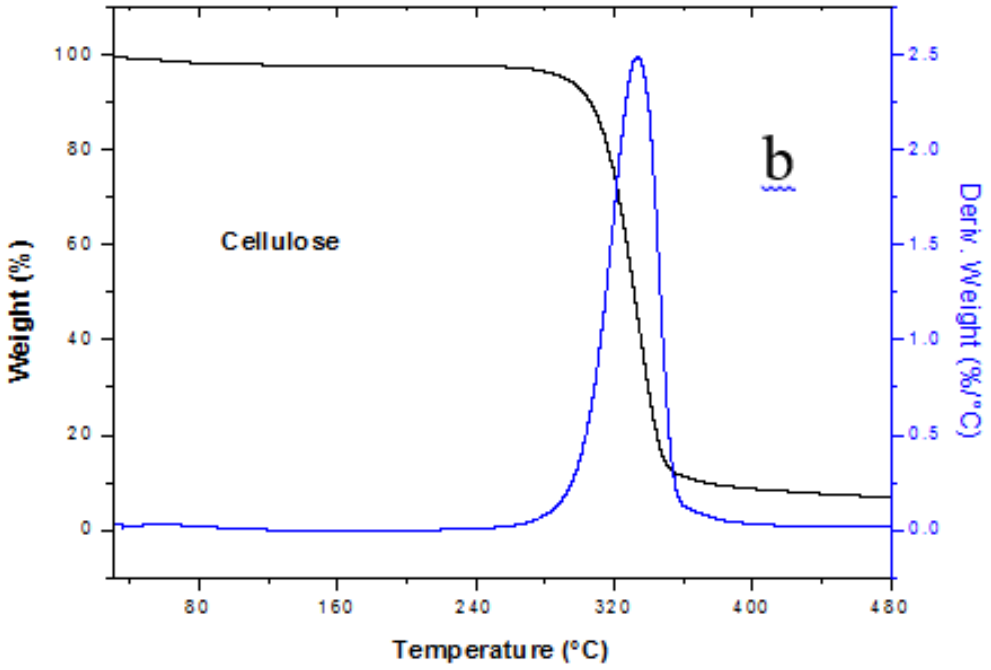
b
Cellulose
Weight (%)
Deriv. Weight (%/°C)
Temperature (°C)
100
80
60
40
20
0
2.5
2.0
1.5
1.0
0.5
0.0
80
160
240
320
400
480

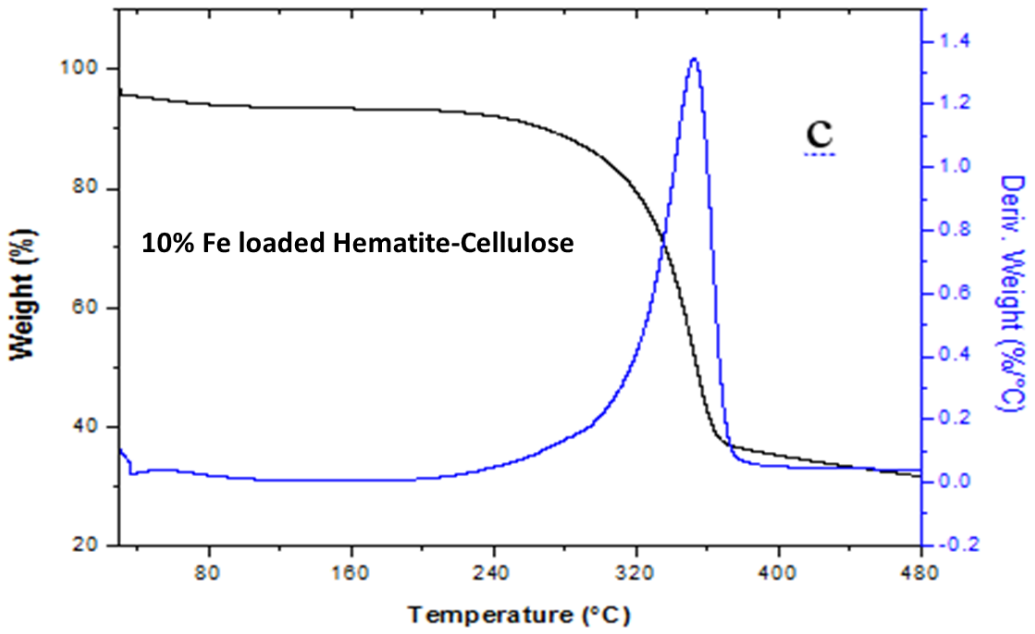

Figure 3.2 TGA results: (a) hematite, (b) cellulose, and (c) 10% Fe coated hematite-cellulose

3.2 FTIR Spectroscopy

3.2.1 FTIR for the goethite and goethite-cellulose composites

FTIR spectra were used to characterize the available functional groups which are formed between the goethite NPs and the cellulose support. In Figure 3.3 a, goethite spectra showed sharp IR bands at 798 and 892 cm^{-1} due to Fe-O-H bending vibration, where the 657 cm^{-1} band related to Fe-O stretching vibration of goethite [125]. The IR band at 468 cm^{-1} was assigned to an antisymmetric Fe-O-H stretching band of goethite [126], while the cellulose had bands for O-CH in-plane bending vibration (1423 cm^{-1}), COC, CCO and CCH deformation and stretching (895 cm^{-1}), C-OH *out-of-plane* bending at 662 cm^{-1} [33]. In Figure 3.3 b, goethite-cellulose composites with greater Fe content had a weaker band at 1423 cm^{-1}, indicating that O-CH from cellulose may interact with Fe. Greater Fe bonded with cellulose revealed reduced O-CH bending of cellulose, while a broad IR band (3327 cm^{-1}) related to the OH stretching of cellulose [33], and goethite had a stretching band at 3150 cm^{-1} [126]. Comparison of the goethite-cellulose composites indicated

spectral shifts occurred from 3327 to 3150 cm^{-1} with increasing Fe content. The results indicated that the OH groups of cellulose were involved in bonding with Fe of goethite, in agreement with the bands at 657, 798 and 892 cm^{-1} for the Fe-O-H bending vibrations and Fe-O stretching of goethite for composites with variable Fe content.

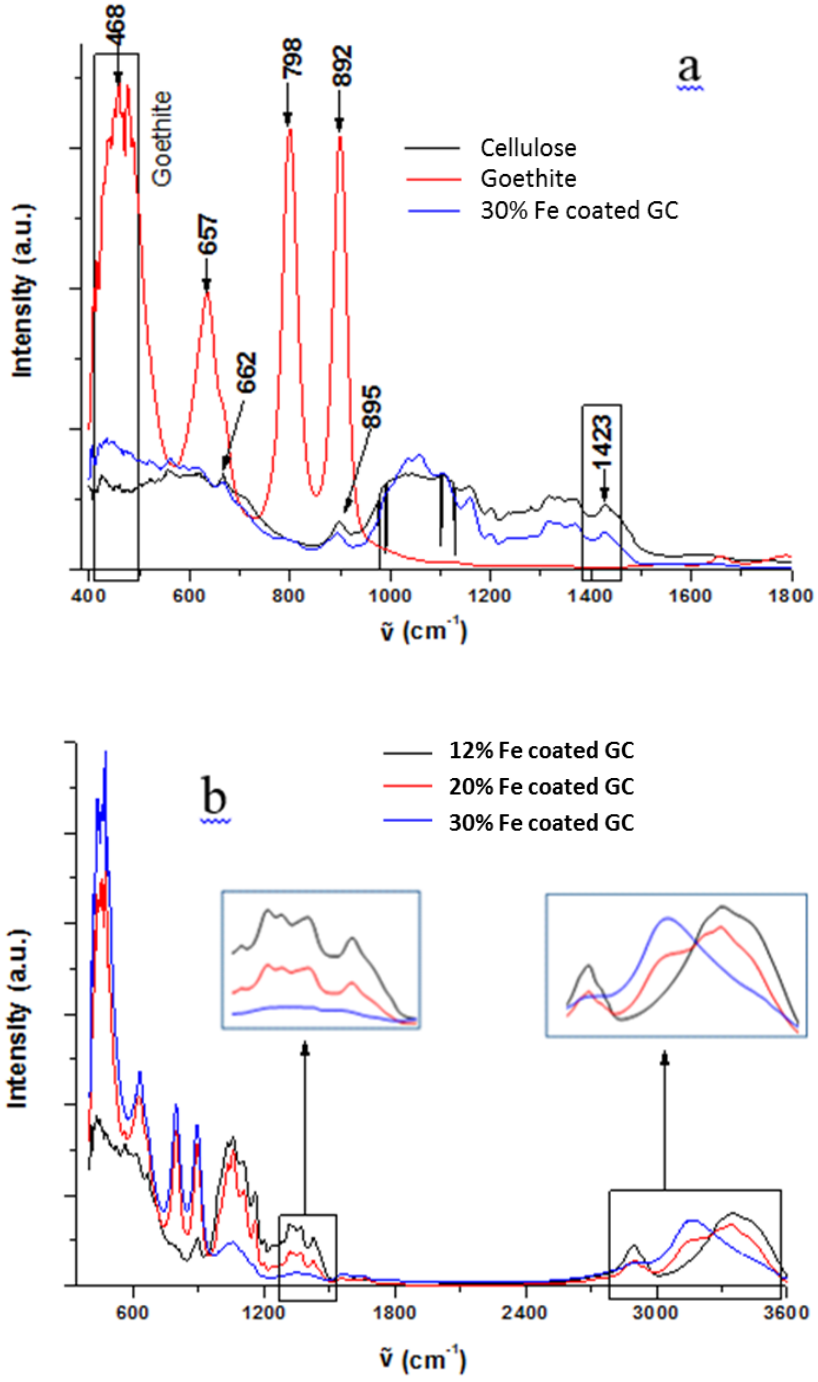

Figure 3.3 FTIR spectral results: (a) goethite, cellulose and GC materials, and (b) FTIR spectra of the GC materials with different Fe content 12.1%, 20.3% and 30.9%.

3.2.2 FTIR for the hematite and hematite-cellulose composites

FTIR spectra were obtained to evaluate the role of active functional groups that form bonds between the hematite NPs and the cellulose support materials. In Figure 3.4, hematite showed IR bands at 1392 cm^{-1} and 1572 cm^{-1} due to Fe-OH and Fe-O respectively [127]. The adsorption 3327 cm^{-1} can be attributed to structural OH. Cellulose showed bands for O-CH in-plane bending vibration 1423cm^{-1}, COC, CCO and CCH deformation and stretching 895cm^{-1}, C-OH *out-of-plane* bending at 662 cm^{-1} [33]. In Figure 3.4, hematite-cellulose composites with greater Fe content had a weaker band at 1423 cm^{-1}, indicating that O-CH from cellulose may interact with Fe. Also, greater Fe bonded with cellulose revealed reduced O-CH bending from cellulose. A broad IR band 3327 cm^{-1} related to the OH stretching of the cellulose and 2883 cm^{-1} related to C-H symmetrical stretching of the cellulose [33]. The results indicated that the OH groups of cellulose were involved in bonding with Fe groups of hematite, the more Fe loaded composites showed less OH signal in the IR spectra which was consistent with the goethite-cellulose composite.

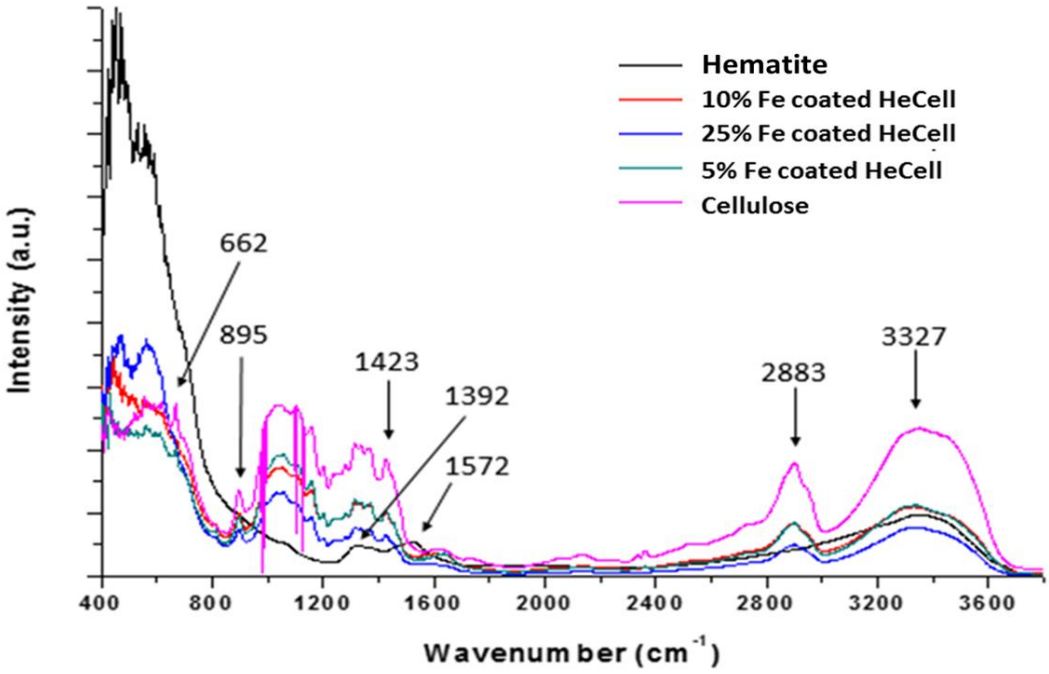

Figure 3.4 FTIR spectra of cellulose, hematite and HeCell materials with different Fe content 5%, 10% and 25%

Although GC and HeCell are different iron oxide-cellulose composites, the FTIR spectra shows information about the types of functional groups present. The similar functional groups from the two composites show similar IR spectra.

3.3 Raman Spectroscopy

3.3.1 Raman spectroscopy of the cellulose, goethite, and goethite-cellulose composites

The cellulose material used was derived from cotton linters, the Raman spectra of cellulose from 200 cm^{-1} to 2000 cm^{-1} showed broadening peaks due to the more amorphous cellulose than the highly crystalline cellulose [128]. The weak peaks at 352 cm^{-1} and 373 cm^{-1} were due to the CCC, COC, OCC, OCO skeletal bending, the methane bending CCH, COH and movement of CC, CO groups within the glucopyranosyl units; the weak peak at 896 cm^{-1} was from HCC, HCO bending; strong peaks at 1095 cm^{-1} and 1117 cm^{-1} were due to COC stretching symmetrically; the weak peak at 1337 cm^{-1} was from HCH (wagging), HCC, HOC, COH (rocking) bending; the weak peak at 1376 cm^{-1} was from HCH, HCC, HOC, COH bending; the weak peak at 1462 cm^{-1} was caused by HCH scissoring bending [128].

The Raman spectra of the synthetic goethite showed peaks at 223, 299, 400, 595, and 681 cm^{-1}. Raman bands occurring at 223 and 681 cm^{-1} were assigned to the Fe-O symmetric stretching; the 299 cm^{-1} peak was due to the Fe-OH symmetric bending; the 400 cm^{-1} peak was from the Fe-O-Fe symmetric stretching; and the 595 cm^{-1} peak was resulted from Fe-OH asymmetric stretching [129]. The synthetic goethite's Raman spectra from this work when compared with the goethite reported by Legodi and coworkers yielded results that were very similar. The similarities confirmed that the material synthesized in this work contained similar Fe-O, Fe-O-Fe characters as the goethite material [129].

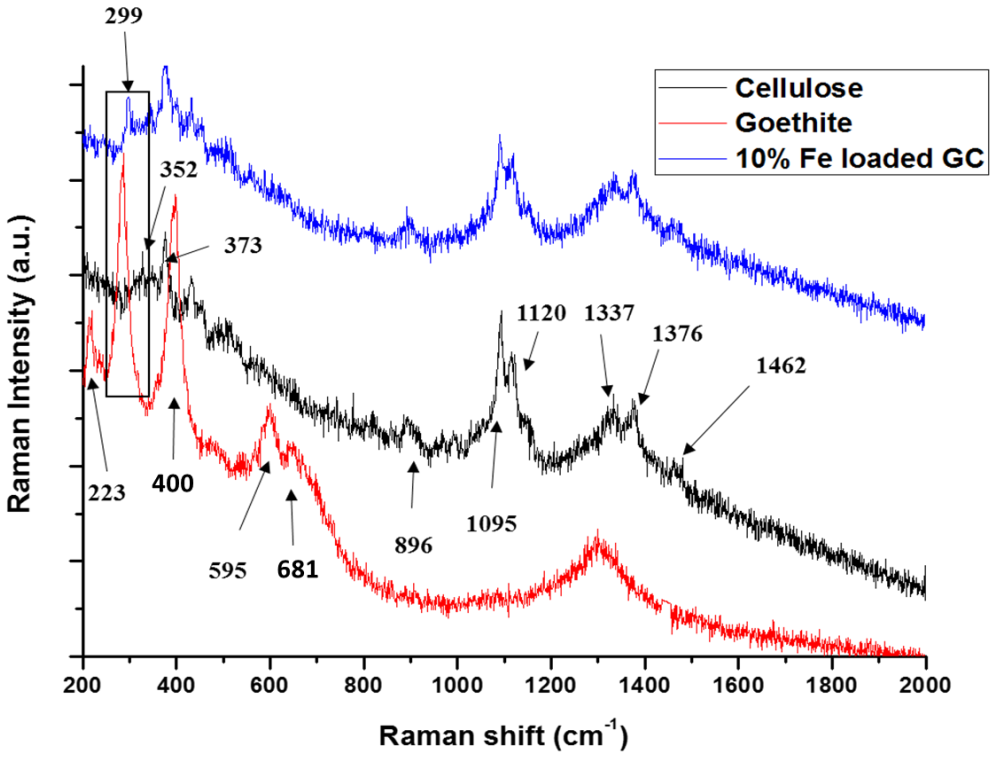

Figure 3.5 Raman spectra of cellulose, synthetic goethite, and the 10% Fe coated GC

The 10% Fe coated GC material's Raman spectra showed peaks at 299 cm^{-1} as a result of the Fe-OH symmetric bending and other peaks 352, 373, 896, 1095, 1120, 1337, 1376, and 1462 cm^{-1} that were similar to the cellulose's Raman spectra. Looking at all three Raman spectra of cotton linters cellulose, the synthetic goethite, and the 10% Fe coated GC, peaks 223, 595, and 681 cm^{-1} from goethite did not appear in the Raman spectra of 10% Fe coated GC. It could be that the intensity of these peaks was too weak to be detected. The other strong peak at 400 cm^{-1} from the goethite interfered with the 373 cm^{-1} peak from the cellulose, it also could not be detected in the Raman spectra of the 10% Fe coated GC. The strong peak 299 cm^{-1} was the only evidence that goethite NPs were presented with the cellulose to form the 10% Fe coated GC composite material.

3.3.2 Mode of adsorption between the ROX, goethite and goethite-cellulose composites

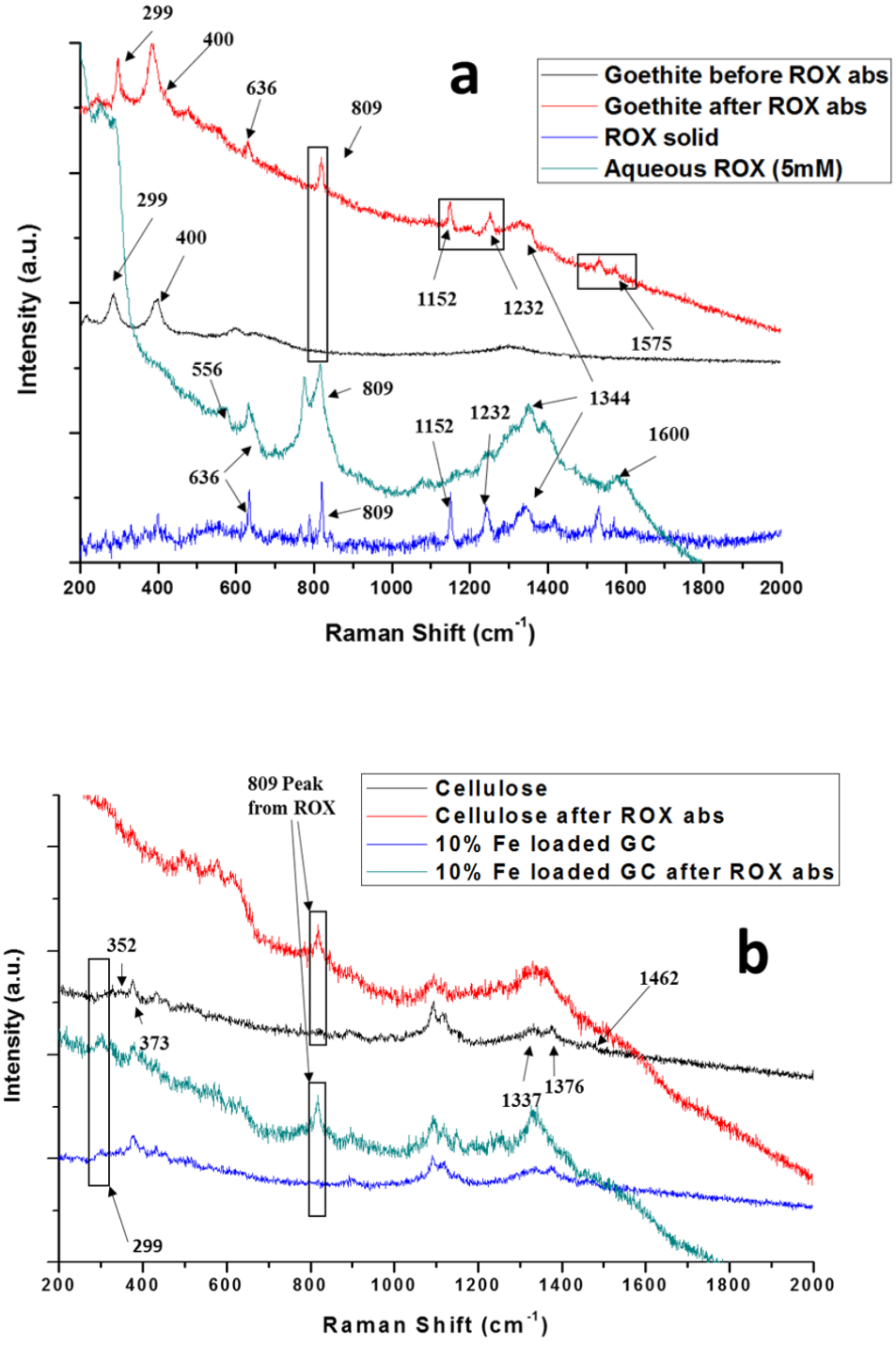

Figure 3.6 Raman spectra of the adsorbent materials before and after the roxarsone uptake, (a) Goethite, and (b) Cellulose and GC composites

Figure 3.6 a-b illustrated a comparison of the Raman spectra of the solid ROX, the aqueous 5 mM ROX, the adsorbent materials before and after uptake of roxarsone. The Raman spectra of solid roxarsone had a band at 636 cm^{-1} assigned to the As-C stretching, and the band at 809 cm^{-1} was due to AsOx stretching [130]. The bands at 1152 and 1232 cm^{-1} were due to CN and OH stretching [131]. Vibrational modes corresponding to the NO_2 group were also present in the Raman spectra at 1344 and 1600 cm^{-1}, corresponding to the symmetric and asymmetric modes [132]. The Raman spectra of the 5 mM ROX solution had similar peaks as the solid ROX, in addition to the solid ROX, it had a notable band at 556 cm^{-1} assigned to the As-OH out-of-plane bending [133]. The Raman spectra of the synthetic goethite was the same as previously described, peaks at 299 and 400 cm^{-1} were labeled for synthetic goethite for better comparison with the goethite Raman spectra after ROX sorption. Looking at both the goethite Raman spectra before and after roxarsone sorption, the Raman spectra of goethite after ROX sorption contained bands at 636, 809, 1152, 1232, 1344, and 1575 (1600) cm^{-1} which proved the ROX molecules were bonded with goethite nanoparticles. The Raman spectra of 5 mM aqueous ROX had two Raman bands at 1555 and 1600 cm^{-1}, corresponding to the aromatic ring and the nitro group asymmetric stretching. These two bands were overlapped at 1575 cm^{-1} from the effects of the As=O and $As(OH)O_2$ symmetric stretching [134].

Comparing the two Raman spectra of cellulose before and after roxarsone sorption, there was a noticeable band at 809 cm^{-1} from AsO_x stretching for cellulose after roxarsone sorption. This indicated that the roxarsone species were complexed with cellulose, where the weak bands at 1337, 1376 and 1462 cm^{-1} became weaker comparing with the Raman spectra of cellulose before sorption of roxarsone. Weaker band signals resulted for cellulose after adsorption of roxarsone because the incorporation of roxarsone onto the cellulose surface made the whole celluose structure appear more amorphous than before adsorption of roxarsone. For the Raman spectra of 10% Fe coated GC, it contained most of the bands of cellulose at 352, 373, 1095, 1120, 1337, 1376, and 1462 cm^{-1}; the bands at 299 and 400 cm^{-1} were due to the Fe-OH symmetric bending and the Fe-O-Fe symmetric stretching [95], the band at 299 cm^{-1} was more noticeable because of the large amount of Fe-OH groups presented in the goethite material. The present of Fe-O-Fe bond at 299 cm^{-1} was another evidence to show the goethite and cellulose composite material formed. Looking at both Raman spectra of 10% Fe coated GC before and after roxarsone sorption, the band at 809 cm^{-1}

from 10% Fe coated GC after roxarsone sorption showed that the roxarsone was complexed with the goethite-cellulose composite.

3.3.3 Mode of adsorption between the ROX, hematite and hematite-cellulose composites

The Raman results of the hematite and the hematite-cellulose composites are described in Figure 3.7, the bands at 299, 400, 495, 600 cm^{-1} and 1320 cm^{-1} in the synthetic hematite from this work were consistent with values recorded by other researchers [129, 135]. The results indicated that the hematite was successfully formed and the 1320 cm^{-1} peak was from nitrate due to insufficient washing of hematite [119]. The band at 299 cm^{-1} was more noticeable because of the large amount of Fe-OH from the water trapped within hematite during the synthesis [26]. The peaks at 400 and 600 cm^{-1} were due to Fe-O symmetric bending, the peak at 495 cm^{-1} was from the Fe-O symmetric stretching [129]. The Raman spectra of all the different Fe loaded hematite-cellulose composites showed peaks with cellulose features, peaks at 373, 896, 1095, 1120, 1337, 1376 and 1462 cm^{-1} all resulted from the cellulose. The weak peaks at 352 cm^{-1} and 373 cm^{-1} were due to the CCC, COC, OCC, OCO skeletal bending, the methane bending CCH, COH and movement of CC, CO groups within the pyranose ring units; the weak peak at 896 cm^{-1} was from HCC, HCO bending; strong peaks at 1095 cm^{-1} and 1120 cm^{-1} were due to COC stretching symmetric; the weak peak at 1337 cm^{-1} was from HCH (wagging), HCC, HOC, COH (rocking) bending; the weak peak at 1376 cm^{-1} was from HCH, HCC, HOC, COH bending; the weak peak at 1462 cm^{-1} was caused by HCH scissoring bending [128]. However, by comparing among 5%, 10% and 25% Fe coated HeCell composites, the peaks with cellulose features reduced gradually as Fe content increased. For instance, the peak around 896 cm^{-1} was from C-O-C bond in cellulose [136], this peak was more noticeable in the 5% Fe coated HeCell composite than the 10% Fe coated HeCell, and it became hard to notice in the 25% Fe coated HeCell composite.

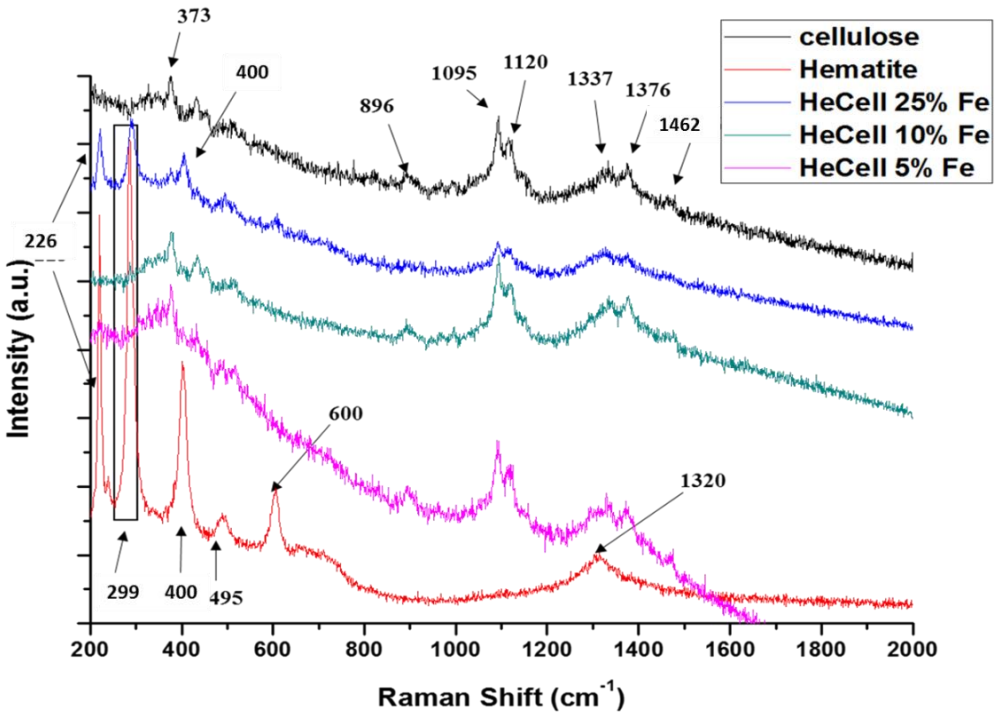

Figure 3.7 Raman spectra of hematite and composites with different Fe loading levels

For the 25% Fe coated HeCell, it had peaks from the hematite at 226, 299, 400, and 600 cm^{-1}, but the peak at 495 cm^{-1} was not observed in the 25% Fe coated HeCell which was due to the small size of the Fe-O symmetric stretching peak. For the 10% Fe coated HeCell composite, only one peak at 299 cm^{-1} with hematite feature was observed the remaining peaks all came from cellulose. As the Fe content decreased from 10% to 5% by weight, there were no peaks with hematite features observed in the 5% Fe coated HeCell composite. The reduced hematite features resulted from the small amount of hematite NPs available to scatter the laser in the Raman spectra instrument.

Figure 3.8 is the graph of the Raman spectra of the hematite and the 10% Fe coated HeCell composite before and after ROX adsorption. The Raman spectra of 5 mM ROX showed peaks at 636, 792, 809, 1232, 1344, and 1600 cm^{-1}. The Raman spectra of solid roxarsone had a band at 636 cm^{-1} assigned to the As-C stretching, and the bands at 792 and 809 cm^{-1} were due to AsOx stretching [130]. The bands at 1152 and 1232 cm^{-1} were due to CN and OH stretching [131].

Vibrational modes corresponding to the NO_2 group were also present in the Raman spectra at 1344 and 1600 cm^{-1}, corresponding to the symmetric and asymmetric modes [132].

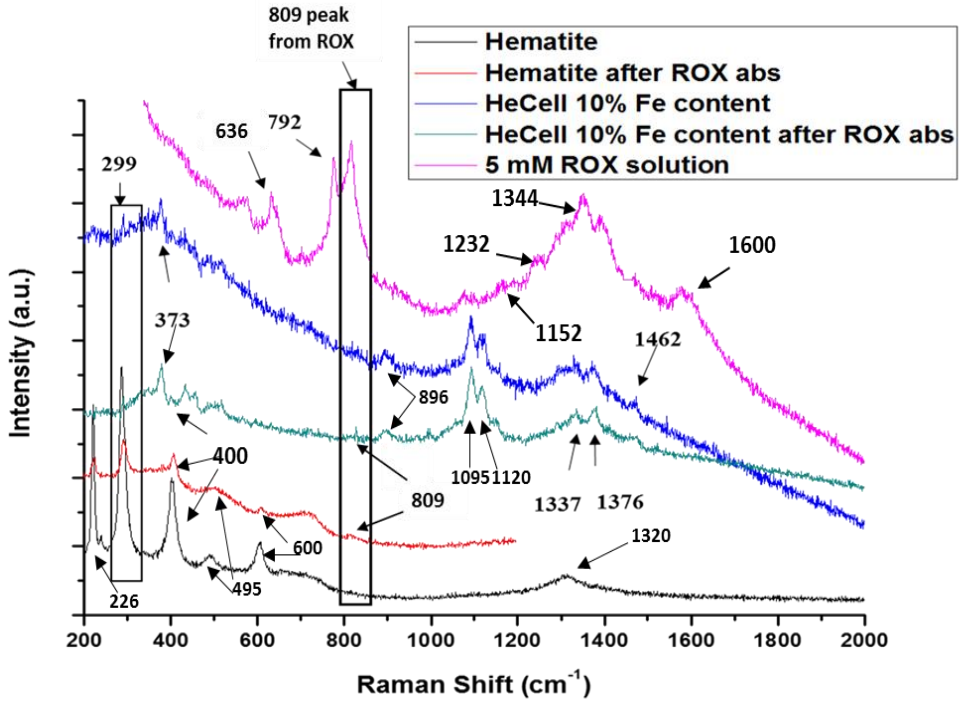

Figure 3.8 Raman spectra of the hematite and 10% Fe coated HeCell before and after uptake of roxarsone

The bands at 226, 299, 400, 495, and 600 cm^{-1} and 1320 cm^{-1} in the synthetic hematite from this work were consistent with values recorded by other researchers [129, 135]. It indicated that the hematite was successfully formed and the 1320 cm^{-1} peak was from nitrate due to insufficient washing of hematite [119]. The band at 299 cm^{-1} was the Fe-OH from the hematite during the synthesis [26]. The peaks at 400 and 600 cm^{-1} were due to Fe-O symmetric bending, the peak at 495 cm^{-1} was from the Fe-O symmetric stretching [129]. Comparison of the Raman spectra of the hematite before and after ROX sorption, the hematite after ROX sorption had an extra peak at 809 cm^{-1} from the ROX molecular. It provided evidence that the ROX adsorbed onto the hematite adsorbent. Furthermore, the Raman spectra of the hematite after ROX sorption showed reduced peaks intensity comparing with the hematite before ROX sorption. It indicated more amorphous structure in the short range after an uptake of ROX molecules by the hematite adsorbent;

it also provided evidence that the hematite can attract ROX molecules. Comparing the 10% Fe coated HeCell with the hematite's Raman spectra, the peaks at 299 and 400 cm^{-1} were showed in the 10% Fe coated HeCell composite which provided evidence that hematite NPs were coated with cellulose. Looking at the Raman spectra of the 10 % Fe coated HeCell before and after ROX sorption, the peak at 809 from ROX was shown in the 10% Fe coated HeCell composite after ROX sorption which indicated the ROX molecule bonded to the composite. Both Raman spectra from 10% Fe coated HeCell before and after ROX sorption, they had peaks at 373, 896, 1095, 1120, 1337, 1376 and 1462 which were all from the cellulose [128]; the broaden and reduced peaks were also observed for the 10% Fe coated HeCell after ROX sorption which indicated more amorphous structure in the short range after ROX sorption, it supported the assumption that the hematite cellulose composite can attract ROX molecules.

3.3.4 Hydration properties of adsorbent materials

Figure 3.9 shows the Raman spectra of ROX uptakes by the hematite in 5 % (Vol.) D_2O/H_2O system. To compare the peak intensity, baseline of these Raman spectra was first set and then the start and end point for each peak to integrate the peak area was set. The full width at half maximum (FWHM) for each peak was calculated and compared among each other. There was a trend of reduced D_2O peaks' area as the roxarsone concentration increased. This fluctuation indicated that the hydrogen bonded character of the solvent H_2O on the hematite adsorbent surface was affected by the adsorbate roxarsone concentration in the system [137]. The results suggest the possible adsorption mechanism of roxarsone onto adsorbents is a process of replace water molecules on the surface of adsorbents by roxarsone. At higher concentration of roxarsone, further replacement of water molecules occurs on the surface of adsorbents due to competitive binding of roxarsone on the adsorbent surface. Fewer water molecules on the surface of adsorbent will yield a weaker D_2O signal. Hence, the trend of reduced D_2O signals was observed with the increase of roxarsone concentration in solution.

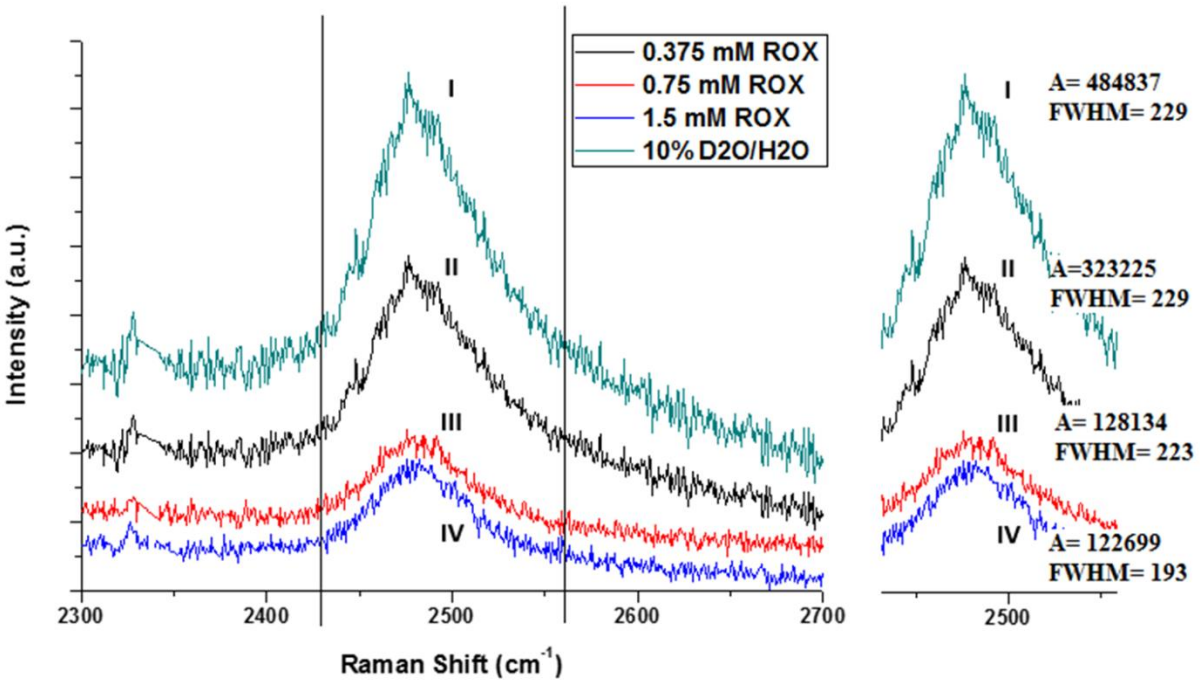

Figure 3.9 Raman spectra of ROX adsorption by hematite in 5% (Vol.) D_2O/H_2O solvent

3.4 TEM

3.4.1 TEM of the goethite and the 10% Fe coated goethite-cellulose composite

Figure 3.10 shows the TEM results for the synthetic goethite and the different Fe loaded goethite-cellulose composites. Figure 3.10 (a-b) are the TEM images of the synthetic goethite under 200 nm scale. These images show needle-shape of synthetic goethite NPs with sizes that range from 200 to 400 nm. The results are consistent with the results of other research confirming common shape of goethite crystals to be needle-like (acicular) [119]. Figure 3.10 (c-d) are the TEM images of the 10% Fe coated GC composite on 500 nm and 200 nm scales. Comparing with the pure goethite NPs, the composite material had reduced the appearance of needle-like features of the coated goethite NPs. The presence of cellulose as a support for goethite NPs reduced the long-range order via formation of a binary composite. Figure 3.10 (e-f) are the TEM images of 10% Fe coated GC composite under 100 and 50 nm scales, these images confirmed that the morphology

of goethite NPs changed to smaller needle shape after forming binary composite with the cellulose support material. These changes could be due to changes in precipitation conditions when forming the 10% Fe coated GC composite. According to Schwertmann's results, the length/width ratio of the needles varied widely, where the goethite crystals range from long, thin needles to short, broad blocks [119]. Figure 3.10 (g), (h), (I), and (j) display the TEM results of cellulose fibers under 500, 200, 100, 50 nm scales. Individual cellulose fibers were about 50 nm in width and the length is much higher, leading to a practically infinite aspect ratio of the cellulose fibers. Comparing Figure 3.10 (c-f) with Figure 3.10 (g-j), there were not many changes in the morphology of cellulose fibers after forming the 10% Fe coated GC composite material.

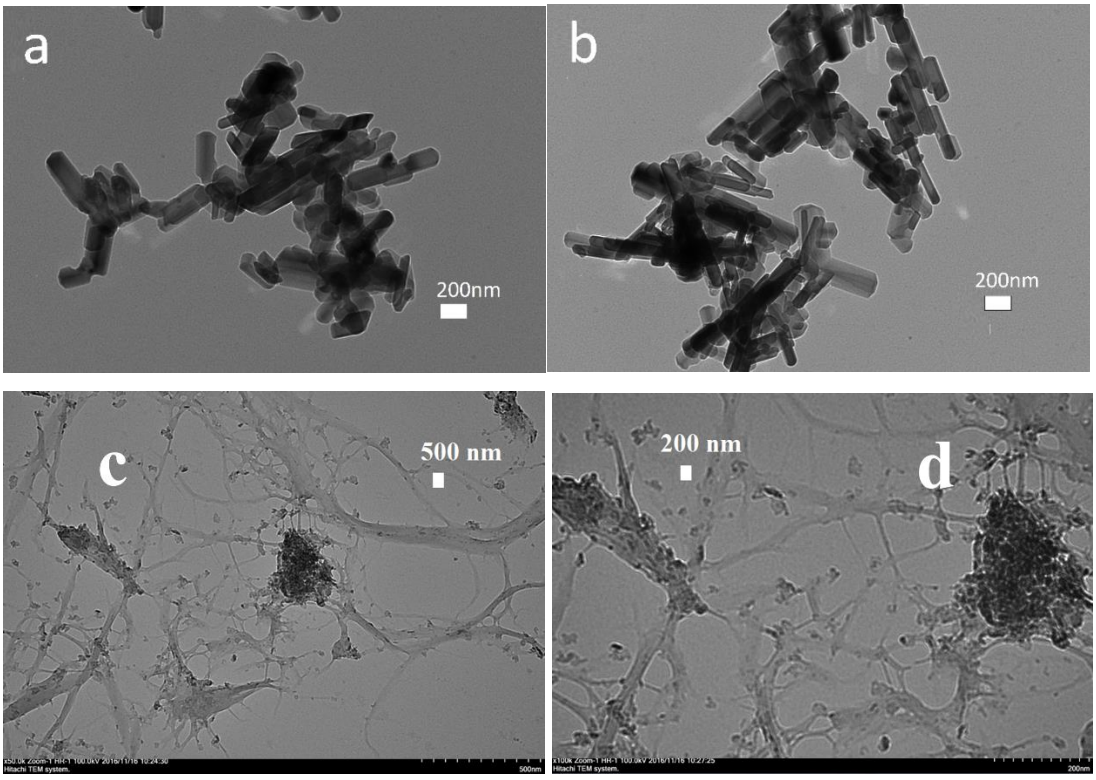

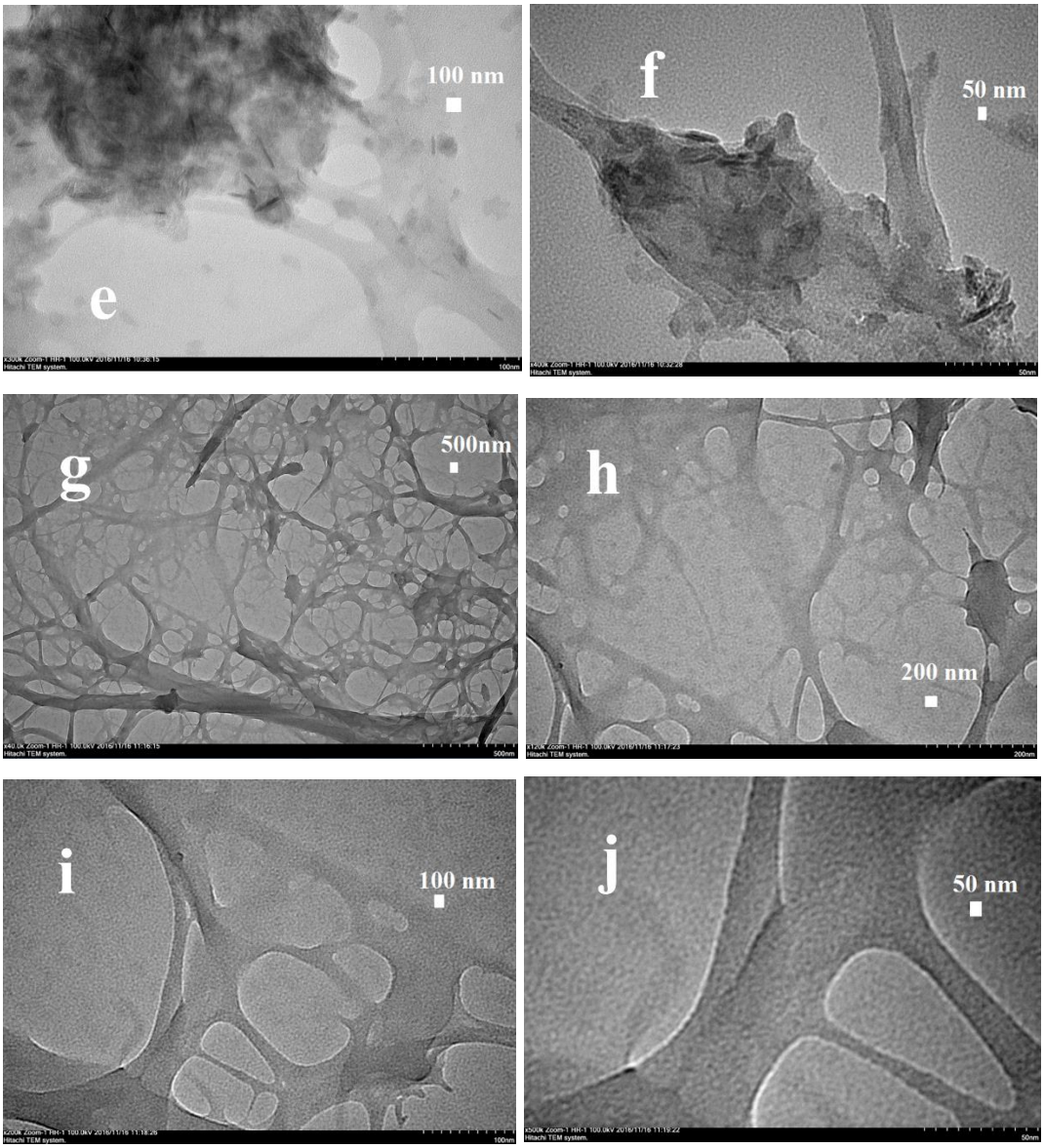

Figure 3.10 TEM of (a) and (b) goethite, (c), (d), (e), (f) goethite-cellulose under 500, 200, 100, 50 nm scale, (g), (h), (i), and (j) cellulose were obtained at 500, 200, 100, 50 nm scales.

3.4.2 TEM of the hematite and different Fe coated hematite-cellulose composites

Figure 3.11 (a) and (b) are TEM images of the hematite NPs synthesized from heating ferrihydrite NPs at 70 °C for 18 h. The synthesized hematite was irregular and diamond shaped with about 50-100 nm in diameter which was consistent with the hematite produced by

Schwertmann's method of transferring ferrihydrite NPs to hematite NPs [119]. Figure 3.11 (c), (d), and (e) were taken from the 10% Fe coated HeCell, these images show a fibril bundle of cellulose and an aggregate mass of hematite. Looking at Figure 3.11 (c), some spots on the cellulose fiber were covered with more hematite NPs than others. This indicated the coating of hematite NPs with the cellulose fiber support was not homogeneous. There were also some empty cellulose fiber spots which indicated some degrees of dispersion of hematite NPs on the cellulose fiber's surface. Figure 3.11 (f), (g), and (h) were taken from the 5% Fe coated HeCell composite, comparing Figure 3.11 (c) to (h) the greater aggregation of NPs occurred at higher concentration of hematite, lower Fe concentration would favor better coverage and dispersion of hematite NPs in the case of nanoparticle materials. Comparing Figure 3.10 (a) with Figure 3.11 (a), the rod shaped goethite NPs were larger in size than the hematite NPs which reduced their surface area resulting in less available sites for adsorption. Comparing Figure 3.10 (c) with Figure 3.11 (h), for the same amount of 10% Fe coated cellulose composite materials, the 10% Fe coated GC composite material showed bigger aggregated NPs cluster on the cellulose fiber surface than the 10% Fe coated HeCell material. Therefore, the smaller hematite NPs and low Fe loading resulted in better dispersion of these NPs onto the cellulose fiber surface.

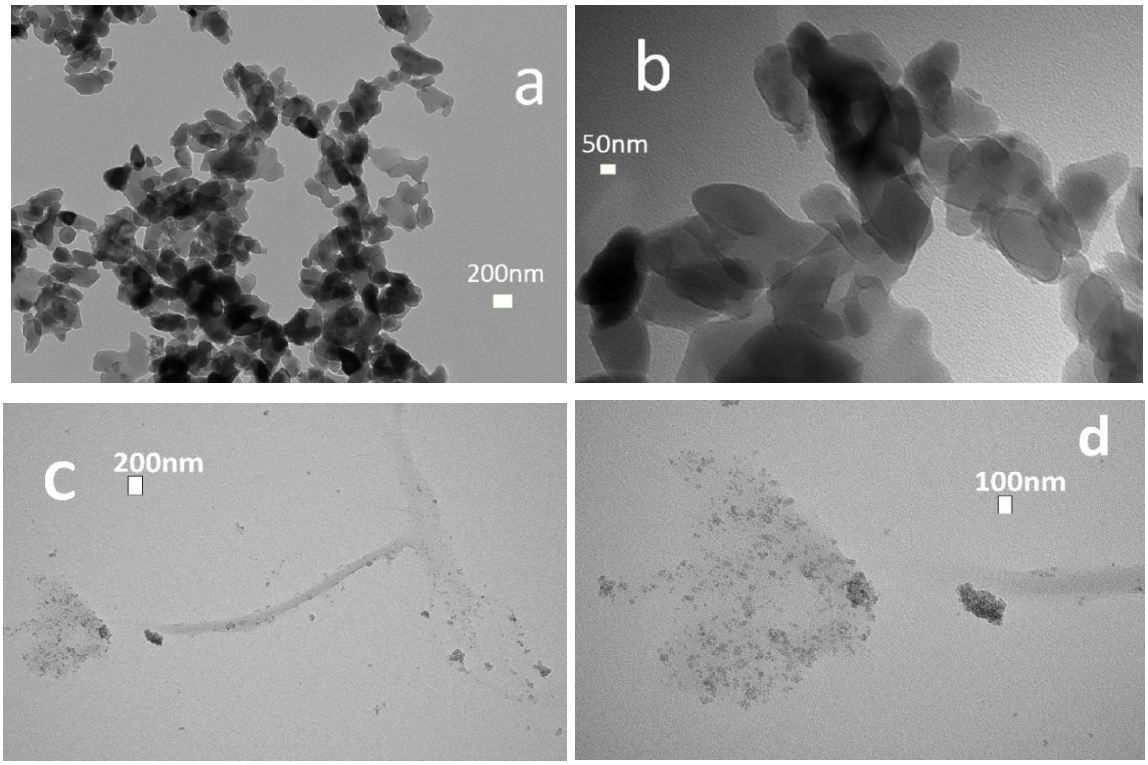

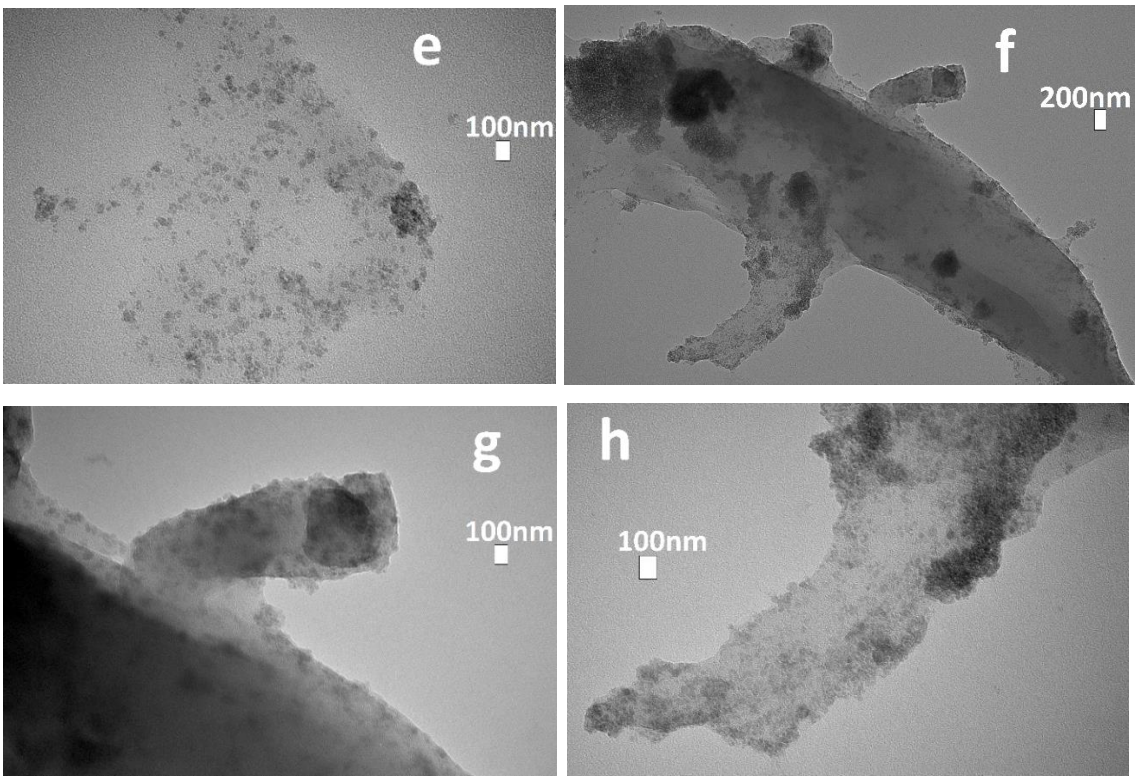

Figure 3.11 TEM of (a) and (b) hematite, (c) and (f) hematite-cellulose in 200 nm scale, (d), (e), (g), and (h) hematite-cellulose materials at 100 nm scale

3.4.3 TEM of the ferrihydrite NPs

Figure 3.12 (a) and (b) are TEM images of ferrihydrite NPs synthesized in work, these NPs were roughly round sphere shaped and aggregated together as big clusters. Comparing these images with literature results, the morphology of these ferrihydrite NPs was very similar and the diameter of ferrihydrite NPs was around 3-4 nm as shown in Figure 3.12 (c) and (d) [119]. The synthetic method for ferrihydrite NPs had been proven to be reliable and accurate and provided the basis for transferring to the hematite NPs by heating the ferrihydrite NPs.

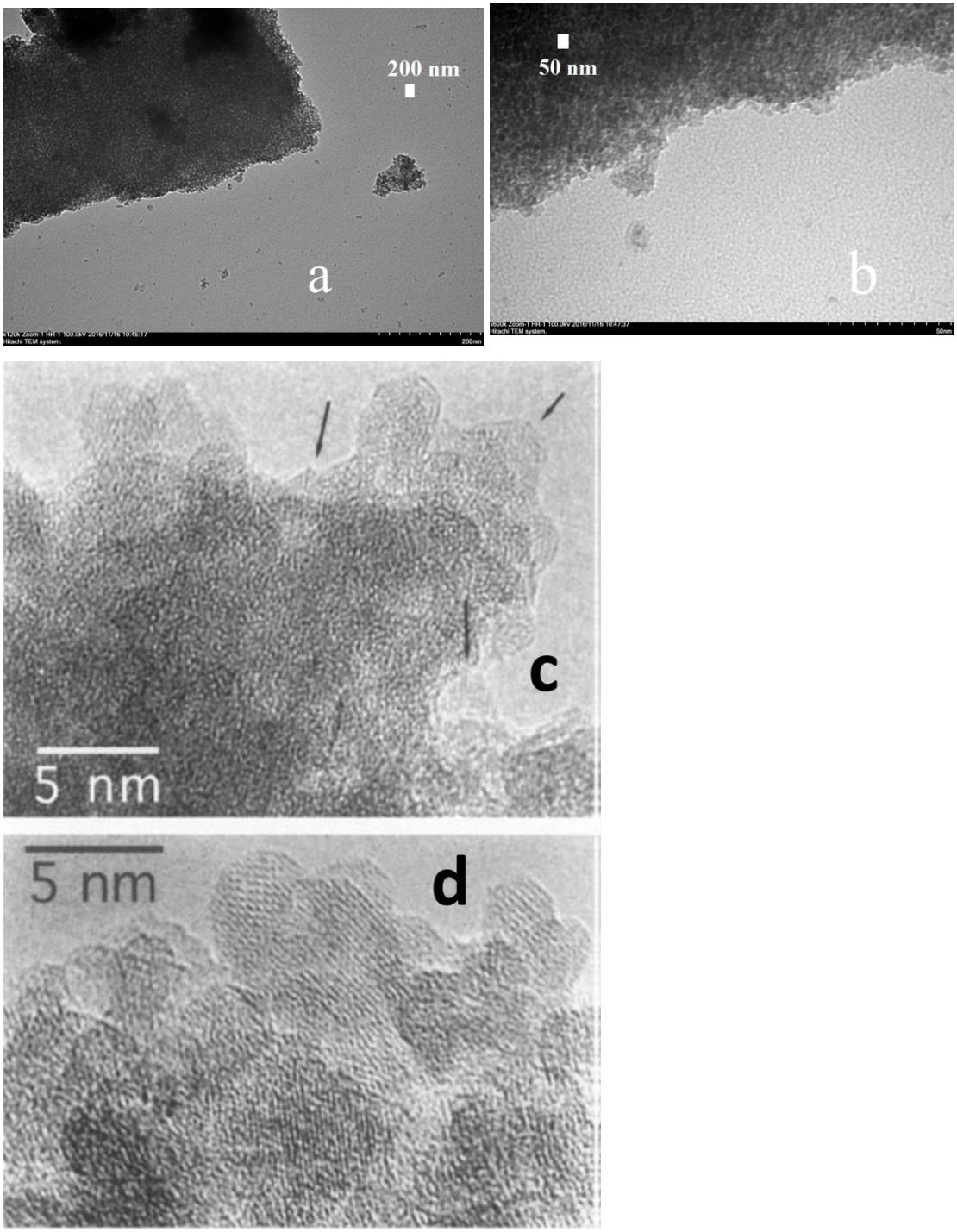

Figure 3.12 TEM of ferrihydrite NPs, (a) and (b) were synthesized in this study, (c) and (d) were from Schwertmann's work [119]

3.5 pXRD

3.5.1 pXRD for the cellulose, the goethite and different Fe coated goethite-cellulose composites

The synthetic goethite's pXRD spectra in Figure 3.13 showed characteristic strong peaks at 2θ of, ~25º, ~39º, ~43º, ~48º, ~63º, ~70º, and ~72º as well as weak peaks at ~21º, ~31º ~48º, ~59º, ~63º, ~64º, ~67º, , and ~75º. Due to the fix λ = 1.54 Å of the Cu K-alpha X-ray irradiation source, the 2θ reflection positions of synthesized goethite were slightly shifted from the Bragg's law calculation λ = 2dSinθ. Overall the synthesized goethite pXRD spectra was consistent with data from Das, Hendry and Essilfie-Dughan [138]; it was also consistent with data from Cornell and Schwertmann [119].

From the pXRD lines, it can be said that the goethite product was fairly crystalline and pure. The grain sizes of the synthetic goethite were calculated using the Scherrer relationship [139]. In Equation 3.1, τ was the grain size (nm), k was the Scherrer constant (0.94 for spherical crystals with cubic symmetry), λ was the wavelength (0.179 nm) of Co Kα, β was the full-width-half maximum (FWHM) of the highest intensity peak in radians, and cos θ was the angle (degree) value at the highest intensity peak in radians. The average grain size calculated for the synthetic goethite was 213 nm.

$$\tau = \frac{k \text{ X } \lambda}{\beta \text{ X } cos\theta} \qquad (3.1)$$

The cellulose's pXRD spectra in Figure 3.13 showed the 17° 2θ reflection assigned to the ($1\bar{1}0$) crystallographic plane, the 19° 2θ reflection assigned to the (110) crystallographic plane, the 23° 2θ reflection assigned to the amorphous phase and the 27° 2θ reflection assigned to the (200) crystallographic plane. The pXRD spectra obtained from this Sigma Aldrich cotton cellulose fiber was similar to the results of other researchers [124]. On the other hand, these (110) and (200) planes were named "hydrogen-bonded" plane. With the hydroxyl groups being equatorial to the cellulose ring plane, intra- and inter-chain hydrogen bonding was most prevalent within the (110) plane in the triclinic structure and within the (200) plane in the monoclinic structure. Inter-chain

hydrogen bonding within the other planes (010), (100) in the triclinic structure and the planes (110) and ($1\bar{1}0$) in the monoclinic structure was substantially lower, and van der Waals forces were considered the main forces between cellulose inter-chains [140].

The pXRD results for goethite coated cellulose composite materials displayed weaker and less intense peaks relative to the synthetic goethite NPs (Figure 3.13) in agreement with the reduction of long range order for the oxide phase as the cellulose content increases [141].

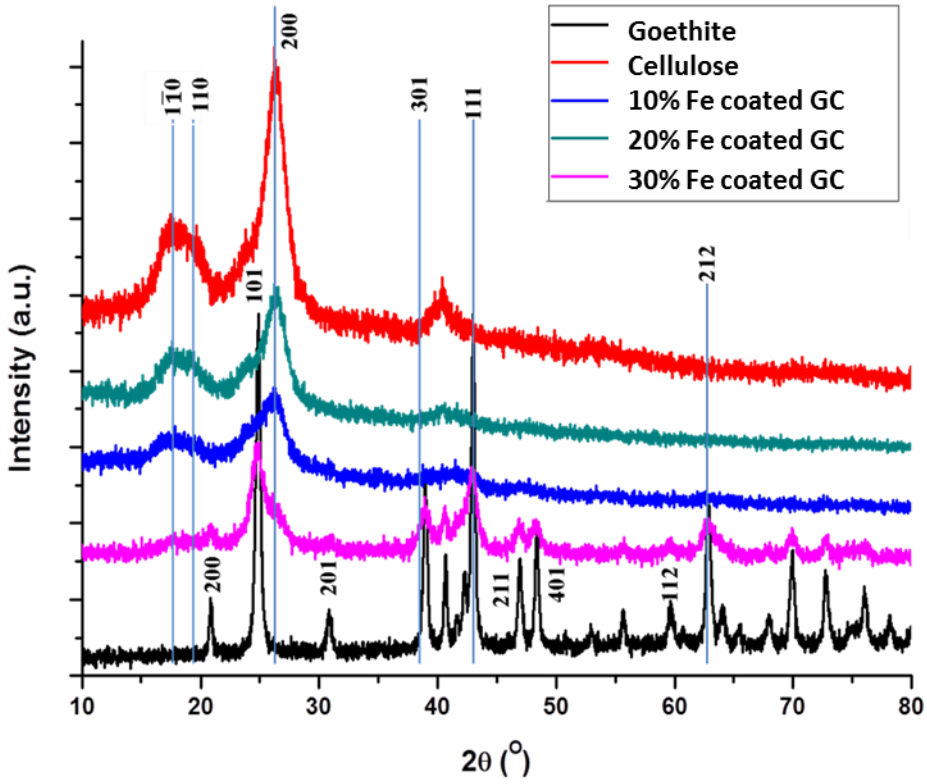

Figure 3.13 pXRD results for cellulose, goethite and goethite-cellulose composite materials

Comparing cellulose pXRD spectra with all different Fe loaded goethite-cellulose composites', the 10% and 20% Fe coated GC had no noticeable extra peaks with goethite NPs' feature. As the Fe content of GC grew from 20% to 30%, peaks with cellulose feature becoming weaker and wider; on the other hand peaks with goethite features became noticeable at 2θ of, ~25°,

~39º, ~43º, ~48º, ~63º, ~70º, and ~72º for those strong peaks. The 30% Fe coated GC composite retained both the amorphous cellulose feature at 23° 2θ reflection and the crystal goethite Bragg reflections.

3.5.2 pXRD for the ferrihydrite, the hematite and different Fe coated hematite-cellulose composites

In Figure 3.14, the pXRD results for ferrihydrite showed two major peaks which were evidence for 2-lines ferrihydrite [119]. The X-ray diffraction pattern of synthesized Fe_2O_3 had the diffraction peaks can be indexed well to a pure rhombohedral structure of α-Fe2O3 with lattice constants of a = 5.036 A˚, c = 13.749 A˚ (JCPDS No. 33-0664). The cellulose's pXRD spectra in Figure 3.14 showed the 17° 2θ reflection assigned to the $(1\bar{1}0)$ crystallographic plane, the 19° 2θ reflection assigned to the (110) crystallographic plane, the 23° 2θ reflection assigned to the amorphous phase and the 27° 2θ reflection assigned to the (200) crystallographic plane [124]. Comparing the amorphous phase region around 23° 2θ reflection for all three HeCell composites, pXRD patterns of different Fe coated HeCell composite materials showed broad peaks in the cellulose's amorphous region as more Fe loaded. The observation of reduced cellulose feature peaks from iron doping was in agreement with the reduction in long range order of the cellulose as more iron oxide NPs coated [141].

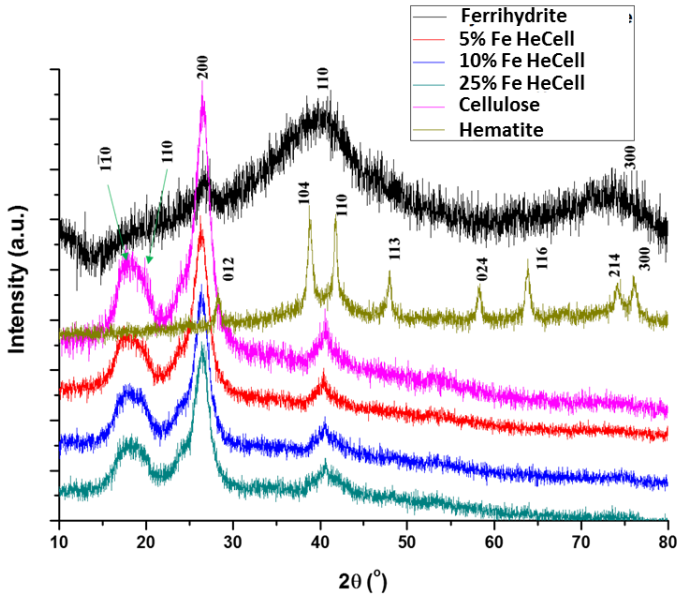

Figure 3.14 pXRD of ferrihydrite, hematite and different Fe coated HeCell composites

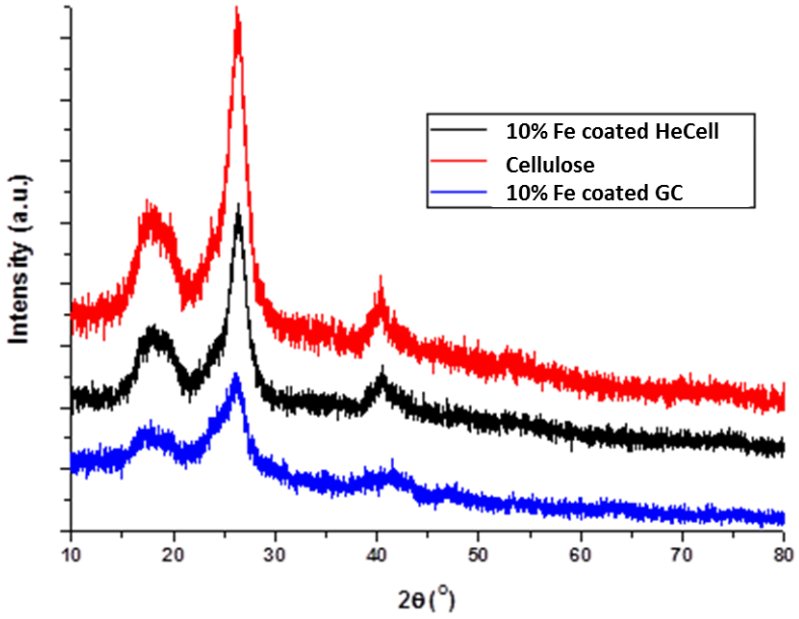

Figure 3.15 pXRD of cellulose, 10% Fe coated HeCell and 10% Fe coated GC

Comparing the three pXRD patterns, 2θ reflection peaks at 17°, 19° and 27° were broadened when coating cellulose with iron. The cellulose's amorphous phase region around 23°

also increased as more iron was coated with the cellulose. Comparing between the same amounts of iron coated cellulose composites the 10% Fe coated HeCell and the 10% Fe coated GC, the pXRD pattern showed the cellulose feature was more reduced for the 10% Fe coated GC. This was due to the goethite NPs being more crystalline and with more defined crystal structure than hematite; also the grain size of the goethite NPs was larger than hematite NPs. Hence, the coating of hematite NPs onto the cellulose had less effect on the long range crystal structure than coating with goethite NPs with the cellulose.

3.6 BET

3.6.1 Goethite and different Fe coated goethite-cellulose composites

N_2 adsorption–desorption analysis (BET) of the specific surface areas of goethite showed surface area 57 m^2/g. The nitrogen adsorption isotherm of goethite NPs showed type IV of the IUPAC adsorption isotherm classification which exhibited a hysteresis loop. The type IV adsorption isotherm with H3 type hysteresis loop indicated goethite NPs were mesoporous adsorbents. At low pressure, an adsorbent monolayer was first formed on the adsorbent pore surface. The broad H3 type hysteresis loop indicated the thin slit-like capillary pores of the goethite NPs [142]. From the experimental results in Figure 3.17, the nitrogen adsorption isotherms of the different Fe loaded GC composites were also type IV adsorption isotherm with H3 type hysteresis loops. These BET results indicated nitrogen gas adsorption and desorption processes of GC composites were similar to the goethite NPs. The goethite NPs coated with the cellulose fiber must contribute the most in the nitrogen sorption process of the composite materials, because the 30% Fe coated GC composite had the largest nitrogen gas adsorption capacity. Results recorded in Table 3.1 showed that the 10% Fe coated GC composite had the smallest 8 m^2/g among all the composites, the BET specific surface area increased with the Fe content for the composites. Hence, the uptake of nitrogen gas was mainly affected by the surface area of the goethite NPs on the composite materials.

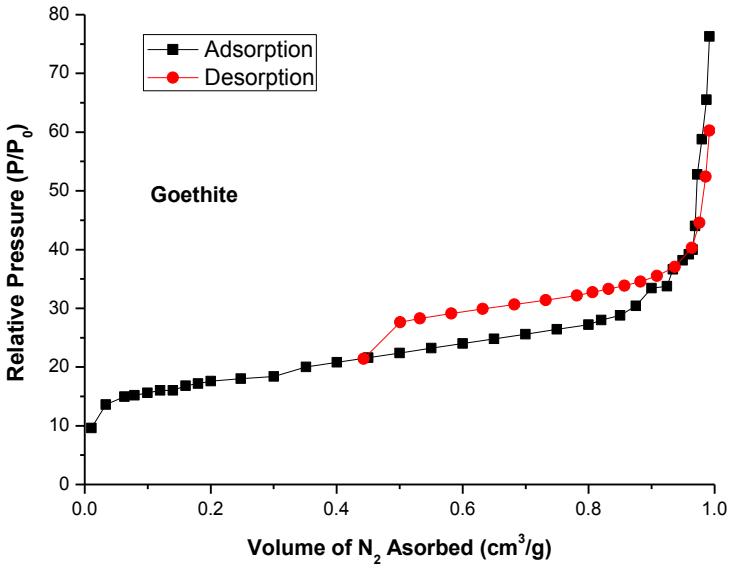

Figure 3.16 Goethite sorption/desorption profile with nitrogen at 77 K

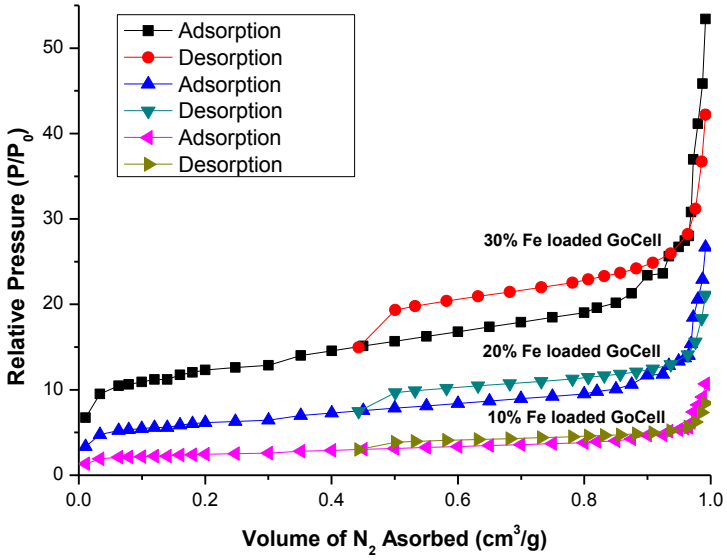

Figure 3.17 10% Fe coated GC composite sorption/desorption profile at 77 K

Table 3.1 Total specific surface area of the goethite NPs and the 10% Fe coated GC

Adsorbent	BET specific surface area (S_{BET}, m^2/g)
Goethite	52
10% Fe coated GC	8
20% Fe coated GC	20
30% Fe coated GC	38

3.6.2 Ferrihydrite

The BET specific surface area result for ferrihydrite was 282 m^2/g. The smaller size and more amorphous structure of ferrihydrite NPs showed more surface area than goethite NPs. The isotherms presented a hysteresis loop which indicated the presence of mesoporosity for the ferrihydrite NPs [142]. The hysteresis loop for ferrihydrite was H2 type which indicated the constricted porous networks or ink-bottle pores in the ferrihydrite NPs [143]. For adsorption curve of the H2 type hysteresis loop, the capillary force adsorbed the nitrogen gas and condensation happened within the pores as the external pressure increased. As the external pressure corresponding to the upper closure point of the hysteresis loop, the pores were completely filled with liquid. On the other hand, in the desorption process one major mechanism may be associated with the H2 type desorption process: cavitation. When the external pressure dropped, the liquid trapped inside the pores reached the limit of stability and "boiled" to form gas bubbles in the pore interior [143].

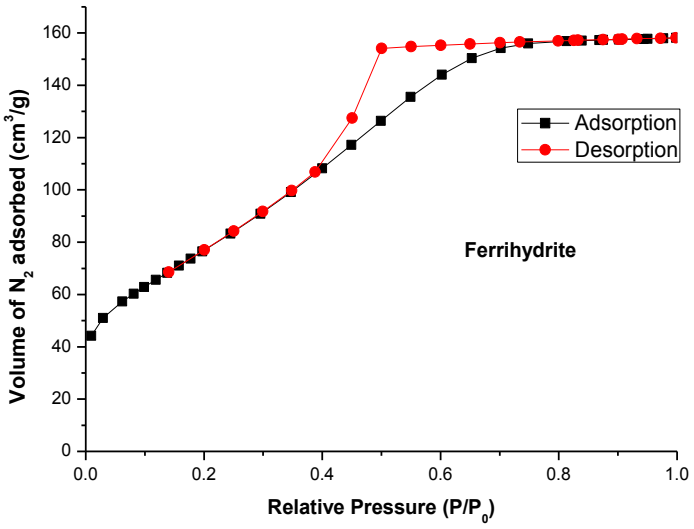

Figure 3.18 Ferrihydrite sorption/desorption profile with nitrogen at 77 K

Table 3.2 Total specific surface area of ferrihydrite from BET analysis

Adsorbent	BET specific surface area (S_{BET}, m^2/g)
Ferrihydrite	282

3.6.3 Hematite and different Fe coated hematite-cellulose composites

The N_2 gas adsorption isotherms of the hematite and its cellulose composites at 77 K belong to type IV isotherm which also indicated the mesoporous pore size of these adsorbent and multiple layers of adsorbate can form on the adsorbent surface. These isotherms N_2 gas adsorption isotherms of the hematite presented an H3-type hysteresis loop feature, which was related to the presence of slit-like pores in the hematite NPs [144]. All of these hematite and HeCell composites must possess/contain macropores because their isotherms showed continuous uptake of nitrogen gas when the relative pressure was close to unity.

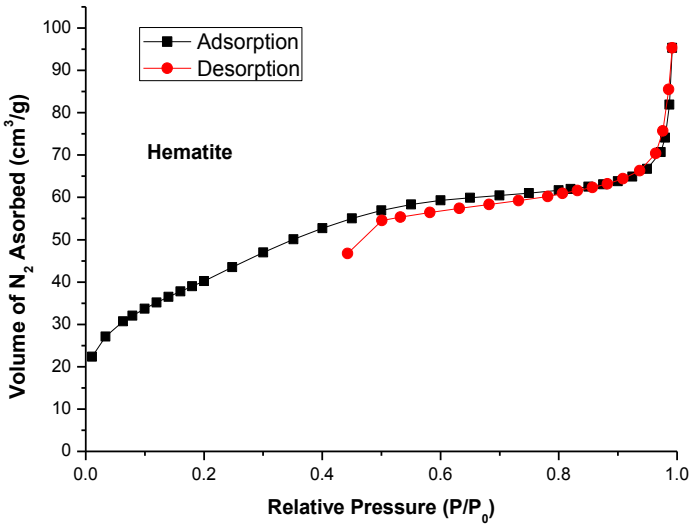

Figure 3.19 Hematite nitrogen sorption/desorption profile at 77 K

The BET equation was used to calculate the specific surface areas of each adsorbent. The methodology adopted by Barrett et al. was used to estimate the mesopore volumes and pore size distributions [53] [145]. The results for the hematite and its composites were listed in Table 3.3. Comparing the specific surface area of the synthesized hematite and different Fe coated HeCell composites, it became evident that the hematite had the largest specific area of 105 m^2/g, and the smallest BET specific area was the 5% Fe coated HeCell with 10 m^2/g. The observed trend was that the more hematite NPs coated onto the cellulose, the larger the surface area of the composite materials became. The surface area of the composite increased with the Fe content indicated the hematite NPs had more influence on the surface area of the composite materials which was reasonable due to the small surface area of the cellulose fibers. On the other hand, the TEM results of 5% and 10% Fe HeCell showed coating of Fe NPs on the cellulose surface was not homogeneous which concord with the BET results of 5% and 10% Fe HeCell that the surface area of 10% Fe HeCell was not two times larger than the surface area of 5% Fe HeCell.

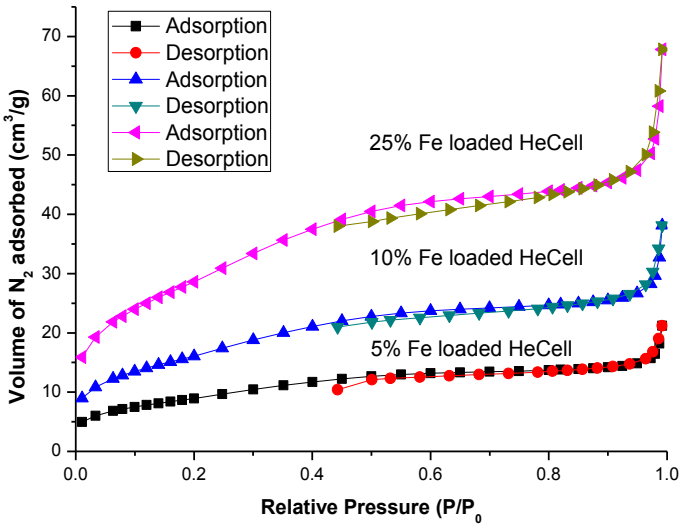

Figure 3.20 10% Fe coated HeCell nitrogen sorption/desorption profile at 77 K

Table 3.3 The BET specific surface area for the hematite and different Fe coated HeCell composites

Adsorbent	BET specific surface area (S_{BET}, m^2/g)
Hematite	105
5% Fe coated HeCell	10
10% Fe coated HeCell	18
25% Fe coated HeCell	32

3.7 Solid State ^{13}C NMR Spectroscopy

3.7.1 Goethite and different Fe coated goethite-cellulose composites

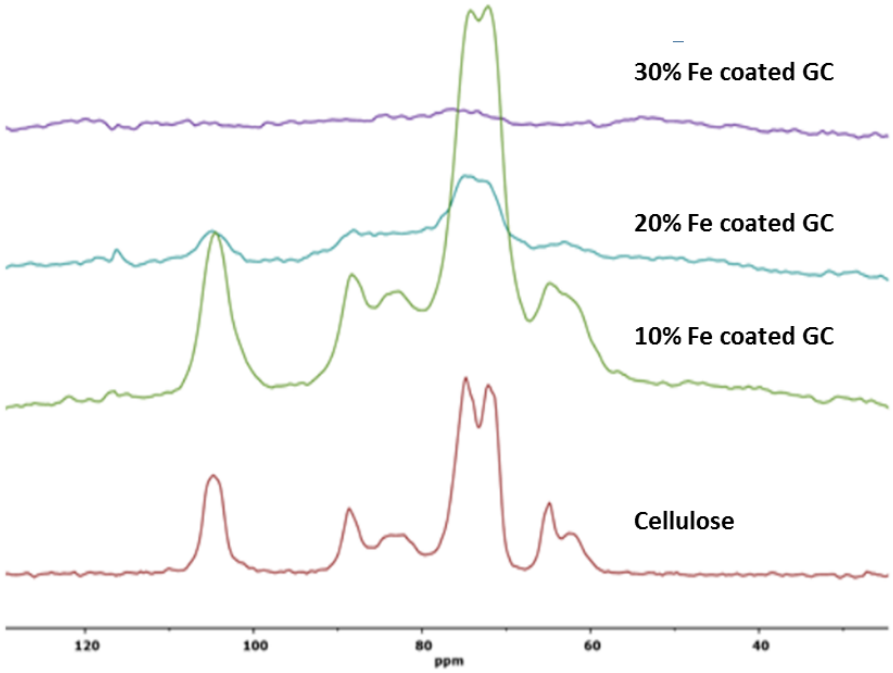

Figure 3.21 ^{13}C CP-MAS solids NMR (ssNMR) spectra of Goethite and different Fe coated GC composites

The trend of the ssNMR results showed the more iron coated with the composites, the cellulose ^{13}C NMR features were less pronounced. The 30% Fe coated GC had very little cellulose spectral features and indicated the composite material's structure became more rigid which reduced the ^{13}C resonance signal, thereby resulting in weaker ^{13}C spectral lines.

3.7.2 Hematite and different Fe coated hematite-cellulose composites

Figure 3.22 showed the ^{13}C solid NMR spectra of native cellulose and HeCell composites. Native cellulose had the following ^{13}C NMR resonance lines: C1 (105 ppm), C2/C3/C5 (68–78 ppm), C4 (88.4 and 83.3 ppm), and C6 (57–67 ppm), in agreement with a previous report [146].

Comparing the solid states NMR patterns of cellulose and different Fe coated HeCell composites, weaker ^{13}C peaks, band broadening and chemical shift variations were observed in more Fe coated HeCell composites. As more Fe coated on the cellulose fiber, the composite material's structure became more rigid which reduced the ^{13}C resonance signal which resulted weaker ^{13}C peaks. For the 25% Fe coated HeCell composite, the cellulose's C-2,3,4,5 carbon proton coupling signals all reduced which indicated the high level Fe coating effects of carbon proton coupling inside the cellulose molecules.

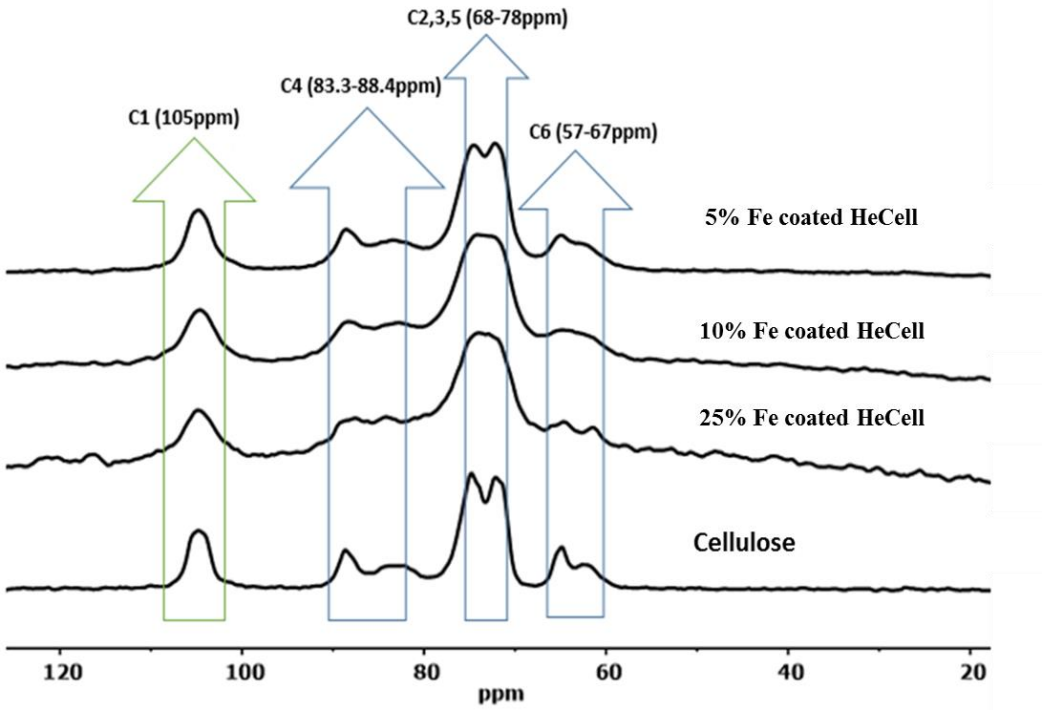

Figure 3.22 ^{13}C CP-MAS solids NMR spectra of the hematite and HeCell composites

3.8 Iron Coating Efficiency

3.8.1 Goethite and different Fe coated goethite-cellulose composites

The results of Fe coating efficiency of different Fe coated GC composites are listed in the Table 3.4. The reduced levels of Fe used for the loading results in greater Fe coating efficiency achieved. This can be understood since the cellulose material had limited surface sites for binding

Fe NPs and low concentration of Fe NPs generally led to more efficiently dispersed NPs onto the cellulose fiber surface and improving the Fe coating efficiency.

Table 3.4 Fe coating efficiency of GC composite adsorbent materials with variable Fe content

Adsorbent	Fe content (w/w %)	Fe coating efficiency (%)
10% Fe coated GC	10.1	85
20% Fe coated GC	20.3	80
30% Fe coated GC	30.9	71

3.8.2 Hematite and different Fe coated hematite-cellulose composites

The results of Fe coating efficiency of different Fe coated HeCell composites are listed in the Table 3.5. The less Fe used for loading the more Fe coating efficiency was achieved, because the cellulose material had limited surface sites for binding hematite NPs and low concentration of hematite NPs disperse better on the cellulose fiber surface which also helped to increase the Fe coating efficiency. The higher Fe coating efficiency, the less of Fe NPs will be wasted during the synthesis process. Synthesis of iron oxide NPs coated onto cellulose led to composite materials with high Fe coating efficiency. This method is a cost effective way of making these composite materials and also reduces chemicals needed to precipitate uncoated Fe NPs in the wastewater.

Table 3.5 Fe coating efficiency of HeCell composite adsorbent materials with variable Fe content

Adsorbent	Fe content (w/w %)	Fe coating efficiency (%)
5% Fe loaded HeCell	4.34	86.8
10% Fe loaded HeCell	8.47	84.7
25% Fe loaded HeCell	19.7	78.6

CHAPTER 4 : RESULTS AND DISCUSSION: CELLULOSE, GOETHITE, AND GOETHITE-CELLULOSE MATERIALS' SORPTION OF ROXARSONE

4.1 Roxarsone Adsorption Isotherms

4.1.1 pH effects on the sorption of ROX

At pH 4, ROX was ionized and singly charged, whereas the dianion species were favored at pH 7. By contrast, goethite adopted a positive surface charge below pH 9 [24]. According to Table 4.1 (b), the GC composite material had a positive zeta-potential from pH 4 to 7. The low pH environment favored ROX uptakes, because the positively charged iron oxide NPs can attract negatively charged ROX molecules and single charged ROX molecule will likely to occupy one binding site from the iron oxide NPs' surface. When pH reached neutral the uptake of ROX decreased, because the dominate dianion species of ROX molecules had to occupy two binding sites on iron oxide NPs' surface. The more binding sites of the iron oxide NPs needed for attract the dianion ROX species resulted lower uptake of ROX in the neutral pH environment. Once the pH went above 9, the surface charge of iron oxide NPs became negative which will not attract the same negatively charged ROX molecules. The adsorption results were consistent with the Raman results above, since goethite and the composite material contained Fe-OH_2 groups which can interact with roxarsone anions. The positively charged surface Fe-OH_2 groups interacted with roxarsone to form complexes which included other heteroatom sites of the adsorbate such as Fe-O-As and Fe-O-N.

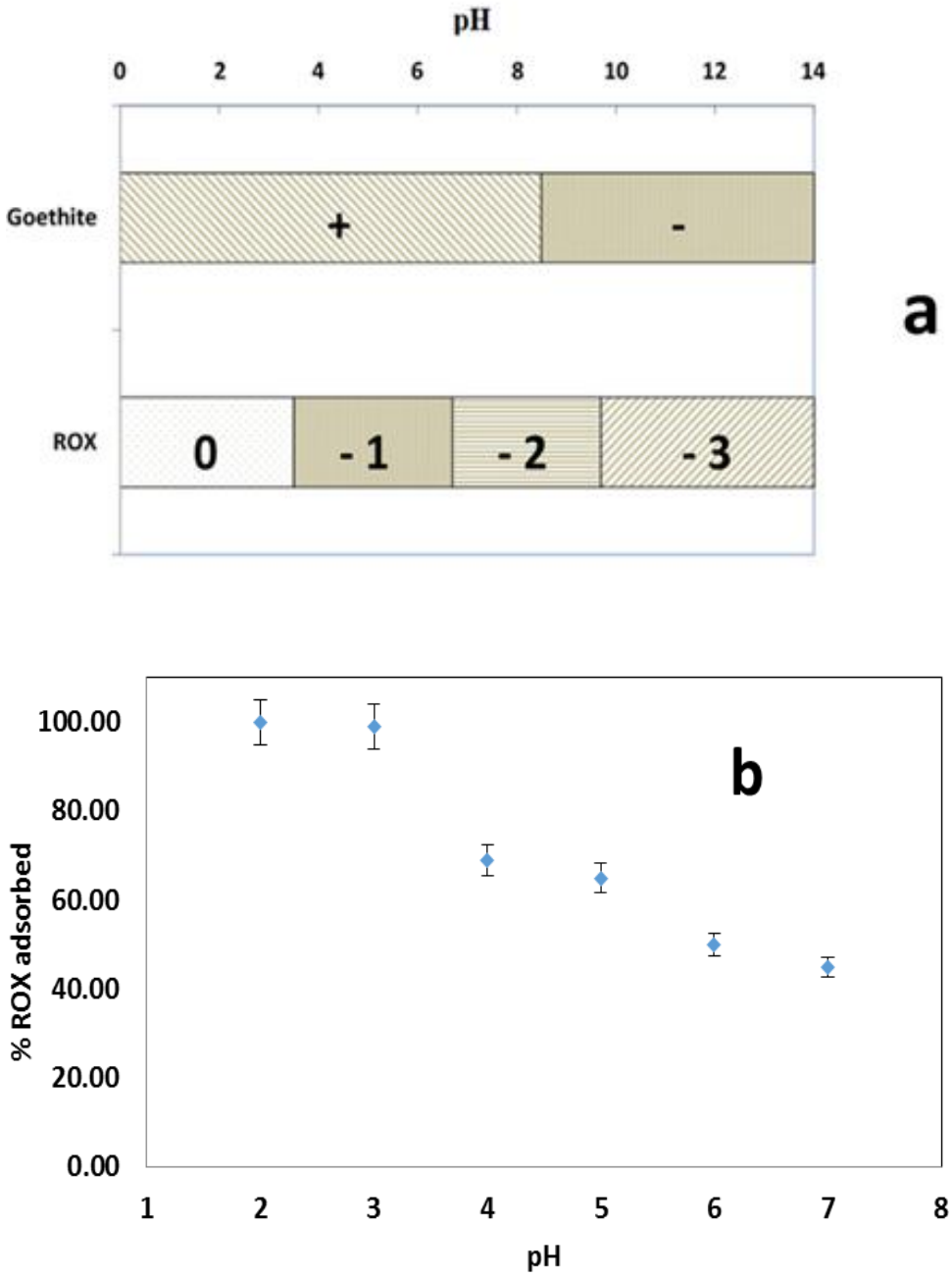

Figure 4.1 (a) Schematic of dominant charge states for ROX (roxarsone) and goethite at variable pH conditions. (b) The pH effect of the roxarsone equilibrium uptake by a 10% Fe coated GC composite with a roxarsone solution (0.040 mM) using an adsorbent dosage at 0.2 g/L.

According to Figure 4.1 b, the uptake of ROX at lower pH was greater than elevated pH conditions for the GC material. The isotherm uptake results suggested that the uptake depended on the presence of available of binding sites of goethite NPs. At lower pH conditions, the surface charge of the GC composite was protonated ($-OH_2^+$) where such groups served as ligand exchange sites for roxarsone anions [22]. At pH > 9, roxarsone molecules underwent further ionization where less adsorbate was bound to the adsorbent. At pH values above the pH_{pzc}, the reduced adsorption of roxarsone related to a reduced positive charge on the adsorbent surface. Above pH 9, the surface charge of the adsorbent was reduced and the adsorbate had a reduced adsorption affinity due to electrostatic repulsions between the bound ROX anion species. Ionization of the –OH groups of goethite contributed negative surface charge ($-O^-$) which led to charge repulsion between the adsorbent surface and the ROX anion species.

Greater ROX uptake was observed for the GC material below pH 7 (Figure 4.1 b), in agreement with the trend for increasing ROX uptake with decreasing pH. The trend in pH coincided with the pH_{pzc} value of goethite (pH_{pzc}=8.6) in Figure 4.1 a [22]. The goethite-based iron oxide had a negative surface charge where electrostatic repulsions occurred with anionic adsorbates due to the accumulation of OH^- ions on the adsorbent surface when the pH lie above the pH_{pzc} of the adsorbent. By contrast, the adsorbent surface was positively charged when the pH lie below the pH_{pzc}, and favored the adsorption of roxarsone anions due to favorable electrostatic interactions. The fact that GC materials adsorbed roxarsone more efficiently at pH values below 7.0 compared with higher pH values revealed the role of the surface potential of the adsorbent, in accordance with the trends in zeta-potential and uptake of roxarsone anion species. At pH>6, the relative amount of ROX dianion species bound to the adsorbent was lower compared with lower pH conditions (pH<6). Roxarsone dianion species may occupy multiple binding sites on the adsorbent surface, as compared with singly charged ROX anions that occupy a single binding site. For the same adsorbent, the amount of roxarsone dianions were lower than the singly charged anion species at pH <6, in accordance with the speciation of ROX (Scheme 1.1)

4.1.2 Different Fe coated composites effect on the sorption of ROX

4.1.2.1 Various Fe content goethite-cellulose composites

The iron coating efficiency was studied by comparing supported materials with variable amounts of iron loading from the synthesis and the final product. Each of the composite materials was evaluated for roxarsone uptake using batch experiments where ca. 37.5 mg of adsorbent in 1.5 mM roxarsone solution (7 mL) at pH 7 was equilibrated for 18 h. The roxarsone uptake results for different Fe coated GC composites were compared, where composite materials with greater iron content had greater roxarsone uptake, as shown in Table 4.1. The composites with higher Fe content showed increased roxarsone uptake, it was evidenced that ROX molecules must bond with iron oxide NPs. The uptakes of roxarsone from cellulose fibers of the composite adsorbent would also contribute in the adsorption process, the uptakes from cellulose were much lower comparing with goethite.

Table 4.1 Roxarsone adsorption values by GC composite adsorbent materials with variable Fe content

Adsorbent	Fe content (w/w %)	Roxarsone uptake (mmol/g)
10% Fe coated GC	10.1	0.0222
20% Fe coated GC	20.3	0.0446
30% Fe coated GC	30.9	0.0661

4.1.2.2 Various Fe coated hematite-cellulose composites

The iron coating efficiency was studied by comparing supported materials with variable amounts of iron loading from the synthesis and the final product. Each of the composite materials was evaluated for roxarsone uptake using batch experiments where ca. 37.5 mg of adsorbent in 1.5 mM roxarsone solution (7 mL) at pH 7 was equilibrated for 18 h. The roxarsone uptake results for different Fe coated HeCell composites were compared, where composite materials with greater iron content had greater roxarsone uptake, as shown in Table 4.2. There was a correlation between

the Fe content and the ROX uptake by the iron oxide-cellulose composites, it was evidenced that ROX molecules must bond with iron oxide NPs.

Table 4.2 Roxarsone adsorption values by HeCell materials with variable Fe content

Adsorbent	Fe content (w/w %)	Fe coating efficiency (%)	Roxarsone uptake (mmol/g)
5% Fe coated HeCell	4.34	86.8	0.0509
10% Fe coated HeCell	8.47	84.7	0.0873
25% Fe coated HeCell	19.7	78.6	0.101

4.1.3 Adsorption isotherm models for the goethite and goethite-cellulose composites

Adsorption isotherms revealed uptake properties of an adsorbate between solution and adsorbent phase at equilibrium conditions. In order to understand the sorption capacity and affinity of the roxarsone with various sorbent materials, a suitable isotherm model was required to describe the adsorption behavior. Figure 4.2 (a-b) illustrated the equilibrium uptake isotherms for the goethite, GC composites, and cellulose with roxarsone at pH 7. In all cases the uptake (Q_e) increased in a nonlinear fashion with increasing C_e (see Equation 1.1). Among the various sorbents, cellulose showed the lowest uptake of ROX (ca. 0.0284 mmol/g) over the range of concentrations. By comparison, 30% Fe coated GC showed greater uptake (ca. 0.0661 mmol/g), while goethite displayed the highest uptake overall (ca. 0.073 mmol/g). The monolayer uptake (Q_m) capacity paralleled the trend in slope of the Q_e vs. C_e curves at low concentration. The isotherm results indicated that goethite had greater uptake over cellulose, while the 30% Fe coated GC composite was intermediate. Thus, the active adsorption sites in the composite material were attributed to the goethite domains; whereas, cellulose accounts for approximately 10% of the roxarsone uptake overall. The best-fit lines through the data for the pure materials (goethite and cellulose) were well described by the Langmuir model, in accordance with homogeneous adsorption sites of these

materials. By contrast, the best-fit results for the GC composites were well-described by the Freundlich model (see Equation 1.2), in accordance with the presence of heterogeneous adsorption sites due to the cellulose and goethite domains. The corresponding best-fit parameters are listed in Table 4.3.

Table 4.3 Isotherm adsorption parameters for the roxarsone onto the cellulose, the goethite, and GC composite materials at 295 K

Adsorbent	T (K)	Langmuir			Freundlich		
		Q_m (mmol/g)	K_L (L/mmol)	SSE	K_F	n	SSE
Cellulose	295	0.0284	0.289	3.69E-7	0.00629	1.23	4.96E-7
Goethite	295	0.0730	11.5	6.46E-6	0.0710	3.49	1.47E-4
30% Fe coated GC	295	0.0661	4.53	8.35E-6	0.0553	3.30	3.90E-6
20% Fe coated GC	295	0.0446	4.27	3.80E-6	0.0369	3.17	5.88E-7
10% Fe coated GC	295	0.0222	4.40	7.27E-7	0.0184	3.24	8.08E-8

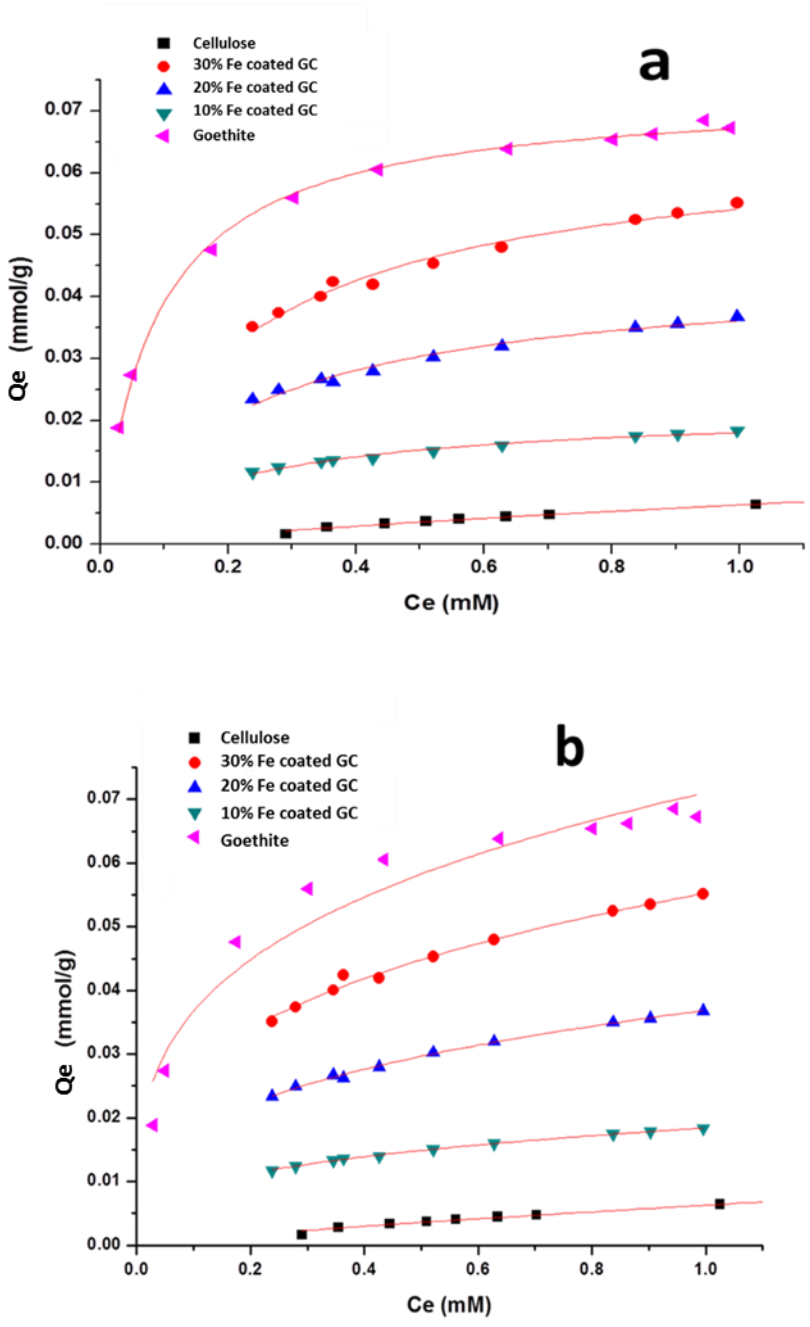

Figure 4.2 Adsorption isotherms and "best fit" results for roxarsone with various adsorbent materials (Goethite, GC, and Cellulose) at 295 K (a) Langmuir isotherm and (b) Freundlich isotherm model

4.1.4 Adsorption isotherm models for the hematite and HeCell composites

Adsorption isotherms showed the partitioning of adsorbate between solution and adsorbent phase at equilibrium conditions. In order to understand the sorption capacity and affinity of roxarsone with various sorbent materials, a suitable isotherm model was required to describe the behavior. Figure 4.3 (a-b) shows adsorption isotherm of the roxarsone with the hematite and the HeCell composite materials. The profile of the adsorption isotherm showed a good correspondence with the Freundlich isotherm, suggesting that the uptake occurs at heterogeneous sites on the HeCell adsorbents' surface [52].

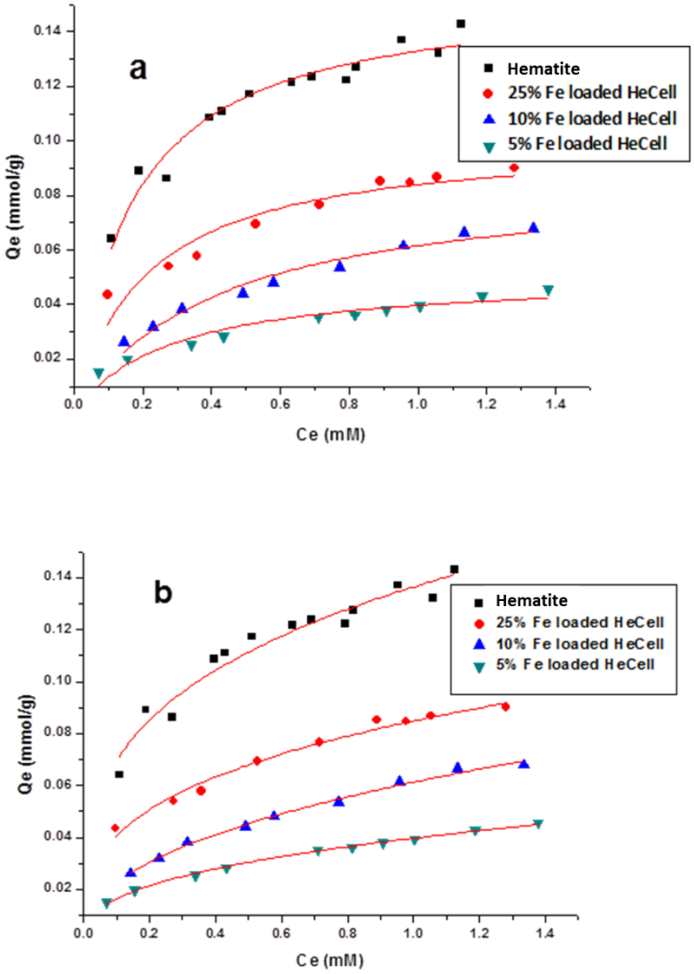

Figure 4.3 Adsorption isotherm of roxarsone with various adsorbent materials at 295 K. (a) Langmuir model fit of the hematite and HeCell composites, and (b) Freundlich model fitting of the hematite and HeCell composites.

The isotherm parameters are listed in Table 4.4 according to the best-fit results. The monolayer adsorption capacity (Q_m) of roxarsone with hematite was 0.155 mmol/g and the HeCell (10% Fe) composite was ca. 0.0873 mmol/g (Q_m was calculated by Eqn 1.1). By comparison, the Q_m value for cellulose was very low which indicated that hematite may serve as the principal adsorption site for roxarsone.

Table 4.4 Isotherm adsorption parameters for the roxarsone onto the hematite and the HeCell composite materials at 295 K.

Adsorbent	T (K)	Langmuir			Freundlich		
		Q_m (mmol/g)	K_L (L/mmol)	SSE	K_F	1/n	SSE
Hematite	298	0.155	5.90	2.71E-4	0.136	0.293	2.77E-4
5% Fe loaded HeCell	298	0.0509	3.54	5.90E-5	0.0397	0.384	4.04E-5
10% Fe loaded HeCell	298	0.0873	2.39	5.06E-5	0.0613	0.434	1.03E-5
25% Fe loaded HeCell	298	0.101	4.84	2.13E-4	0.0848	0.319	3.33E-6

4.2 Roxarsone Adsorption Kinetics by the "filter barrier" method

4.2.1 Adsorption kinetics models for the goethite and goethite-cellulose composites

Kinetic uptake isotherms provided information on the dynamic adsorption parameters for various systems. The kinetic parameters for ROX uptake (q_e, mmol/g; see Eqn 1.9 and 1.10) with the various sorbent materials are shown in Figure 4.4 (a and b) and Table 4.5. A comparison of the

pseudo-first-order (PFO) and the pseudo-second-order (PSO) kinetic models for the adsorption process revealed that the PSO model provided a better fit, according to the SSE values in

Table 4.5. During an initial period of the adsorption profile, the uptake displayed by the adsorbents was described by the PFO model. Over a longer time interval, the PSO kinetic model provided a better fit of the adsorption profile, the values of the correlation coefficients are all extremely high (>0.998) where similar trends were reported elsewhere [147].

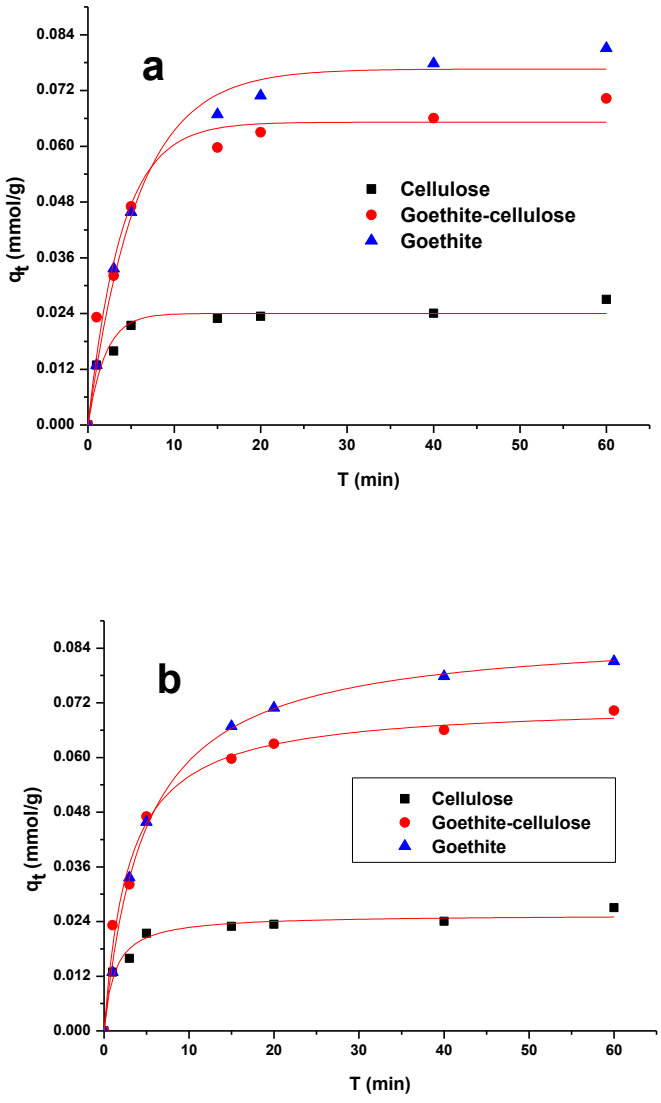

Figure 4.4 Kinetic uptake experiments for the cellulose, the goethite, and the 30% Fe loaded GC, as described by two kinetic models: (a) PFO, and (b) PSO models.

The PFO model assumed a single type of binding site [148]; whereas, the PSO model assumed that multi-adsorption sites exist. The GC materials may bind with roxarsone at multiple sites due to the presence of different surface functional groups in such composite materials. The greater rate of adsorption for roxarsone onto cellulose revealed that the kinetics of binding between cellulose and roxarsone was favoured and may relate to the labile hydration character of the polysaccharide surface due to its dipolar and the rapid diffusion process with such anion species [149]. By contrast, the adsorption process for ROX with goethite or GC composites was reduced at lower pH values for goethite-based materials. The similar rates of adsorption for goethite and its composites related to the goethite binding sites and the reduced lability of the hydration sphere, especially below the pH_{PZC}, where surface bound water had reduced lability due to ion-dipole interactions at the sorbent surface. This kinetic barrier concurred with the greater Lewis acid character of the goethite relative to the cellulose, and provided further evidence that goethite was supported onto the cellulose.

Table 4.5 Adsorption kinetics experiment parameters from the PFO and PSO models for uptake of roxarsone onto the cellulose, the goethite and the 30% Fe coated GC adsorbents at 295 K

Adsorbent	C_0 (mM)	PFO Model			PSO Model		
		k_1 (min^{-1})	$Q_{e,cal}$ (mmol/g)	SSE	k_2 (g/mmol min)	$Q_{e,cal}$ (mmol/g)	SSE
Cellulose	0.194	0.498	0.0240	3.04E-5	31.8	0.0255	1.33E-5
Goethite	0.194	0.176	0.0767	5.80E-5	2.36	0.0878	6.74E-6
Goethite-Cellulose (30.9% Fe loading)	0.194	0.261	0.0652	1.26E-4	4.85	0.0719	4.87E-5

4.2.2 Adsorption kinetics models for the hematite and hematite-cellulose composites

Kinetic uptake experiments provided information on the adsorption parameters for various systems. The kinetic parameters for the uptake of roxarsone (q_e; mmol/g, see Eqn 1.9 and 1.10) with various sorbent materials are shown in Figure 4.5 (a-b) and Table 4.6. The pseudo-first-order (PFO) and the pseudo-second-order (PSO) kinetic models were used to describe the adsorption process.

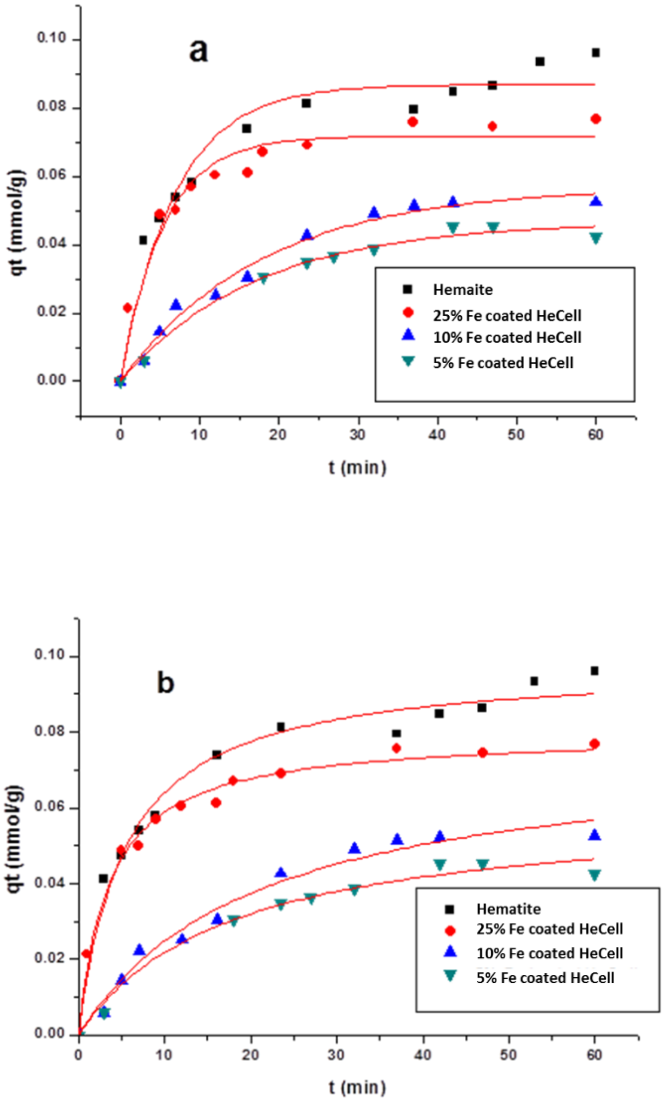

Figure 4.5 Kinetic uptake isotherms for the hematite and hematite-cellulose composite materials, as described by two kinetic models: (a) PFO, and (b) PSO models.

In Table 4.6, the SSE values were minimized according to each type of kinetic model (PFO and PSO). The PFO model assumed singular binding sites [148]; whereas, the PSO model assumed multiple adsorption sites where available. The hematite-cellulose materials can bind with roxarsone at multiple binding sites. Any chemisorption processes involving covalence forces through the sharing or exchange of electrons between the adsorbent and adsorbate were best described by the pseudo-second-order reaction [147]. On the other hand, an initial period of the adsorption process fit the pseudo-first-order reaction well [147]. At longer time intervals, the PSO kinetic model provided a better fit of the adsorption profile as shown herein. The similar rates of adsorption for hematite and its composites indicated that the binding sites occur between hematite and roxarsone. This concurred with the Lewis acid character of hematite and provided evidence that hematite is supported onto cellulose.

Table 4.6 Adsorption kinetic parameters from the PFO and PSO models for the uptake of roxarsone onto hematite and HeCell adsorbents at 295 K

Adsorbent	C_0 (mM)	PFO Model			PSO Model		
		k_1 (min^{-1})	$Q_{e,cal}$ (mmol/g)	SSE	k_2 (g/mmol min)	$Q_{e,cal}$ (mmol/g)	SSE
Hematite	1.50	0.145	0.0868	3.54E-4	1.91	0.0981	1.53E-4
25% Fe loaded HeCell	1.50	0.186	0.0717	2.39E-4	3.55	0.0796	5.80E-5
10% Fe loaded HeCell	1.50	0.0556	0.0569	5.46E-5	0.626	0.0765	7.66E-5
5% Fe loaded HeCell	1.50	0.0582	0.0467	2.12E-5	0.951	0.0600	3.56E-5

4.3 Thermodynamic Study

4.3.1 Adsorption parameters of the 30% Fe coated GC composite

The ΔG^o value can be obtained from the Langmuir adsorption constant (K_L), where $\Delta G^o = -RT \ln K_L$ and R is the ideal gas constant, T is temperature and K_L was the Langmuir adsorption constant [150]. In Table 4.7, the ΔG^o values were favorable according to the negative signs from the sorbent materials investigated. Among the various materials, goethite NPs had the most negative ΔG^o value for the adsorption of roxarsone, which provided further support that iron oxide sites were the most active sites for the GC composites.

Table 4.7 Thermodynamic parameters at 295 K for the adsorption of the roxarsone onto the goethite and the 30% Fe coated GC adsorbent materials

Parameters	T (K)	Cellulose	Goethite	30% Fe coated GC
$\Delta G°$ (kJ/mol)	298	-23.9	-33.1	-30.8

4.3.2 Adsorption parameters of the 25% Fe coated HeCell composite

The ΔG^o value can be obtained from the Langmuir adsorption constant (K_L), where $\Delta G^o = -RT \ln K_L$ and R is the ideal gas constant, T was temperature and K_L was the Langmuir adsorption constant [150]. Herein, the ΔG^o values are listed in Table 4.8, where negative values were observed for the materials investigated. This indicated the adsorption was spontaneous process.

Table 4.8 Thermodynamic parameters at 295 K for the adsorption of the roxarsone onto the hematite and HeCell adsorbent materials

Parameters	T (K)	Cellulose	Hematite	25% Fe coated HeCell
ΔG° (kJ/mol)	298	-23.9	-31.5	-31.0

4.3.3 The uptake of ROX by the 10% Fe coated HeCell at various Temperature

The uptake of roxarsone increased as temperatures decreased, this trend demonstrated that the sorption of roxarsone by the 10% Fe coated HeCell composite was an exothermic process. In the Table 4.9, adsorption rate constant was the highest at the lowest temperature which also indicated that the low temperature facilitated the adsorption process.

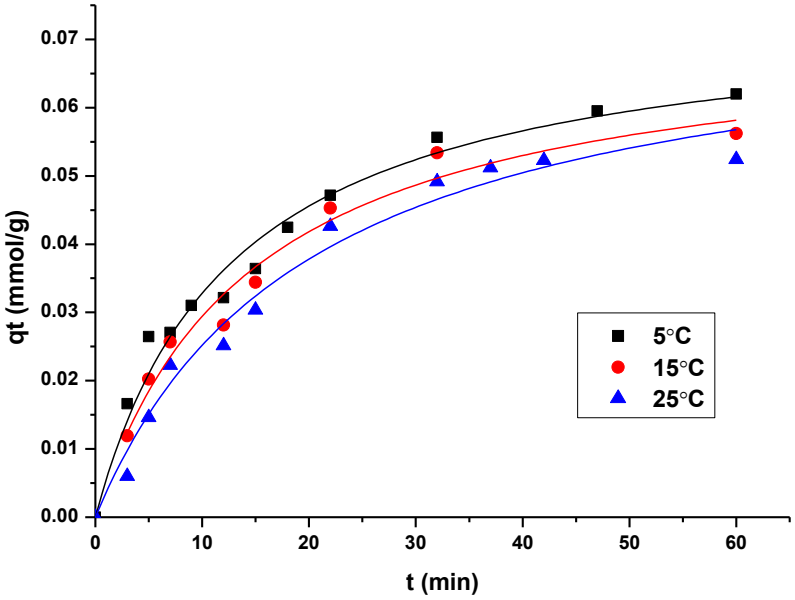

Figure 4.6 PSO fitted ROX uptake by the 10% Fe coated HeCell composite material

Table 4.9 Adsorption kinetics experiment parameters from the PSO model for the uptake of ROX onto adsorbents at different temperature

Adsorbent	T (K)	ROX C_0 (mM)	PSO Model		
			k_2 (g/mmol min)	$Q_{e,cal}$ (mmol/g)	SSE
10% Fe loaded HeCell	278	1.5	1.0	0.76	7.5E-6
10% Fe loaded HeCell	288	1.5	0.88	0.75	4.3E-5
10% Fe loaded HeCell	298	1.5	0.66	0.74	7.7E-5

The standard enthalpy of activation (ΔH^*), the entropy of activation (ΔS^*), and the Gibbs energy of activation (ΔG^*) in the adsorption process are calculated from a plot of ln k/T versus 1/T according to the Eyring equation (Eqn 4.1).

$$\ln\left(\frac{k}{T}\right) = \ln\frac{k_b}{h} + \frac{\Delta S^*}{R} - \frac{\Delta H^*}{RT} \qquad (4.1)$$

where k is the adsorption rate constant; k_b is the Boltzmann constant (1.381 X 10^{-23} J•K^{-1}); h is the Planck's constant (6.626 X 10^{-34} J•s); R is the ideal gas constant (8.314 J•mol^{-1}•K^{-1}); and T is the temperature (K). The values of ΔH^* and ΔS^* are determined from the slope and intercept of a plot of ln (k/T) versus 1/T. These values obtained were used to compute ΔG^* from Equation 4.2 below:

$$\Delta G^* = \Delta H^* - T\Delta S^* \qquad (4.2)$$

The activation energy (E_a) of the process was obtained by plotting ln k versus 1/T according to the Arrhenius equation (Eqn 4.3), the value of the slop (E_a/R) can be used to calculate E_a.

$$\ln K = \ln A + \frac{E_a}{R}\left(\frac{1}{T}\right) \qquad (4.3)$$

Where k is the rate constant; A is the pre-exponential factor; E_a is the activation energy; R is the gas constant (8.314 J•mol^{-1}•K^{-1}); and T is the temperature (K).

Table 4.10 Thermodynamic parameters for the uptake of ROX by the 10% Fe coated HeCell

T (K)	ΔE_a (kJ/mol)	Activation Parameters		
		ΔH^* (kJ/mol)	ΔS^* (J/Kmol)	ΔG^* (kJ/mol)
278	14.2	-16.6	-304	67.9
288				70.9
298				74.0

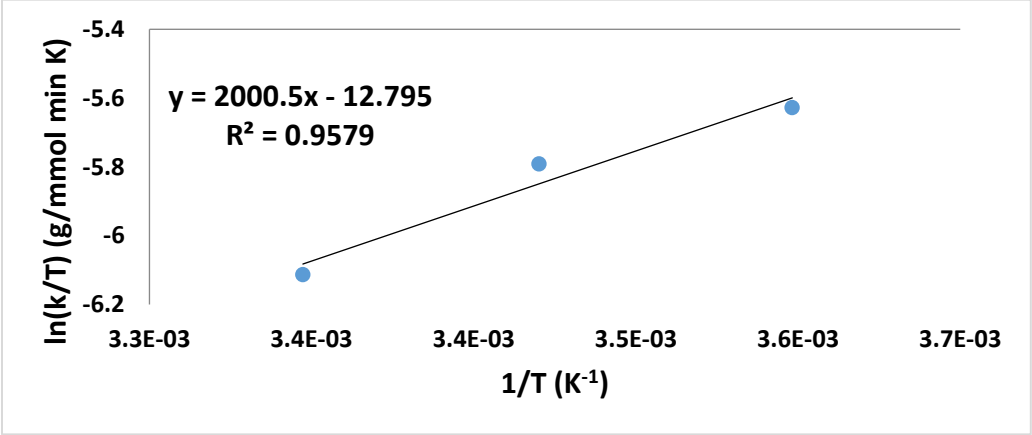

Figure 4.7 Eyring plots for ROX uptake at variable temperature at pH 7

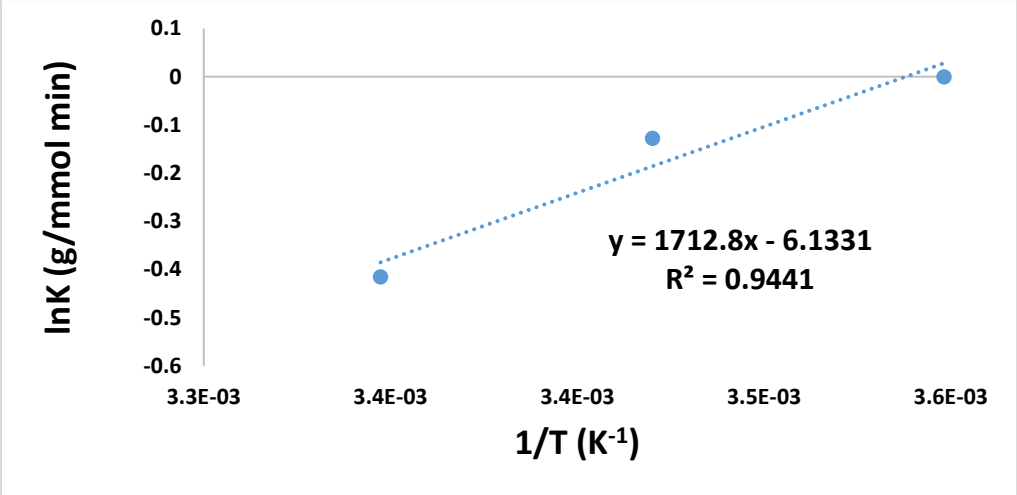

Figure 4.8 The activation energy (E_a) of the adsorption process of roxarsone onto the 10% Fe coated HeCell composites

4.4 Regeneration of the 10% Fe Coated HeCell adsorbent

4.4.1 10% Fe coated HeCell regeneration with the 0.6 M NaOH solution

Approximately 500 bed volumes of 0.6 M NaOH eluent was used to wash ca. 80% ROX from the 10% Fe loaded HeCell's surface, the high pH environment changed the hematite NPs' surface charge from positive to negative which separated the same negatively charged ROX species. Similar experimental procedures were adopted to wash roxarsone off from the 10% Fe coated HeCell by the 0.6 M NaCl solution, but the results showed there was no detectable roxarsone in the eluent solution. The saline solution was not a good regeneration fluid compared with the same concentration NaOH solution.

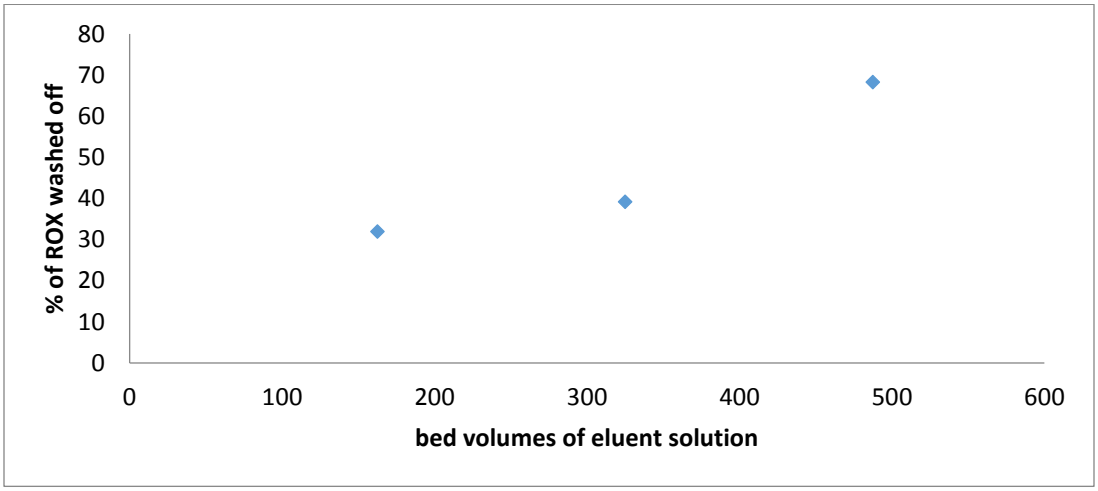

Figure 4.9 Regeneration graph of the 10% Fe loaded HeCell composite material

After washing with caustic solution, the adsorbent 10% Fe loaded HeCell was washed again with a large amount water to bring the pH to neutral. The neutralized adsorbent was again tested with 1.5 mM ROX solution to see the ROX removal efficiency; the results of removal efficiency are listed in the

Table 4.11.

Table 4.11 ROX adsorption efficiency of the 10% Fe loaded HeCell after each washing cycle

ROX adsorption efficiency of the 10% Fe loaded HeCell after each washing cycles	ROX removal efficiency (%)
1st cycle	11.66
2nd cycle	10.86
3rd cycle	10.43
4th cycle	9.80

4.5 Iron leaching test

The iron leaching tests were done on the 10% Fe coated GC and the 30% Fe coated GC composite, the results showed there were very small amounts of Fe leached into the liquid phase during the 5 days leaching tests. The peak value of the iron washed from the composite materials happened within the first 24 h, and then the amount of the iron leached into the liquid phase reduced greatly to about 10 μg/L after 48 h.

Table 4.12 The iron leaching tests

	10% Fe loaded GC	10% Fe loaded HeCell	30% Fe loaded GC
Total Volume (L)	0.1	0.1	0.1
Iron mass in the composites (mg)	10	10	30
Time (hours)	Amount of Fe leached out into the liquid phase (µg/L)	Amount of Fe leached out into the liquid phase (µg/L)	Amount of Fe leached out into the liquid phase (µg/L)
1	5	47	120
4	9.6	36	230
22	62	66	760
24	36	16	18
48	12	11	14
Total Fe leached (µg)	12.5	17.6	114.2
% of Iron leached out	0.12	0.18	0.38

The amount of iron leached out from the composite materials was less than 1% by weight, and provides support that most iron NPs were immobilized by the cellulose supports. Comparison of the 30% and 10% Fe coated GC composite materials, the 30% Fe coated material showed about 3 times more iron leached out than the 10% Fe loaded GC composite. More iron leaching from the 30% Fe loaded GC indicated there was more iron on the cellulose's surface, hence, more chances

for these iron NPs to be washed off. On the other hand, comparing the 10% Fe coated GC to the same 10% Fe coated HeCell composite, more iron NPs were washed off from the HeCell composite material. This could be due to the smaller size of the hematite NPs (10nm) which were more mobile than the goethite NPs (200nm) [119].

4.6 Adsorption mechanism

From the adsorption kinetics experiments, the rapid adsorption rate indicated that favorable interactions occur between the ROX anions and goethite NPs [18]. The ion exchange process between the hydroxide groups of goethite NPs may involve H-bonding or electrostatic interactions with roxarsone (*cf.* Table 4.9)

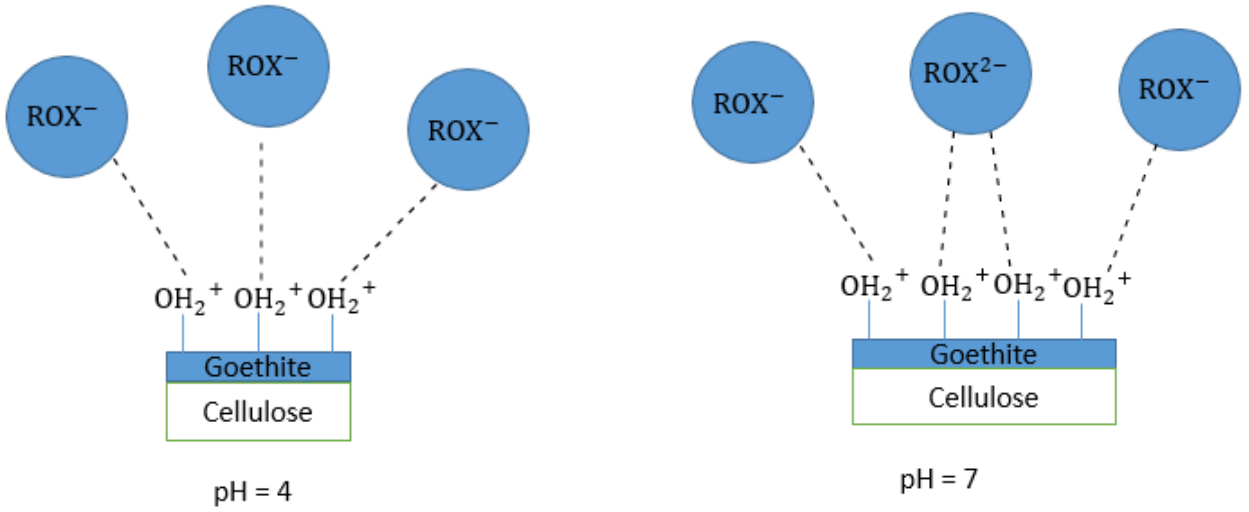

Figure 4.10 Electrostatic interactions between goethite NPs and roxarsone at pH 4 and pH 7.

The Raman spectral results in Figure 3.5 and 3.7 showed evidence of a decreasing of Fe-OH_2^+ signature after uptake of ROX. This trend indicated that the surface of hydrated goethite and composite contributed significantly to the binding of ROX. In Figure 3.5 b, the Fe-OH_2^+ spectral band was reduced dramatically after adsorption of ROX, especially for goethite materials which indicated that goethite NPs contributed mainly as the primary binding site.

CHAPTER 5 : CONCLUSION AND FUTURE WORK

5.1 Conclusion

Composite materials containing cellulose and goethite were prepared at variable goethite composition and characterized using various materials characterization methods. The IR/Raman spectroscopy, TGA, and TEM analysis results provided support that goethite was coated onto cellulose up to 30% goethite (w/w) content. The adsorption properties of the binary composites and their precursors (cellulose and goethite) were compared at equilibrium and dynamic conditions using a model organoarsenical (roxarsone). The adsorption capacity of the materials revealed that the binary composites display greater uptake of roxarsone over the cellulose. The monolayer adsorption (Q_m; mmol/g) capacity adopted the following trend, listed in parentheses: cellulose (0.028), 30% Fe loaded GC composite (0.066), and pure goethite (0.073), where goethite was the active adsorption site in the composite materials. The doubly charged anion of roxarsone appeared to be more strongly bound than the single charged species since the goethite-based sorbents adopted as positive zeta-potential at such conditions. However, the dianion roxarsone species may occupy more binding sites on the goethite surface which resulted in less dianion roxarsone species that can complex with goethite NPs. The pH dependent uptake for goethite and its composites displayed reduced adsorption at pH values above the pH_{pzc} value of goethite. The kinetic adsorption profiles were well-described by the PSO model, in agreement with the presence of multiple adsorption sites for such binary GC composites. The binary GC composites reported herein were anticipated to have a wide range of application toward the sorption of inorganic and organic anions due to their synthetic versatility and tunable properties [151]. The development of reusable cellulose, bio-flocculants with magnetic properties represented promising materials for the green processing water and wastewater supplies [150].

Composite materials containing cellulose and hematite were prepared and characterized. Hematite was supported onto cellulose, the adsorption properties of the composites and their precursors (cellulose and hematite) were compared at equilibrium and dynamic conditions with a model organoarsenical (roxarsone). The adsorption capacity of the various materials revealed that hematite and its composites with cellulose had the variable uptake capacity, where hematite served

as the primary adsorption site. The monolayer adsorption capacity adopted the following order: cellulose (0.028 mmol/g), 10% Fe coated GC (0.0222 mmol/g), 10% Fe coated HeCell (0.0873 mmol/g), goethite (0.0730 mmol/g) and hematite (0.155 mmol/g). The larger surface area of hematite NPs resulted in greater uptake of roxarsone than goethite NPs since better dispersion of the hematite NPs increased the uptake of roxarsone. The kinetic adsorption profiles were well described by the PSO model, in agreement with multiple adsorption sites in the case of HeCell composites. The roxarsone uptake by both 30% Fe coated GC and 25% Fe coated HeCell showed that adsorption capacity of the ~25% Fe NPs coated cellulose composite can achieve similar roxarsone uptake as their precursor goethite and hematite.

5.2 Future Work

Future research involving iron oxide composite materials can be conducted in several areas. Firstly, the methods of dispersion iron oxide NPs onto their support materials need to be investigated in greater detail. A more comprehensive study on the formation of iron oxide and cellulose composite needs to be carried out to optimize the synthesis process, as evidenced from results published by Kong and Wilson [152]. In this research more than 30% goethite NPs were used to coat the cellulose to yield GC composite materials with similar performance as the pure goethite NPs. There is a need to study how the aggregation of iron oxide NPs can be prevented or controlled which will lead to the development of improved iron oxide coated cellulose adsorbents.

Secondly, a support material with larger surface area than cellulose can be used to support iron oxide NPs. The larger surface of the supporting material would provide more active sites to bind the iron oxide NPs for the same unit mass of support. Tests of iron oxide coated clay samples with roxarsone have demonstrated improved uptake efficiency than the cellulose supported composites. The hypothesis was more surface area and active sites from the clay material could bind more iron oxide NPs than the cellulose support, hence more iron oxide NPs were available on the surface of clay to bind more roxarsone.

Thirdly, it is also possible to synthesize iron oxide NPs with greater surface area and active sites that can complex with the oxyanion species. Iron resources are relatively abundant on earth,

and it is a cost effective way to develop iron-based nanomaterial with greater surface area for large scale environmental remediation.

Fourthly, it is recommended to synthesize magnetite coated cellulose composites due to their paramagnetic properties. These composite materials can be collected in a strong magnetic field and reprocessed to isolate the composite materials.

Finally, the iron oxide-cellulose regeneration study can be optimized by investigating the residence time for contacting eluent solution with the adsorbent and the effects of concentration of NaOH on the regeneration efficiency. The alternative eluent solution such as the saturated brine solution for the regeneration of iron oxide-cellulose adsorbents can be investigated to provide a more environmentally friendly process for the sorbent regeneration process.

REFERENCES

1. Smith, A. H.; Hopenhayn-Rich, C.; Bates, M. N.; Goeden, H. M.; Hertz-Picciotto, I.; Duggan, H. M.; Wood, R.; Kosnett, M. J.; Smith, M. T., Cancer risks from arsenic in drinking water. *Environ. Health Perspect.* **1992,** *97*, 259-267.
2. Ahmed, M. F. An Overview of Arsenic Removal Technologies in Bangladesh and India. http://inweh.unu.edu/wp-content/uploads/2015/05/An-Overview-of-Arsenic-Removal-Technologies.pdf.
3. Barlow, M., *Blue Covenant: The Global Water Crisis and the Coming Battle for the Right to Water*. The New Press: 2009.
4. Bednar, A. J.; Garbarino, J. R.; Ferrer, I.; Rutherford, D. W.; Wershaw, R. L.; Ranville, J. F.; Wildeman, T. R., Photodegradation of roxarsone in poultry litter leachates. *Sci. Total Environ.* **2003,** *302*, 237-245.
5. Peng, H.; Hu, B.; Liu, Q.; Li, J.; Li, X. F.; Zhang, H.; Le, X. C., Methylated Phenylarsenical Metabolites Discovered in Chicken Liver. *Angew. Chem. Int. Ed.* **2017,** *56*, 6773-6777.
6. Brown, B. L.; Slaughter, A. D.; Schreiber, M. E., Controls on roxarsone transport in agricultural watersheds. *Appl. Geochem.* **2005,** *20*, 123-133.
7. Welch, A. H.; Lico, M. S.; Hughes, J. L., Arsenic in groundwater of the Western United States. *Ground Water* **1988,** *26*, 333-347.
8. Cullen, W. R.; Reimer, K. J., Arsenic Speciation in the Environment. *Chem. Rev.* **1989,** *89*, 713-764.
9. Ellis, B. D.; MacDonald, C. L. B., Stabilized Arsenic(I) Iodide: A Ready Source of Arsenic Iodide Fragments and a Useful Reagent for the Generation of Clusters. *Inorg. Chem.* **2004,** *43* (19), 5981-5986.
10. Ravenscroft, P.; Brammer, H.; Richards, K., *Arsenic Pollution: A Global Synthesis*. Wiley-Blackwell: 2009.
11. Metal Mining Effluent Regulations - Authorized Limits of Deleterious Substances. the Minister of Justice: 2017; p 34.
12. Shaw, S. A.; Hendry, M. J.; Essilfie-Dughan, J.; Kotzer, T.; Wallschlager, D., Distribution, characterization, and geochemical controls of elements of concern in uranium mine tailings, Key Lake, Saskatchewan, Canada. . *Appl. Geochem.* **2011,** *26*.
13. Levasseur, J.; Marcoux, J. Bad water: 'Third World' conditions on First Nations in Canada. http://www.cbc.ca/news/canada/manitoba/bad-water-third-world-conditions-on-first-nations-in-canada-1.3269500 (accessed Nov 14 2016).
14. Li, S.; Chen, W.; Pei, X.; Zhang, S.; Feng, X.; Zhou, J.; Wang, B., Water Purification: Adsorption over Metal-Organic Frameworks. *Chin. J. Chem.* **2016,** *34*, 175-185.
15. Nikolaidis, N. P.; Dobbs, G. M.; Lackovic, J. A., Arsenic removal by zero-valent iron: field laboratory and modeling studies. *Water Res.* **2003,** *37*, 1417-1425.
16. Lunge, S.; Singh, S.; Sinha, A., Magnetic iron oxide (Fe3O4) nanoparticles from tea waste for arsenic removal. *J. Magn. Magn. Mater.* **2014,** *356*.
17. Yu, X.; Tong, S.; Ge, M.; Zuo, J.; Cao, C.; Song, W., One-step synthesis of magnetic composites of cellulose-iron oxide nanoparticles for arsenic removal. *J. Mater. Chem. A* **2013,** *1*, 959-965.
18. Hokkanen, S.; Repo, E.; Lou, S.; Sillanpää, M., Removal of arsenic(V) by magnetic nanoparticle activated microfibrillated cellulose. *Chem. Eng. J.* **2015,** *260*, 886-894.

19. Hu, J.; Tong, Z.; Chen, G.; Zhan, X.; Hu, Z., Adsorption of roxarsone by iron (hydr)oxide-modified multiwalled carbon nanotubes from aqueous solution and its mechanisms. *Int. J. Environ. Sci. Technol.* **2014,** *11* (785).
20. Hu, J.; Tong, Z.; Hu, Z.; Chen, G.; Chen, T., Adsorption of Roxarsone From Aqueous Solution by Multi-walled Carbon Nanotubes. *J. Colloid Interf. Sci.* **2012,** *377* (1), 355-361.
21. Kwon, J. H.; Wilson, L. D.; Sammynaiken, R., Sorptive Uptake Studies of an Aryl-Arsenical with Iron Oxide Composites on an Activated Carbon Support. *Materials* **2014,** *7*, 1880-1898.
22. Chen, W. R.; Huang, C. H., Surface adsorption of organoarsenic roxarsone and arsanilic acid on iron and aluminum oxides. *J. Hazard. Mater.* **2012,** *227*, 378-385.
23. Bouatay, F.; Meksi, N.; Slah, F., Chemical Modification of Cellulosic Fibers Using Eco-Friendly Compounds to Improve Dyeing with Cationic Dyes. *J. Textile Sci. Eng* **2014,** *4* (2), 1-8.
24. Appel, C.; Ma, L.; Rhue, R.; Kennelley, E., Point of zero charge determination in soils and minerals via traditional methods and detection of electroacoustic mobility. *Geoderma* **2003,** *113*, 77-93.
25. Silver, J., Chemistry of Iron, 1st ed.; Blackie Academic & Professional: Glasgow,. 1993; p 5.
26. Cornell, R. M.; Schwertmann, U., *The Iron Oxides: Structure, Properties, Reactions, Occurences and Uses*. WILEY-VCH Verlag GmbH & Co. KGaA, : Weinheim, 2003; p 659.
27. Towe, K. M.; Bradley, W. F., Mineralogical constitution of colloidal "hydrous ferric oxides" *J. Collid Interface Sci.* **1967,** *24*, 384-392.
28. Chukhrov, F. V.; Zvyagin, B. B.; Ermilova, L. P.; Gorshkov, A. I., New data on iron oxides in the weathering zone. *Proc. Int. Clay Conf. Madrid* **1973**, 333-341.
29. Schwandt, H.; Kogel-Knabner, I.; Stanjek, H.; Totsche, K., Sorption of an acidic herbicide on synthetic iron oxides and soils: sorption isotherms. *Sci. Total Environ.* **1992,** *123/124*, 121-131.
30. Bragg, W. H.; Bragg, W. L., *X-rays and crsytal structure 3rd ed.* Bell and Sons: London, 1918.
31. Bethe, H., splitting of terms in crystals. *Ann. Phys.* **1929,** *3*, 133-206.
32. Tsuchida, R., Absorption Spectra of Co-ordination Compounds. I. *Bull. Chem. Soc. Jpn.* **1938,** *13* (5), 388-400.
33. Fan, M.; Dai, D.; Huang, B., Fourier Transform Infrared Spectroscopy for Natural Fibres. In *Fourier Transform - Materials Analysis, Salih Salih (Ed.)*, InTech: Rijeka, Croatia: 2012.
34. Soliman, S. A.; El-Zawahry, Y. A.; El-Mougith, A. A., Fungal Biodegradation of Agro-Industrial Waste. *Cellulose - Biomass Conversion* **2013**.
35. Yadav, M.; Mun, S.; Hyun, J.; Kim, J., Synthesis and characterization of iron oxide/cellulose nanocomposite film. *Int. J. Biol. Macromolec* **2015,** *74*, 142-149.
36. Kurokawa, Y., Ro separation of rare earth ions from aqueous solution by hydrous fe oxide cellulose — composite membrane. *Desalination* **1982,** *41* (1), 115-119.
37. Wojnárovits, L.; Földváry, C. M.; Takács, E., Radiation-induced grafting of cellulose for adsorption of hazardous water pollutants: A review. *Radiat. Phys. Chem.* **2010,** *79*, 848-862.
38. Liu, S.; Zhou, J.; Zhang, L.; Guan, J. G.; Wang, J., Synthesis and Alignment of Iron Oxide Nanoparticles in a Regenerated Cellulose Film. *Macromol. Rapid Commun.* **2006,** *27* (24), 2084-2089.
39. Reid, M. L.; Brown, M. B.; Moss, G. P.; Jones, S. A., An investigation into solvent-membrane interactions when assessing drug release from organic vehicles using regenerated cellulose membranes. *J. Pharm. Pharmacol.* **2008,** *60*, 1139-1147.

40. Gardner, D. J.; Oporto, G. S.; Mills, R.; Samird, M. A. S. A., Adhesion and surface issues in cellulose and nanocellulose. *J. Adhes. Sci. Technol.* **2008,** *22*, 545-567.
41. O'Connell, D. W.; Birkinshaw, C.; O'Dwyer, T. F., Heavy metal adsorbents prepared from the modification of cellulose: A review. *Bioresour. Technol.* **2008,** *99*, 6709-6724.
42. Zhang, L.-M., Cellulosic associative thickeners. *Carbohydr. Polym.* **2001,** *45*, 1-10.
43. Kalia, S.; Kaith, B. S.; Kaur, I., Pretreatments of natural fibers and their application as reinforcing material in polymer composites—A review. *Polym. Eng. Sci.* **2009,** *49*, 1253-1272.
44. Habibi, Y.; Lucia, L. A.; Rojas, O. J., Cellulose nanocrystals: chemistry, selfassembly, and applications. *Chem. Rev.* **2010,** *110* (6), 3479-3500.
45. Olsson, R. T.; Samir, M. A.; Salazar-Alvarez, G.; Belova, L.; Ström, V.; Berglund, L. A.; Ikkala, O.; Nogues, J.; Gedde, U. W., Making flexible magnetic aerogels and stiff magnetic nanopaper using cellulose nanofibrils as templates. *Nature nanotechnology* **2010,** *5* (8), 584-588.
46. Lee, H.; Lee, E.; Kim, D.; Jang, N.; Jeong, Y.; Jon, S., Antibiofouling polymer-coated superparamagnetic iron oxide nanoparticles as potential magnetic resonance contrast agents for in vivo cancer imaging. *J Am Chem Soc.* **2006,** *128* (22), 7383-7389.
47. Duro, L., Arsenic sorption onto natural hematite, magnetite, and goethite. . *Journal of Hazardous Materials* **2007,** *141*, 575-580.
48. Myers, D., Surfactant Science and Technology. Wiley-Inter science: Hoboken, 2006; pp 150-152, 329-348.
49. Adamson, A.; Gast, A., In *Physical Chemistry of Surfaces.*, Wiley-Interscience: New York, 1997; pp 390-420.
50. Sing, K. S. W.; Everett, D. H.; Haul, R. A. W.; Moscou, L.; Pierotti, R. A.; Rouquérol, J.; Siemeniewska, T., Reporting physisorption data for gas/solid systems with special reference to the determination of surface area and porosity. *Pure & Appl. Chem.* **1985,** *57*, 603-619.
51. Langmuir, I., The adsorption of gases on plane surfaces of glass, mica and platinum. *J. Am. Chem. Soc.* **1918,** *40* (9), 1361-1403.
52. Freundlich, H., Kolloidfällung und Adsorption. *Angew. Chem.* **1907,** *20*, 749-750.
53. Brunauer, S.; Emmett, P. H.; Teller, E., Adsorption of Gases in Multimolecular Layers. *J. Am. Chem. Soc.* **1938,** *60* (2), 309-319.
54. Lagergren, S., About the theory of so-called adsorption of soluble substances. *K Sven Vetenskapsakad Handl* **1891,** *24*, 1-39.
55. Dzombak, D. A.; Morel, F. M. M., Surface complexation modeling. Hydrous ferric oxide. *J. Wiley, New York* **1990**, 393.
56. Fendorf, S. E.; Eick, M. J.; Grossl, P.; Sparks, D. L., Arsenate and chromate retention mechanisms on geoethite. 1. Surface structure. *Environ. Sci. Techn.* **1997,** *31*, 315-320.
57. Hingston, F. J.; Posner, A. M.; Quirk, J. P., anion adsorption by goethite and gibbsite. II. Desorption of anions from hydrous oxide surfaces. *J. Soil Sci.* **1974,** *25*, 16-26.
58. Lumsdon, D. G.; Fraser, A. R.; Russell, J. D.; Livesey, N. T., New infrared band assignments for the arsenate ion adsorbed on synthetic goethite (α-Fe-OOH). *J. Soil Sci.* **1984,** *35*, 381-386.
59. Bibak, A.; Borggaard, O. K., Molybdenum adsorption by aluminum and iron oxides and humic acid. *Soil sci.* **1994,** *158*, 323-328.
60. Gold, S.; Forster, H. S.; Heick, E. I., Temperature effects on boron adsorption by reference minerals and soils. *Soil Sci.* **1993,** *156*, 316-321.
61. Su, C.; Suarez, D. L., In situ infrared speciation of adsorbed carbonate on aluminum and iron oxides. *Clays Clay Min.* **1997,** *45*, 814-825.

62. Hiemstra, T.; Van Riemsdijk, W. H., Fluoride adsorption on goethite in relation to different types of surface sites. *J. Colloid Interface Sci.* **2000,** *225*, 94-104.
63. Hingston, F. J.; Atkinson, R. J.; Posner, A. M.; Quirk, J. P., Specific adsorption of anions on goethite. In *Int. Congr. Soil Sci. Trans. 9th (Adelaide, Aust.) I*, 1968; pp 669-678.
64. Machesky, M.; Andrade, W.; Rose, A., Adsorption of gold (III)-chloride and gold (I) thiosulphate anions by goethite. *Geochim. Cosmochim. Acta* **1991,** *55*, 769-776.
65. Ainsworth, C. C.; Sumner, M. E., Effect of aluminum substitution in goethite on phosphorus adsorption: II. Rate of adsorption. *Soil Sci. Soc. Am. J.* **1985,** *49*, 1149-1153.
66. Ainsworth, C. C.; Sumner, M. E.; Hurst, V. J., Effect of aluminum substitution in goethite on phosphorus adsorption: I. Adsorption and isotopic exchange. *Soil Sci. Soc. Am. J.* **1985,** *49*, 1142-1149.
67. Anderson, M. A.; Tejedor-Tejedor, M. I.; Stanforth, R. R., Influence of aggregation on the uptake kinetics of phosphate by goethite. *Environ. Sci. Techn.* **1985,** *19*, 632-637.
68. Hingston, F. J.; Posner, A. M.; Quirk, J. P., Adsorption of selenite by goethite. *Adv. Chem. Series* **1968,** *79*, 82-90.
69. Bowden, J. W.; Nagarajah, S.; Barrow, N. J.; Posner, A. M.; Quirk, J. P., Describing the adsorption of phosphate, citrate and selenite on a variable-charge ineral surface. *Aust. J. Soil Res.* **1980,** *18*, 49-60.
70. Hingston, F. J.; Posner, A. M.; Quirk, J. P., Competitive adsorption of negatively charged ligands on oxide surfaces. *Disc. Faraday Soc.* **1971,** *52*, 334-342.
71. Brown, A. S. C.; Hargreaves, J. S. J.; Ryniersscе, B., A study of the structural and catalytic effect of sulphation on iron oxide catalysts prepared from goethite and ferrihydrite precursors for methane oxidation. *Catalysis Letters* **1998,** *53*, 7-13.
72. Hansmann, D. D.; Aderson, M. A., Using electrophoresis in modeling sulfate, selenite, and phosphate adsorption onto goethite. *Environ. Sci. Technol.* **1985,** *19*, 544-551.
73. Avena, M. J.; Koopal, L. K., Kinetics of humic acid adsorption on solid-water interfaces. *Environ. Sci. Techn.* **1999,** *33*, 2739-2744.
74. Cornell, R. M.; Schindler, P. W., Infrared study of the adsorption of hydroxyl carboxylic acids on α-FeOOH and amorphous Fe(III)-hydroxide. *Colloid Polymer Sci.* **1980,** *258*, 1171-1175.
75. Filius, J. D.; Hiemstra, T.; Van Riemsdijk, W. H., Adsorption of small weak organic acids on goethite: modeling and mechanisms. *J. Colloid Interface Sci.* **1997,** *195*, 368-380.
76. Nowack, B.; Sigg, L., Adsorption of EDTA and Metal EDTA complexes onto goethite. *J. Colloid Interface Sci.* **1996,** *177*, 106-121.
77. Parfitt, R. L.; Fraser, A. R.; Farmer, V. C., Adsorption on hydrous oxides. III. Fulvic acid and humic acid on goethite, gibbsite and imogolite. *J. Soil Sci.* **1977,** *28*, 289-296.
78. Tipping, E.; Cooke, D., The effects of adsorbed humic substances on the surface charge of goethite (α-FeOOH) in freshwaters. *Geochim. Cosmochim. Acta* **1982,** *46*, 75-80.
79. McBride, M. B.; Kung, K. H., adsorption of phenol and substituted phenols by iron oxides. *Environ. Toxic. Chem.* **1991,** *10*, 441-448.
80. Sticher, H.; Agusoni-Phan, N., Adsorption von 2,4-D an Eisenoxidhydroxiden. Miteilgn. *Dtsch. Bodenkdl. Ges.* **1977,** *25*, 183-188.
81. Watson, J. R.; Posner, A. M.; Quirk, J. P., Adsorption of the herbicide 2,4-D on goethite. *J. Soil Sci.* **1973,** *24*, 503-511.
82. Fuller, C. C.; Davis, J. A.; Waychunas, G. A., Surface chemistry of ferrihydrite: Part 2. Kinetics of arsenate adsorption and coprecipitation. *Geochim. Cosmochim. Acta.* **1993,** *57*, 2271-2282.

83. Hsia, T. H.; Lo, S. L.; Lim, C. F.; Lee, D. Y., Characterization of arsenate adsorption on hydrous iron oxide using chemical and physical methods. *Colloids & Surfaces* **1994,** *85*, 1-7.
84. Watanabe, S.; Matsumoto, S., Effect of monosilicate, phosphate, and carbonate on irom dissolution by mugineic acid. *Soil Sci. Plant Nutr.* **1994,** *40*, 9-17.
85. Borggaard, O. K., The influence of iron oxides on phosphate adsorption by soil. *J. Soil Sci.* **1983,** *34*, 333-341.
86. J., G., Phosphate adsorption by humic/Fe-oxide mixtures aged at pH 4 and 7 and by poorly ordered Fe-oxide. *Geoderma* **1993,** *59*, 279-288.
87. Gupta, S. K. Uber die phosphate-Elimination in den Systemen H_3PO_4 γ-FeOOH und H_3PO_4-$FeCl_3$ und die Eigenschaften von Klarschlamm-Phosphate. Univ. Bern, 1976.
88. Anderson, P. R.; Benjamin, M. M., Effects of silicon on the crystallization and adsorption properties of ferric oxides. *Environ. Sci. Tech.* **1985,** *19*, 1048-1053.
89. Beckwith, R. S.; Reeve, R., Studies on soluble silica in soils. I. The sorption of silicic acid by soils and minerals. *Aust. J. Soil Res.* **1963,** *1*, 157-168.
90. Parfitt, R. L.; Smart, R. S. C., The mechanism of sulfate adsorption on iron oxides. *Soil Sci. Soc. Am. J.* **1978,** *42*, 48-50.
91. Hsia, T. H.; Lo, S. L.; Lin, C. F.; Lee, D. Y., Chemical and spectroscopic evidence for specific adsorption of chromate on hydrous iron oxide. *Chemosphere* **1993,** *26*, 1897-1904.
92. Jeon, B. H.; Dempsey, B. A.; Burgos, W. D.; Royer, R. A.; Roden, E. E., Modeling the Sorption Kinetics of Divalent Metal Ions and Hematite. *Water Res.* **2004,** *38* (10), 2499-2508.
93. Adegoke, H. I.; Adekola, F. A.; Fatoki, O. S.; Ximba, B. J., Sorptive Interaction of Oxyanions with Iron Oxides: A Review. *Pol. J. Environ. Stud.* **2012,** *22* (1), 7-24.
94. Ai, L.; Zhang, C.; Liao, F.; Wang, Y.; Li, M.; Meng, L.; Jiang, J., Removal of methylene blue from aqueous solution with magnetite loaded multi-wall carbon nanotube: Kinetic, isotherm and mechanism analysis. *J. Hazard. Mater* **2011,** *198*, 282-290.
95. C., X.; Wang, Y.; Zhao, P. H.; Chen, H. Y.; Liu, Y. P., Porous hematite microflowers toward the adsorption of organic pollutants from water. *Materials Let.* **2015,** *159*, 64-67.
96. Lovgren, L.; Sjoberg, S.; Schindler, P. W., Acid/base reaction and aluminum (III). Complexation at the surface of goethite. *Geochim. Cosmochim. Acta.* **1990,** *54*, 1301-1306.
97. Bochatay, L.; Perseen, P.; Lovgren, L.; Brown Sr., G. E., XAFS study of Cu at water-goethite (α-FeOOH) interface. *J. Phys. IV France* **1997,** *2*.
98. Coughlin, B. R.; Stone, A. T., Non reversible adsorption of divalent metal ions (MnII, CoII, NiII, CuII and PbII) onto goethite. Effects of acidification, FeII addition and picolinic acid addition. *Environ. Sci. Techn.* **1995,** *29*, 2445-2455.
99. Forbes, E. A.; Posner, A. M.; Quirk, J. P., The specific adsorption of divalent Cd, Co, Cu, Pb, and Zn on goethite. *J. Soil Sci.* **1976,** *27*, 154-166.
100. Barrow, J. J.; Cox, V. C., The effects of pH and chloride concentration on mercury sorption. I. Goethite. *J. Soil Sci.* **1992,** *43*, 437-450.
101. Collins, C. R.; Sherman, D. M.; Ragnarsdottir, K. V., Surface complexation of Hg on goethite: mechanism from EXAFS spectroscopy and density functional calculations. *J. Colloid interface Sci.* **1999,** *219*, 345-350.
102. Bleam, W. F.; McBride, M. B., Cluster formation vs. isolated site formation. A study of Mn(II) and Mg(II) adsorption on boehmite and goethite. *J. Colloid interface Sci.* **1985,** *103*, 124-132.
103. His, C. D.; Langmuir, D., Adsorption of uranyl onto ferric oxyhydroxides: Application of the surface complexation site-binding model. *Geochim. Cosmochim. Acta.* **1985,** *48*, 1931-1941.

104. Kinniburgh, D. G.; Jackson, M. L.; Syers, J. K., Adsorption of alkaline earth, transition, and heavy metal cations by hydrous oxide gels of iron and aluminum. *Soil Sci. Soc. Am. J.* **1976,** *40*, 796-799.
105. Ainsworth, C. C.; Pilon, J. L.; Gassman, P. L.; van der Sluys, W. G., Coblat, cadmium, and lead sorption to hydrous ferric oxide: Residence time effect. *Soil Sci. Soc. Am. J.* **1994,** *58*, 1615-1623.
106. Waite, T. D.; Davis, S. A.; Payne, T. E.; Waychunas, G. A.; Xu, N., Uranium (VI) adsorption on ferrihydrite, Application of a surface complexation model. *Geochim. Cosmochim, Acta* **1994,** *58*, 5465-5478.
107. Benjamin, M. M.; Leckie, J. O., Multiple-site adsorption of Cd, Cu, Zn, and Pb on amorphous iron oxyhydroxide. *J. Colloid Interface Sci.* **1981,** *79*, 209-221.
108. Crawford, R. J.; Harding, I. H.; Mainwaring, D. E., Adsorption and coprecipitation of single heavy metal ions onto the hydrated oxides of iron and chromium. *Langmuir* **1993,** *9*, 3050-3056.
109. White, B. R.; Stackhouse, B. T.; A., H. J., Magnetic γ-Fe_2O_3 nanoparticles coated with poly-l-cysteine for chelation of As(III), Cu(II), Cd(II), Ni(II), Pb(II) and Zn(II). *J. Hazard. Mater* **2009,** *161*, 848-853.
110. Ma, T. Y.; Zhang, X. J.; Yuan, Z. Y., Hierarchically Meso-/Macroporous Titanium Tetraphosphonate Materi-als: Synthesis, Photocatalytic Activity and Heavy Metal Ion Adsorption. *MICROPOR MESOPOR MAT* **2009,** *123*, 234-242.
111. Mamindy-Pajany, Y.; Hurel, C.; Marmier, N.; Romeo, M., Arsenic Adsorption onto Hematite and Goethite. *Comptes Rendus Chimie* **2009,** *12* (8), 876-881.
112. Wu, Z. X.; Li, W.; Webley, P. A.; Zhao, D. Y., Synthesis of magnetic hollow carbon nanospheres with superior microporosity for efficient adsorption of hexavalent chromium ions. *Adv. Mater.* **2012,** *24*, 465-491.
113. Yu, L.; Wu, H.; Wu, B.; Wang, Z.; Cao, H.; Fu, C.; Jia, N., Magnetic Fe_3O_4-Reduced Graphene Oxide Nanocomposites-Based Electrochemical Biosensing. *Nano-Micro Letters* **2014,** *6* (3), 258-267.
114. Geng, Z. G.; Lin, Y.; Yu, X.; Shen, Q. H.; Ma, L.; Li, Z. Y.; Pan, N.; Wang, X. P., Highly efficient dye adsorption and removal: a functional hybrid of reduced graphene oxide-Fe3O4 nanoparticles as an easily regenerative adsorbent. *J. Mater. Chem.* **2012,** *22*, 3527-3535.
115. Gai, S. L.; Yang, P. P.; Ma, P. A.; Wang, D.; Li, C. X.; Li, X. B.; Niu, N.; Lin, J., *J. Mater. Chem.* **2011,** *21*, 16420.
116. Nata, I. F.; Sureshkumar, M.; Lee, C. K., One-pot preparation of amine-rich magnetite/bacterial cellulose nanocomposite and its application for arsenate removal. *RSC Adv.* **2011,** *1* (4), 625-631.
117. Kwon, J. H.; Wilson, L. D., Sorptive Uptake Studies of an Aryl-Arsenical with Iron Oxide Composites on an Activated Carbon Support. *J. Env. Sci. & Health Part A* **2010,** *45*, 1793-1803.
118. Nayak, R.; Rao, J. R., Synthesis of active goethite and maghemite from scrap iron sources. *J. Sci. Ind. Res.* **2005,** *64*, 35-40.
119. Schwertmann, U.; Cornell, R. M., *Iron Oxides in the Laboratory*. . Wiley: Chichester, NY., 2000.
120. Mohamed, M. H.; Wilson, L. D., Kinetic Uptake Studies of Powdered Materials in Solution. *Nanomaterials* **2015,** *5*, 1-11.
121. Kumar, K. V., Linear and non-linear regression analysis for the sorption kinetics of methylene blue onto activated carbon. *J. Hazard. Mater.* **2006,** *B137*, 1538-1544.

122. Kosmulski, M.; Durand-Vidal, S.; Maczka, E.; Rosenholm, J. B., Morphology of synthetic goethite particles. *J Colloid Interface Sci* **2004,** *271*, 261-269.
123. Poletto, M.; Dettenbon, J.; Pistor, V.; Zeni, M.; Zattera, A. J., Materials produced from plant biomass. Part I: evaluation of thermal stability and pyrolysis of wood. *Mat. Res.* **2010,** *13*, 375-379.
124. Poletto, M.; Pistor, V.; Zattera, A. J., Structural Characteristics andThermal Properties of Native Cellulose. In *Cellulose – Fundamental Aspects*, InTech: 2013; pp 45-68.
125. Jaiswal, A.; Banerjee, S.; Mani, R.; Chattopadhyaya, M. C., Synthesis, characterization and application of goethite mineral as an adsorbent. *J. Environ. Chem. Eng.* **2013,** *1*, 281-289.
126. Cambier, P., Infrared study of goethites of varying crystallinity and particle size: I. interpretation of OH and lattice vibration frequencies. *Clay Minerals.* **1986,** *21*, 191-200.
127. Rout, K.; Mohapatra, M.; Anand, S., 2-Line ferrihydrite: synthesis, characterization and its adsorption behavior for removal of Pb (II), Cd (II), Cu (II) and Zn (II) from aqueous solutions. *Dalton Trans.* **2011,** *41*, 3302-3312.
128. Szymanska-Chargot, M.; Cybulska, J.; Zdunek, A., Sensing the Structural Differences in Celluloses from Apple and Bacterial Cell Wall Materials by Raman and FT-IR. *Sensors* **2011,** (11), 5543-5560.
129. Legodi, M. A.; Wall, d. d., The preparation of magnetite, goethite, hematite and maghemite of pigment quality from mill scale iron waste. *Dyes and Pigments* **2007,** (74), 161-168.
130. Cowen, S.; Duggal, M.; Hoang, T.; Al-Abadleh, H. A., Vibrational spectroscopic characterization of some environmentally important organoarsenicals - A guide for understanding the nature of their surface complexes. *Can. J. Chem.* **2008,** *86*, 942.
131. Fleger, Y.; Mastai, Y.; Rosenbluh, M.; Dressler, D. H., SERS as a probe for adsorbate orientation on silver nanoclusters. *J. Raman Spectrosc.* **2009,** *40*, 1572.
132. Raj, A.; Raju, K.; Varghese, H. T.; Granadeiro, C. M.; Nogueira, H. I. S.; Yohannan Panicker, C., IR, Raman and SERS Spectra of 2- (Methoxycarbonylmethylsulfanyl)-3,5-dinitrobenzene Carboxylic Acid. *J. Brazil. Chem. Soc.* **2009,** *20*, 549.
133. Haresh, R.; Philip, D.; Aruldhas, G., Infrared, Raman and SERS spectra of betaine arsenate. *Spectrosc. Lett.* **1995,** *28*, 11.
134. Olavarria-Fullerton, J.; De. Jesus, M. A., Surface-Enhanced Raman scattering (SERS) Characterization of Trace Organoarsenic Antimicrobials Using Silver/Polydimethylsiloxane Nanocomposites. *Appl. Spectro.* **2011,** *65*, 423.
135. Hanesch, M., Raman spectroscopy of iron oxides and (oxy)hydroxides at low laser power and possible application in environmental magnetic studies. *Geophys. J. Int.* **2009,** *177* (3), 941-948.
136. Gierlinger, N.; Keplinger, T.; Harrington, M., Imaging of plant cell walls by confocal Raman microscopy. *Nat Protoc.* **2012,** *7* (7), 1694-1708.
137. Avila, G.; Fernandez, J.; Mate, B.; Tejeda, G.; Montero, S., Ro-vibrational Raman Cross sections of Water Vapor in the OH Stretching Region. *J. Mol. Spectrosc.* **1999,** *196* (1), 77-92.
138. Das, S.; Hendry, M. J.; Essilfie-Dughan, J., Adsorption of selenate onto ferrihydrite, goethite, and lepidocrocite under neutral pH conditions. *Appl. Geochem.* **2013,** *28*, 185-193.
139. Mandal, S.; Mayadevi, S.; Kulkarni, B. D., Adsorption of Aqueous Selenite [Se(IV)] Species on Synthetic Layered Double Hydroxide Materials *Ind. Eng. Chem. Res.* **2009,** *48* (17), 7893-7898.
140. Moon, R. J.; Martini, A.; Nairn, J.; Simonsen, J.; Youngblood, J., Cellulose nanomaterials review: structure, properties and nanocomposites. *Chem. Soc. Rev.* **2011,** *40*, 3941-3994.

141. Roberts, A. P.; Liu, Q.; Rowan, C. J.; Chang, L.; Carvallo, C.; Torrent, J.; Horng, C., Characterization of hematite, goethite, greigite, and pyrrhotite using first-order reversal curve diagrams. *J. Geophys. Res.* **2006,** *111*, B12S35.
142. Oulego, P.; Villa-Garcia, M. A.; Laca, A.; Diaz, M., The effect of the synthetic route on the structural, textural, morphological and catalytic properties of iron(III) oxides and oxyhydroxides. *Dalton Transactions* **2016,** *45*, 9446-9459.
143. Hung, F. R.; Bhattacharya, S.; Coasne, B.; Thommes, M., Argon and krypton adsorption on templated mesoporous silicas: molecular simulation and experiment. *Adsorption* **2007,** *13* (5), 425-437.
144. Mou, F.; Guan, J. G.; Xiao, Z.; Sun, Z.; Shi, W.; Fan, X., Solvent-mediated synthesis of magnetic Fe2O3 chestnut-like amorphous-core/γ-phase-shell hierarchical nanostructures with strong As(V) removal capability. *J. Mater. Chem.* **2011,** *21*, 5414-5421.
145. Barrett, E. P.; Joyner, L. G.; Halenda, P. P., The Determination of Pore Volume and Area Distributions in Porous Substances. I. Computations from Nitrogen Isotherms. *J. Am. Chem. Soc.* **1951,** *73* (1), 373-380.
146. Okushita, K.; Komatsu, T.; Chikayama, E.; Kikuchi, J., Statistical approach for solid-state nmr spectra of cellulose derived from a series of variable parameters. *Polym. J.* **2012,** *44*, 895-900.
147. Ho, Y. S., Pseudo-second order model for sorption processes. *Proc. Biochem.* **1999,** *34*, 451-465.
148. Piergiovanni, P. R., Adsorption kinetics and isotherms: A Safe, Simple, and Inexpensive Experiment for Three Levels of Students. *J. Chem. Educ.* **2014,** *91* (4), 560-565.
149. Crini, G., Recent developments in polysaccharide-based materials used as adsorbents in wastewater treatment. *Prog. Polym. Sci.* **2005,** *30* (1), 38-70.
150. Hena, S.; Fatihah, N.; Tabassum, S.; Jing, S. Y., Magnetophoretic harvesting of freshwater microalgae using polypyrrole/Fe_3O_4 nanocomposite and its reusability. *J. App. Phycol.* **2016,** *28*, 1597.
151. Mahaninia, M. H.; Wilson, L. D., Phosphate uptake studies of cross-linked chitosan bead materials. *J. Colloid Interf. Sci.* **2017,** *485*, 1-12.
152. Kong, D.; Wilson, L. D., Synthesis and characterization of cellulose-goethite composites and their adsorption properties with roxarsone. *Carbohydr Polym* **2017,** *169*, 282-294.